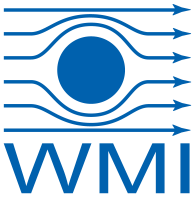

TECHNISCHE UNIVERSITÄT MÜNCHEN

WALTHER-MEISSNER-INSTITUT FÜR TIEF-TEMPERATURFORSCHUNG

BAYERISCHE AKADEMIE DER WISSENSCHAFTEN

Spin-Orbit Torques and Magnetization Dynamics in Non-collinear Magnets

Master's Thesis

Lukas Liensberger

Supervisor: Prof. Dr. Rudolf Gross
Advisor: Dr. Mathias Weiler

Garching, October 2017

Fakultät für Physik
Technische Universität München

Contents

Chapter 1

Introduction

In the past decades, our ever increasing demand for computational power, lead to the development of novel electronic devices. Widespread use of information processing devices, started with the discovery of the transistor. Further research lead to the development of integrated circuits, as they are still used in today's microprocessors. The miniaturization of the feature size, e.g., the gate size of the transistors used in these devices, continuously improves their performance. However, the feature size now apporaches fundamental physical limits like the Heisenberg uncertainty [1], which will render its further downsizing impossible in the near future.

New technologies are required in order to overcome these problems. One solution is to exploit the spin of the electron and not only its electrical charge. In 1988, Albert Fert [2] and Peter Grünberg [3] independently discovered the giant magnetoresistance (GMR) in multilayers of iron and chrome. The discovery was honoured with the Nobel Prize in Physics in 2007. Fert and Grünberg found that the electrical resistance in these multilayers is smaller for parallel spin alignment than for antiparallel spin alignment [4]. A similar effect, based on the magnetization orientation of two magnetic layers separated by an insulator, is the tunneling magnetoresistance (TMR), discovered by M. Julliere in 1975 [5]. The phenomenology is similar to the GMR in that the resistance is dependent on the relative orientation of the magnetizations in the magnetic layers, but the effect is even larger. Therefore, the TMR effect is still used in read heads of hard disk drives [6].

The development of spin-based electronics lead to the research field of spintronics, where the central goal is the manipulation and transport of spins by electrical currents and voltages. Important progress has been made in the development of, e.g., nonvolatile memory devices, where the memory is retained even after removing power from the device. An example is the racetrack memory proposed by Stuart Parkin in 2008 [7], where the idea is to store information in magnetic domains of a ferromagnetic wire by moving them with an electrical current.

Another approach is the magnetoresistive random access memory (MRAM), which uses two ferromagnetic layers separated by a tunnel barrier to store data as bits [8] by utilizing the high and low resistivity configuration of the TMR effect. A further development is the so-called spin transfer torque magnetoresistive random access memory (STT-MRAM). This device uses polarized spin-currents to manipulate the spins in the magnetic layers to store data [9]. These two devices combine high read and write rates, nonvolatility and low energy consumption but they require high current densities which lead to Joule heating.

Current challenges in spintronics include the identification of novel material systems with enhanced domain wall mobility and low switching currents. With the recent discovery of the magnetic skyrmion lattice phase [10], a new class of materials with promising perspectives for spintronics is now available. Furthermore, spin-orbit torques that arise at the interface of a normal metal and a magnetic thin film can be used to switch the magnetization [11]. To study these materials and physical phenomena, it is necessary to understand the magnetization dynamics for different material systems. The magnetization dynamics of a material give information about its intrinsic properties such as Landè-factor, anisotropy and damping but also exchange coupling and spin pumping properties in magnetic multilayers [12]. Spin pumping is the mechanism of generating a spin current in a normal metal by driving the magnetization in an adjacent ferromagnet [13, 14].

Several measurement techniques to study the magnetization dynamics are available in the frequency range from GHz to a few hundred THz. An established method is the broadband ferromagnetic resonance (FMR) technique, which operates in the GHz regime. The broadband FMR uses a coplanar waveguide while earlier FMR experiments used a microwave cavity, which limits the experiments to a single microwave frequency. The coplanar waveguide instead allows to measure over a large frequency range, which is essential to extract magnetic damping and spin-orbit torque efficiencies. Furthermore it allows to study magnetization dynamics in chiral magnets in the frequency domain.

In this thesis, we investigate the magnetization dynamics in different magnetic materials relevant for spintronics using a broadband ferromagnetic resonance technique with a coplanar waveguide and a vector network analyzer (VNA). The VNA allows us to recover the full amplitude and phase information, which we exploit to quantify spin-orbit torques in normal metal/ferromagnet bilayers. We furthermore study a compensating ferrimagnet and an insulating chiral magnet, which hosts magnetic skyrmions. Exploring the fundamentally different dynamical properties of these systems motivated this work.

This thesis is structured as follows: In chapter 2, we start with an introduction into the basics of magnetization dynamics in an externally applied magnetic field. Afterwards, the ferromagnetic resonance observed when we apply an additional oscillating magnetic field perpendicular to the external magnetic field is discussed. The resulting response of the magnetization is described by the Polder susceptibility and the resonance condition is given by the Kittel equation, which will be introduced here.

In chapter 3, the so-called vector network analyzer ferromagnetic resonance setup (VNA-FMR) will be explained in detail. In particular, we discuss the detection scheme in a fully quantitative manner. As the VNA is a versatile instrument, two operation modes (linear frequency sweep and continuous wave mode) are discussed with regard to their applications for FMR spectroscopy. We furthermore show how the raw FMR signal can be distinguished from the background coming from the used microwave equipment, and how the FMR spectra can be fitted.

In chapter 4, we present an inductive measurement technique to quantify the room-temperature field- and damping-like spin-orbit torques (SOT) in three series of normal metal/ferromagnet bilayer samples by evaluating the amplitude and phase of the measured FMR signal using a VNA. Due to the phase-sensitive measurement it is possible to

distinguish between the damping- and field-like SOTs as they are in quadrature. The samples consist of the ferromagnet CoFeB interfaced with three different normal metal systems (namely TaAu, W and AuPt), where also the exact composition of the binary alloys is varied. The necessary processing steps required to extract the spin-orbit torque conductivity are described. From the spin-orbit torque conductivity we obtain the spin Hall angle. The experimentally determined spin Hall angles are in excellent agreement with theory and with results from two other measurement techniques, namely the harmonic Hall measurement (group of M. Meinert) and the THz emission spectroscopy (group of T. Kampfrath). In the AuPt/CoFeB samples we observe a maximum of the spin Hall angle which is two times larger than of pure platinum, for about 33% gold content. Additionally, a correlation between the Gilbert damping parameter and the damping-like SOT conductivity is found. For the W/CoFeB samples a correlation between the Gilbert damping parameter and the damping-like SOT conductivity and also between the Landè-factor and the field-like SOT conductivity is observed.

In chapter 5, the magnetization dynamics of the compensating ferrimagnet gadolinium iron garnet (GdIG) are investigated. The crystal structure of GdIG features three magnetic sublattices. This results in a so-called compensation temperature ($T_{\mathrm{comp}} \simeq 288\,\mathrm{K}$), where the sublattice magnetizations cancel each other out. The temperature-dependence of the sublattice magnetizations makes GdIG an ideal testing environment to investigate the ferrimagnetic (FMR) and the antiferromagnetic resonance (AFMR) close and far away from the compensation point. At the compensation point, the Landè-factor and the linewidth of the FMR diverge as predicted by theory. The antiferromagnetic resonance has in contrast to the ferromagnetic resonance a negative resonance frequency vs. magnetic field dispersion. The AFMR shifts to larger frequencies for decreasing temperature because the molecular exchange constant becomes also larger. Additionally, the strong and weak coupling between the FMR and AFMR and its dependence on the crystallographic direction along which the external magnetic field is applied, is discussed.

In chapter 6, we study the high frequency dynamics of the insulating chiral magnet Cu_2OSeO_3, which is a known skyrmion host material. Skyrmions are topologically protected spin solitons, which are observable below the critical temperature ($T_{\mathrm{c}} \simeq 59\,\mathrm{K}$). The theoretical calculation of M. Mochizuki [15] predicts a "melting" of the skyrmion lattice by driving the system with large microwave power. We test this prediction using two different measurement setups, namely the basic FMR setup with an amplifier and a 2-tone setup, where an additional frequency source and a directional coupler is used. In the basic FMR setup the excitation spectra do not show any changes in the different magnetic modes when applying large microwave power. In the 2-tone experiment, the skyrmion resonance signature is suppressed if a high power driving tone in the frequency range from 0.7 GHz to 1.0 GHz is applied by the frequency source. This has also been observed in small angle neutron scattering (SANS) experiments performed by the group of C. Pfleiderer.

Finally, in chapter 7, the most important experimental results are summarized and we give an outlook on possible future experiments that are based on the results obtained in this thesis.

Chapter 2

Ferromagnetic Resonance

Broadband magnetic resonance spectroscopy is a widely used and well-established experimental technique to probe materials with a magnetic ordering. Magnetic ordering occurs below a critical temperature and in the absence of a magnetic field. The interaction energy then overcomes the thermal energy and causes the magnetic moments depending of the type of interaction into an ordered state [16]. For ferromagnets and antiferromagnets, where all the magnetic moments are aligned either parallel or antiparallel, the Heisenberg exchange interaction [17] is responsible for the ordering. There also exist more complicated ordering phenomena like in a chiral magnet, which will be treated in chapter 6.

For the description of the dynamics of the magnetization and the ferromagnetic resonance, a classical, macroscopic approach is used. This is justified since the quantum numbers corresponding to the relevant energy levels are of the order of 10^{15} [18], which is a simple consequence of the correspondence principle [19]. Therefore the quantum-mechanical and the classical description lead to the same result [20].

First, the dynamics of a magnetization in an externally applied static magnetic field will be treated in section 2.1. By applying an additional oscillating magnetic field perpendicular to the static field leads to the ferromagnetic resonance. In section 2.2 the response of the system (Polder-susceptibility) as well as the Kittel-equations, which describe the resonance condition of the FMR, will be discussed.

2.1 Magnetization Dynamics

In order to get a first intuition of the magnetization dynamics, a single magnetic moment μ of an electron in an externally applied magnetic field $\mathbf{H}_0$ is considered. The magnetic field applies a torque $\mathbf{T}$ on the magnetic moment

$$\mathbf{T} = -\boldsymbol{\mu} \times \mu_0 \mathbf{H}_0, \tag{2.1}$$

which results in a precession of the magnetic moment around the magnetic field with a frequency

$$\omega = \gamma \mu_0 |\mathbf{H}_0|, \tag{2.2}$$

where ω is the angular frequency, $\mu_0 = 4\pi \times 10^{-7}\,\mathrm{V\,s/(A\,m)}$ is the vacuum permeability and

$$\gamma = \frac{g\,\mu_\mathrm{B}}{\hbar} \tag{2.3}$$

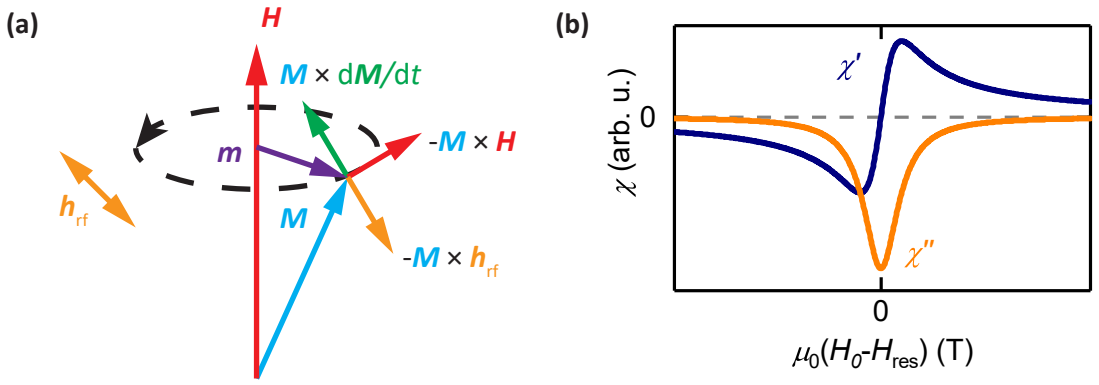

Figure 2.1: **(a)** Precessional motion of the magnetization $\mathbf{M}$ in an effective magnetic field $\mathbf{H}$ described by Eq. (2.9). The torque originating from the externally applied field is indicated in red and the damping torque which leads to an alignment of the magnetization to the equilibrium position ($\mathbf{M}||\mathbf{H}$) is drawn in green. The torque opposing the damping torque which is due to the additionally applied oscillating field $\mathbf{h}_{\mathrm{rf}}$, which is perpendicular to $\mathbf{H_0}$ and drives the magnetization away from its equilibrium position, is drawn in orange. **(b)** The real and imaginary part of the high-frequency susceptibility χ as a function of the externally applied magnetic field $\mu_0 H_0$. The susceptibility relates the magnetization perpendicular to the static magnetic field H_0 and the driving field $\mathbf{m} = \chi \mathbf{h}_{\mathrm{rf}}$.

is the gyromagnetic ratio with the Landè-factor g, the Bohr magneton μ_{B} and the reduced Planck constant $\hbar = h/2\pi$. The gyromagnetic ratio relates the magnetic moment with the angular momentum. From classical mechanics it is known that the torque is equal to the rate of change of angular momentum, Eq. (2.1) results in

$$\frac{\mathrm{d}\boldsymbol{\mu}}{\mathrm{d}t} = -\gamma\, \boldsymbol{\mu} \times \mu_0 \mathbf{H}_0, \tag{2.4}$$

which describes the dynamics of a single magnetic moment in an external magnetic field and is also called Larmor precession [21].

In a solid-state material the number of electrons are in the order of 10^{24}, so a continuum approach is done, where the single magnetic moments of the electrons $\boldsymbol{\mu}_i$ are added up to a macroscopic quantity called the magnetization

$$\mathbf{M} = \frac{1}{V} \sum_{\boldsymbol{\mu}_i \in V} \boldsymbol{\mu}_i, \tag{2.5}$$

where V is a finite volume of the sample. By simply plugging in this relation into Eq. (2.4), we get the so-called Landau-Lifshitz equation [22]

$$\frac{\mathrm{d}\mathbf{M}}{\mathrm{d}t} = -\gamma\, \mathbf{M} \times \mu_0 \mathbf{H}_0, \tag{2.6}$$

which describes an infinite precession in time of the magnetization around the magnetic field.

The projection of the magnetization $\mathbf{M}$ on the magnetic field vector $\mathbf{H}_0$ stays unchanged. So far no losses have been taken into consideration.

In 1955, T. Gilbert modified the Landau-Lifshitz equation and added a phenomenological damping parameter α [23], which then results in the Landau-Lifshitz-Gilbert equation (LLG)

$$\frac{\mathrm{d}\mathbf{M}}{\mathrm{d}t} = -\gamma\,\mathbf{M} \times \mu_0\mathbf{H} + \frac{\alpha}{M_{\mathrm{sat}}}\mathbf{M} \times \frac{\mathrm{d}\mathbf{M}}{\mathrm{d}t} \tag{2.7}$$

with the saturation magnetization M_{sat}. The magnetization precesses around the magnetic field and relaxes in a finite time to its equilibrium position, which is parallel to the applied magnetic field $\mathbf{M}||\mathbf{H}$, as depicted in Fig. 2.1**(a)**.

Note that the relevant magnetic field is not the externally applied magnetic field, but the effective magnetic field. The effective magnetic field contains the externally applied magnetic field as well as any anisotropy contributions. As a consequence of the dipolar interaction, the magnetic field outside and inside the sample are unequal. The calculation of these so called demagnetization fields can be very tedious for arbitrary sample shape. In our computation we limit our sample shapes to general ellipsoids and can write the internal magnetic field as

$$\mathbf{H}_{\mathrm{i}} = \mathbf{H}_0 - \overleftrightarrow{N}\mathbf{M} \tag{2.8}$$

with the demagnetization tensor $\overleftrightarrow{N}$. If the principle axes of the ellipsoid coincide with the axes of the coordinate system the tensor becomes symmetric and diagonal. Then only the three diagonal demagnetization factors are left, for which in general $N_x + N_y + N_z = 1$ holds. It is important to note that in literature and throughout this thesis the N_z component is always defined as the axis along which the externally applied magnetic field $\mathbf{H}_0$ is pointing.

Furthermore magneto crystalline anisotropy has to be taken into account. Anisotropy of a system is the dependence of properties depending on the direction of the magnetic field relative to a preferred direction [24]. The already mentioned demagnetization fields, which depend on the direction of the applied magnetic field with respect to the sample geometry, can also be referred as the shape anisotropy. The preferred axes of the magneto crystalline anisotropy instead are given by the crystal axes and therefore depend on the angle between the magnetization and these axes. For simplicity the angle dependence is neglected. Additionally, also interface anisotropies can be present. In order to account for all these anisotropy contributions, they are simply collected in a total anisotropy field H_{aniso}. The total magnetic field $\mathbf{H}$ is then given by

$$\mathbf{H} = \mathbf{H}_0 + \mathbf{H}_{\mathrm{aniso}} - \overleftrightarrow{N}\mathbf{M}. \tag{2.9}$$

The total magnetic field is then simply plugged into the LLG (Eq. (2.7)) and by solving this differential equation the full information of the magnetization dynamics of the system is obtained.

2.2 Ferromagnetic Resonance

In our experiments, we additionally apply an oscillating magnetic field $\mathbf{h}_{\mathrm{rf}}$ perpendicular to the static dc magnetic field $\mathbf{H}_0$ as shown in Fig. 2.1**(a)**, which acts as an perturbation for the system. This rf magnetic field exerts a torque, which points in the opposite direction of the damping torque and prevents the magnetization from decaying. In a simple driven harmonic oscillator model the precessing magnetization is driven by the rf magnetic field $\mathbf{h}_{\mathrm{rf}}$ and if the precessional frequency of the magnetization is hit with the rf field, an enhanced response should be observed, which is due to the fact that more energy is absorbed by the system.

In the following a schematical derivation of this response is shown and how the precessional frequency of the material is influenced by its properties will be discussed. A thorough derivation of the following calculation can be found in [24–28].

2.2.1 Polder-Susceptibility and Kittel-Equation

We start our discussion with a magnetization $\mathbf{M}$ of a finite size sample in an externally applied magnetic field along the z-axis $\mathbf{H}_0 = H_0\hat{\mathbf{e}}_z$ and an oscillating magnetic field $\mathbf{h}_{\mathrm{rf}}(t) = (h_{\mathrm{rf,x}}(t),h_{\mathrm{rf,y}}(t),0)$ perpendicular to it. First the magnetic field $\mathbf{H}$ and the magnetization $\mathbf{M}$ is split into a time-independent ($\mathbf{M}_0$, $\mathbf{H}_0$) and a time-dependent part ($\mathbf{h}_{\mathrm{rf}}(t)$, $\mathbf{m}(t)$):

$$\begin{aligned}\mathbf{H} &= \mathbf{H}_0 + \mathbf{H}_{\mathrm{aniso}} - N_z\mathbf{M}_0 + \mathbf{h}_{\mathrm{rf}}(t) = (H_0 + H_{\mathrm{aniso}} - N_z M_0)\,\hat{\mathbf{e}}_z + \mathbf{h}_{\mathrm{rf}}(t)\\ \mathbf{M} &= \mathbf{M}_0 + \mathbf{m}(t) = M_0\hat{\mathbf{e}}_z + \mathbf{m}(t).\end{aligned} \tag{2.10}$$

Furthermore the alternating parts are assumed to be harmonic, so it is possible to write them as

$$\begin{aligned}\mathbf{h}_{\mathrm{rf}}(t) &= \mathbf{h}_{\mathrm{rf,0}} \cdot e^{i\omega t}\\ \mathbf{m}(t) &= \mathbf{m}_0 \cdot e^{i\omega t}.\end{aligned} \tag{2.11}$$

The time-dependent parts are supposed to be smaller than the time-independent ones ($h_{\mathrm{rf,0}} \ll H_0$ and $m_0 \ll M_0$). The acquired equations are now simply plugged into the Landau-Lifshitz-Gilbert equation (Eq. (2.7)). In addition, the steady magnetization is supposed to point in its equilibrium position ($\mathbf{M}_0||\mathbf{H}_0$), which leads to $\mathbf{M}_0 \times \mathbf{H}_0 = 0$. By splitting the LLG into the three Cartesian coordinates, this results in

$$\begin{aligned}i\omega m_x &= \gamma\mu_0 M_0 \cdot (h_{\mathrm{rf,y}} - N_y m_y) - m_y \cdot (\gamma\mu_0 \cdot (H_0 + H_{\mathrm{aniso}} - N_z M_0) + i\omega\alpha)\\ i\omega m_y &= -\gamma\mu_0 M_0 \cdot (h_{\mathrm{rf,y}} - N_x m_x) + m_x \cdot (\gamma\mu_0 \cdot (H_0 + H_{\mathrm{aniso}} - N_z M_0) + i\omega\alpha)\\ i\omega m_z &= 0.\end{aligned} \tag{2.12}$$

One needs to keep in mind, that the time-varying components are also attenuated by the internal magnetic fields. In the Landau-Lifshitz-Gilbert equation the value of the equilibrium magnetization equals the saturation magnetization $M_0 = M_{\mathrm{sat}}$ as the length of this vector does not change [29]. As the last component $m_z = 0$, the first two equations

are rewritten into a matrix form and results in

$$\begin{pmatrix} m_{\mathrm{x}} \\ m_{\mathrm{y}} \end{pmatrix} = \overleftrightarrow{\chi} \begin{pmatrix} h_{\mathrm{rf,x}} \\ h_{\mathrm{rf,y}} \end{pmatrix} \tag{2.13}$$

with

$$\overleftrightarrow{\chi} = \frac{\mu_0 M_{\mathrm{sat}}}{\mathrm{Det}(A)} \underbrace{\begin{pmatrix} H_0 + H_{\mathrm{aniso}} + M_{\mathrm{sat}} \cdot (N_y - N_z) + \frac{i\omega\alpha}{\gamma\mu_0} & +\frac{i\omega}{\gamma\mu_0} \\ -\frac{i\omega}{\gamma\mu_0} & H_0 + H_{\mathrm{aniso}} + M_{\mathrm{sat}} \cdot (N_x - N_z) + \frac{i\omega\alpha}{\gamma\mu_0} \end{pmatrix}}_{\equiv A}, \tag{2.14}$$

which is also known as the Polder-susceptibility and was first derived by D. Polder in 1949 [30]. The susceptibility gives the response of the magnetization to a small (compared to the static magnetic field) rf magnetic field perpendicular to its equilibrium position and is generally a tensor of the second order, where its components are labeled as

$$\overleftrightarrow{\chi} = \begin{pmatrix} \chi_{xx} & \chi_{xy} \\ \chi_{yx} & \chi_{yy} \end{pmatrix}. \tag{2.15}$$

The susceptibility can be split into its real and imaginary part $\chi = \chi' + i\chi''$, where the real part χ' describes the dissipation and the imaginary part χ'' characterizes the absorption of the system. The typical lineshape of the susceptibility is shown in Fig. 2.1**(b)**. The absorption of the system χ'' has a typical Lorentzian lineshape, where the minimum indicates where the most energy is absorbed.

In the last step we want to calculate the resonance condition of the ferromagnetic resonance for a given static magnetic field. Solving $\mathrm{Det}(\overleftrightarrow{\chi}) \stackrel{!}{=} 0$ for the frequency $f = \omega/2\pi$ and taking the real part of the solution, we recover the famous Kittel equation

$$f = \frac{\gamma}{2\pi} \mu_0 \sqrt{(H_0 + H_{\mathrm{aniso}} + (N_x - N_z) \cdot M_{\mathrm{sat}}) \cdot (H_0 + H_{\mathrm{aniso}} + (N_y - N_z) \cdot M_{\mathrm{sat}})}, \tag{2.16}$$

which was first calculated by C. Kittel in 1948 [31]. This relation describes the resonance condition for a finite size (bulk) sample. We are also interested in thin film samples (thickness ∼nm), where we can deduce two special cases of Eq. (2.16). We assume the normal of the plane to point along the z-direction.

For the in-plane (ip) case the magnetic field $\mathbf{H}_0$ is pointing in the plane of the sample. Therefore the demagnetization factors are set to $N_x = 1$ and $N_y = N_z = 0$, so the in-plane Kittel-equation takes the following form:

$$f = \frac{\gamma}{2\pi} \mu_0 \sqrt{(H_0 + H_{\mathrm{aniso}}) \cdot (H_0 + H_{\mathrm{aniso}} + M_{\mathrm{sat}})}. \tag{2.17}$$

In the out-of-plane (oop) case the magnetic field $\mathbf{H}_0$ is parallel to the surface normal of the sample so the demagnetization factors become $N_x = N_y = 0$ and $N_z = 1$. In addition the anisotropy field H_{aniso} and the magnetization M_{sat} are combined to an effective magnetization $M_{\mathrm{eff}} = M_{\mathrm{sat}} - H_{\mathrm{aniso}}$ because in the fitting process it cannot be

distinguished between them. This results in the out-of-plane Kittel-equation

$$f = \frac{\gamma}{2\pi}\,\mu_0\,(H_0 - M_{\text{eff}}). \tag{2.18}$$

As seen from the definition of the Polder susceptibility (Eq. (2.14)), there exists an imaginary part in the diagonal elements, which contains the Gilbert damping parameter α. By solving the equation $\mathrm{Det}(\overleftrightarrow{\chi}) \stackrel{!}{=} 0$ for the magnetic field H_0, but this time taking the imaginary part of the solution, we can describe the linewidth

$$\Delta H_{\text{HWHM}} = \frac{\alpha\omega}{\mu_0\gamma}, \tag{2.19}$$

where ΔH_{HWHM} is the linewidth defined as half-width-at-half-maximum (HWHM). This equation phenomenologically accounts for all kind of contributions to the linewidth, which scale linearly with frequency. In our experiments we extract by fitting our FMR curve the full-width-at-half-maximum (FWHM) linewidth. Therefore we need to modify Eq. (2.19) by multiplying with a factor of 2 ($\Delta H_{\text{FWHM}} = 2 \cdot \Delta H_{\text{HWHM}}$). Moreover it is observed, that the curve does not intersect with the y-axis at 0 rather at a finite value. Therefore an offset is added to Eq. (2.19), which is called the inhomogeneous linewidth broadening ΔH_{inh}. Finally, we arrive at the full equation to describe the linewidth

$$\mu_0\Delta H_{\text{FWHM}} = \mu_0\Delta H_{\text{inh}} + 2 \cdot \frac{2\pi f\,\alpha}{\gamma}. \tag{2.20}$$

The origin of the damping can be quite manifold, like two-magnon scattering or Eddy-currents in metals, and is basically sample-dependent [29].

Chapter 3

Measurement Technique (VNA-FMR)

The investigation of the ferromagnetic resonance (FMR) has triggered the development of a multitude of experimental techniques in order to extract the high-frequency properties of a magnetic material. The ferromagnetic resonance can be used to determine the intrinsic parameters such as its damping characteristics [32], its magnetic anisotropies [33] or the interlayer exchange coupling of an magnetic multilayer [12]. In this work a so-called vector network analyzer ferromagnetic resonance (VNA-FMR) technique with a coplanar waveguide is used. Further measurement techniques also characterizing the FMR are the pulsed inductive microwave magnetometer (PIMM) [34], spin-torque ferromagnetic resonance (ST-FMR) [35] or ferromagnetic resonance with a frequency source and a Lock-in [36]. The big advantage of the VNA-FMR over the other methods is that it has a very high sensitivity and the ability to fully analyze the amplitude and the phase of the signal.

The VNA-FMR setup and its general working principle is discussed in section 3.1 . As the vector network analyzer is a versatile measurement device, one can perform VNA-FMR in two different measurement modes. These are the frequency-swept FMR, where the VNA operates in the linear frequency sweep mode, and the magnetic field-swept FMR, where the VNA is in the continuous wave mode. Both will be treated in sections 3.2 and 3.3 respectively. In these sections we further discuss how the background coming from the used microwave equipment in the setup (cable, endlaunches etc.) has to be subtracted in order to get the raw FMR-signal.

3.1 Experimental Setup VNA-FMR

The basic vector network analyzer ferromagnetic resonance (VNA-FMR) setup consists of three main parts: a coplanar waveguide (CPW), the vector network analyzer itself and an instrument to produce magnetic fields as depicted in Fig. 3.1.

Starting with the magnetic field, either an electromagnet is used, when performing room temperature experiments, or an superconducting 3D-vector magnet for cryogenic temperature experiments. The 3D vector magnet is assembled from two opposing coils in Helmholtz configuration and a solenoid, which are producing a homogeneous magnetic field by Amperè's law, when a current is flowing through the wires of the coils. The magnet is in a bath of liquid helium (boiling point $T = 4.2\,\mathrm{K}$). A disadvantage of the superconducting magnet is its slow slew rate. The room-temperature electromagnet uses an iron yoke to

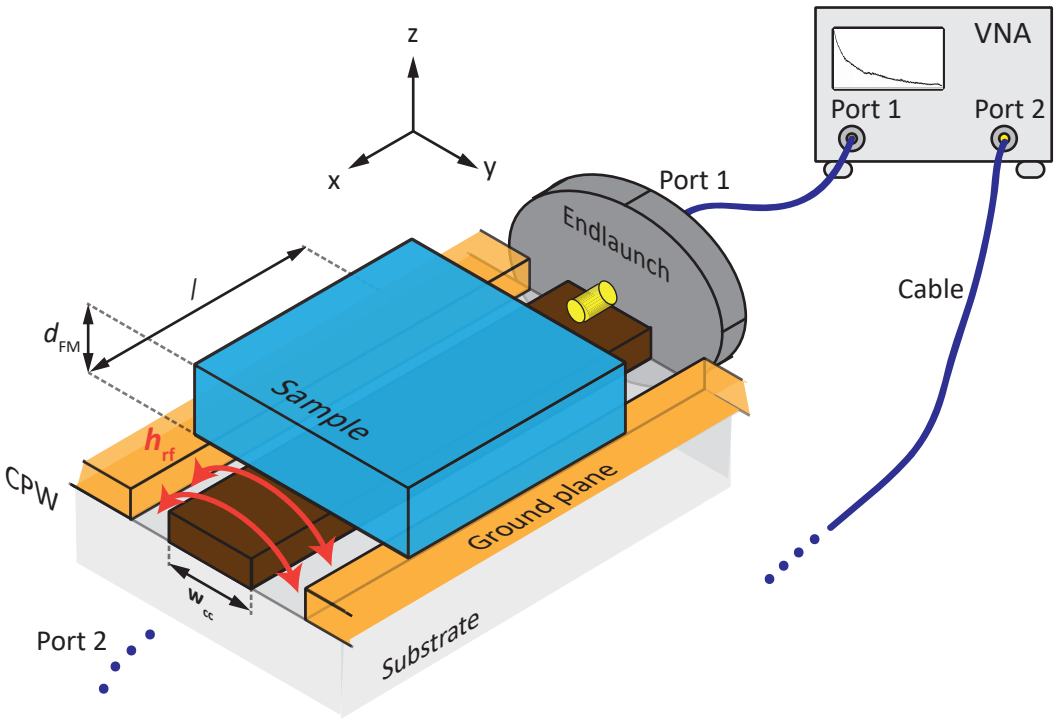

Figure 3.1: Schematic experimental vector network analyzer setup for ferromagnetic resonance (VNA-FMR). The sample (thickness d_{FM}, length l) is placed flip-chip style on the coplanar waveguide (CPW) and is solely inductively coupled to it. The oscillating magnetic field $\mathbf{h}_{\mathrm{rf}}$ is produced by the frequency source of the vector network analyzer (VNA) by applying a sinusoidal microwave to the cables, which is then coupled into the center conductor (in brown) via the endlaunch connectors (front connector not shown for clarity).

produce magnetic inductions with fast slew rates up to 3 T along a single axis. The field resolution is for both systems in general better than 0.5 mT.

The vector network analyzer (VNA) is a device to fully characterize an electrical rf circuit. In a simple picture, a network analyzer produces a wave with frequency f at port 1 and measures the transmitted wave with the same frequency at port 2 after travelling through the rf circuit. A scalar network analyzer only measures the amplitude difference between these waves, in contrast to the vector network analyzer, which additionally measures the phase [37]. From the amplitude and the phase the VNA calculates the complex S-parameters. In our measurements, we are interested in the change of transmission as the sample absorbs energy, if the FMR resonance condition is fulfilled. Therefore we measure the complex transmission parameter S_{21}, which is simply defined as the ratio between the incident wave at port 2 and the outgoing wave at port 1

$$S_{21} = \frac{V_2}{V_1} = \frac{|V_2|}{|V_1|} e^{i(\phi_2 - \phi_1)}, \tag{3.1}$$

where V_i are the measured voltages, which are complex quantities. These complex variables are described by their magnitude $|V_i|$ and a complex phase factor $e^{i\phi_i}$. The transmission parameter S_{21} consists of the transmission change ΔS_{21} coming from the sample and the background S_{21}^0 originating from the frequency-dependent transmission of the setup. The transmission change ΔS_{21} can be written as

$$\Delta S_{21} = \frac{S_{21} - S_{21}^0}{S_{21}^0}. \tag{3.2}$$

In our measurements, we assume to have a fully impedance matched rf circuit of $Z_0 = 50\,\Omega$ in order to neglect the back reflected wave in the system ($S_{11} = 0$). In general this assumption does not hold, but the data analysis that we describe below, remains valid in the limit of $|S_{11}| \ll 1$, which is generally the case.

The amplitude of the outgoing wave can be adjusted by changing the power level of the frequency source of the VNA. The software of the VNA then performs a full phase and amplitude analysis after detecting the signal in a heterodyne measurement scheme. In order to reduce the noise figure, it is possible to adjust the IF bandwidth. The smaller the IF bandwidth is chosen, the less broadband noise is detected at the cost of extended measurement time. Therefore we choose our IF bandwidth such, that it gives a good balance between an adequate Signal-to-Noise ratio and reasonable measurement time. An extensive discussion of the working principle of a VNA can be found in [37].

The last part is the coplanar waveguide, which consists of a metallic thin film, which is deposited on a low loss dielectric substrate, and two electrodes parallel to it, which are also deposited on the same surface and connected to a common ground [38]. The transmission line in the middle is the so-called center conductor and is responsible for the transportation of the induced microwave in a TEM-mode. The microwave in the center conductor generates due to Ampere's law an elliptical rf magnetic field h_{rf} in the y,z-plane because of the finite width w_{cc} of the transmission line, which is typically in the range of µm to mm. This generated magnetic field can be quantitatively calculated with the Karlqvist equations [27, 39, 40]

$$h_y(y,z) = \frac{1}{\pi}\frac{I}{2w_{\mathrm{cc}}}\left(\arctan\left(\frac{y+\frac{w_{\mathrm{cc}}}{2}}{z}\right) - \arctan\left(\frac{y-\frac{w_{\mathrm{cc}}}{2}}{z}\right)\right) \tag{3.3}$$

$$h_z(y,z) = \frac{1}{2\pi}\frac{I}{2w_{\mathrm{cc}}}\ln\left(\frac{\left(y+\frac{w_{\mathrm{cc}}}{2}\right)^2 + z^2}{\left(y-\frac{w_{\mathrm{cc}}}{2}\right)^2 + z^2}\right), \tag{3.4}$$

where the term $I/(2w_{\mathrm{cc}})$ describes the magnetic field, which is produced by an infinite sheet with a current I. The current I in the center conductor of the CPW can be related to the applied power P by $I = \sqrt{P/Z_0}$. The geometry of the center conductor is chosen in a way, that the impedance of the CPW equals $50\,\Omega$ in order to match the impedance of the whole system, so no back-reflecting waves are produced.

The vector network analyzer is connected with the coplanar waveguide using cables and two endlaunche connectors at each side of the CPW. The endlaunches couple the microwave,

produced by the frequency source of the VNA, into the center line. Consequently the center conductor produces the oscillating magnetic field h_{rf} with a frequency f given by the VNA.

In the experiment, the sample is placed flip-chip style onto the CPW and is purely inductively coupled to the coplanar waveguide. By applying a static magnetic field H_0 in an arbitrary direction, the magnetization of the sample is orientated and the magnetization starts to precess with a frequency according to the Kittel equation (Eq. (2.16)). The CPW acts here as an excitation as well as a detection transducer, in a way that it drives the excitation torque on the precessing magnetization with a oscillating magnetic field $\mathbf{h}_{\mathrm{rf}}$ as well as it detects the additional current, which is induced by the precessing magnetization in the sample into the CPW due to Faraday's law. If the applied frequency of the VNA matches the resonance frequency of the precession of the magnetization, the induced current opposes the excitation current, such that microwave power is absorbed.

The coupling between the CPW and the AC magnetic field produced by the precessing magnetization can be calculated by assuming a simple voltage divider model, where we have the resistance of our impedance matched system of $Z_0 = 50\,\Omega$ and the inductance of the sample L_0 in series. As a result we acquire for the transmission parameter

$$\Delta S_{21} = \frac{1}{2}\,\frac{-i\omega L_0}{Z_0 - i\omega L_0}, \tag{3.5}$$

where the factor 1/2 occurs due to the fact that the measured voltage at port 2 V_2 is measured between the CPW signal and ground and not between port 1 and 2 [41]. The inductance of the sample is given by [40, 41]

$$\begin{aligned} L_0 = \frac{\mu_0 M_{\mathrm{sat}} l}{w_{\mathrm{cc}} d_{\mathrm{FM}} I^2} & \left(\int_{-\infty}^{+\infty} \mathrm{d}y \int_{\delta_{\mathrm{sl}}}^{\delta_{\mathrm{sl}}+d_{\mathrm{FM}}} \mathrm{d}z \, \left(\mathbf{q}(y,z) \overleftrightarrow{\chi}(\omega,H_0) \mathbf{h}_{\mathrm{rf}}(y,z,I) \right) \right) \\ & \cdot \left(\int_{-\infty}^{+\infty} \mathrm{d}y \int_{\delta_{\mathrm{sl}}}^{\delta_{\mathrm{sl}}+d_{\mathrm{FM}}} \mathrm{d}z \, \left(\mathbf{q}(y,z) \mathbf{h}_{\mathrm{rf}}(y,z,I) \right) \right) \end{aligned} \tag{3.6}$$

$$= \frac{\mu_0 l d_{\mathrm{FM}}}{4 w_{\mathrm{cc}}}\, \chi_{yy}(\omega,H_0)\, \eta^2(\delta_{\mathrm{sl}},w_{\mathrm{cc}}), \tag{3.7}$$

where the geometry shown in Fig. 3.1 is used and additionally a finite spacing δ_{sl} between the sample and the CPW (not shown in figure) is taken into account. Furthermore we have used in the last step, that the sample is a thin film ($d_{\mathrm{FM}} \simeq$ nm) and that the magnetic field $\mathbf{H}_0$ is applied in the out-of-plane (oop) direction because the precession of the magnetization becomes circular in the xy-plane and only the y-component of the oscillating magnetic field $h_{\mathrm{rf,y}}$ has to be taken into consideration. If the static magnetic field is applied in the in-plane direction (e.g. x-direction) then both components of $\mathbf{h}_{\mathrm{rf}}$ contribute as the precession movement of the magnetization becomes elliptic [29]. This simplification of an out-of-plane applied magnetic field will be used frequently, as we are only interested in the quantitative evaluation of the signal amplitude in chapter 4, where the magnetic field is applied out-of-plane.

In Eq. (3.6), l describes the effective length of the sample on the CPW and $\mathbf{q}(y,z)$ is the normalized spatial amplitude of the uniform excitation mode (FMR), where $\mathbf{q}(y,z) = 1$ holds. The integrated amplitude of the excited mode as a consequence of the field excitation is quantified by the first term in Eq. (3.6) and the integrated sensitivity of the waveguide, which inductively detects the excited mode, is described by the second term [40].

Between the two equal signs in Eqs. (3.6) and (3.7), we assumed that the rf driving field $\mathbf{h}_{\mathrm{rf}}$ to be uniform over the whole sample and that the magnetic field is applied out-of-plane so only the y-component $h_{\mathrm{rf,y}}$ contributes. Therefore the rf field, described by the Karlqvist equation (Eq. (3.3)), can be simplified to

$$h_{\mathrm{rf,y}}(I,\delta_{\mathrm{sl}}) \cong \frac{I}{2w_{\mathrm{cc}}}\eta(\delta_{\mathrm{sl}},w_{\mathrm{cc}}) \quad \text{with } \eta(\delta_{\mathrm{sl}},w_{\mathrm{cc}}) = \frac{2}{\pi}\arctan\left(\frac{w_{\mathrm{cc}}}{2\delta_{\mathrm{sl}}}\right). \tag{3.8}$$

For the in-plane case, the sum of the diagonal elements of the susceptibility $\chi_{\mathrm{xx}} + \chi_{\mathrm{yy}}$ would occur in Eq. (3.7).

Now the question arises: What is really measured at port 2 of the VNA? As already mentioned, we have to deal with losses in the whole setup coming from the cables, endlaunches and impedance mismatch due to the sample on the CPW, which can be magnetic field as well as temperature-dependent. These losses are collected in the frequency-dependent background transmission parameter $S_{21}^0(\omega)$. The total transmission parameter can be quantified by simplifying Eq. (3.5) under the assumption $\omega L_0 \ll Z_0$, which leads to $\Delta S_{21} = -i\omega L_0/(2Z_0)$, and using Eq. (3.2). Therefore, we obtain

$$\begin{aligned} S_{21}(\omega,H_0) &= S_{21}^0(\omega) + S_{21}^0(\omega)\cdot\Delta S_{21} = S_{21}^0(\omega) + S_{21}^0(\omega)\cdot\frac{-i\omega L_0}{2Z_0} \\ &= S_{21}^0(\omega) - S_{21}^0(\omega)\cdot i\omega\,\frac{1}{2Z_0}\,\frac{\mu_0 l d_{\mathrm{FM}}}{4w_{\mathrm{cc}}}\,\chi_{\mathrm{yy}}(\omega,H_0)\,\eta^2(\delta_{\mathrm{sl}},w_{\mathrm{cc}}) \\ &= S_{21}^0(\omega) - iAe^{i\phi}\chi_{\mathrm{yy}}(\omega,H_0), \end{aligned} \tag{3.9}$$

where A comprises all the constants and ϕ is a phase, which is due to the finite electrical length of the system. This phase appears due to the background S_{21}^0.

In the experiment we use two different procedures in order to investigate the magnetization dynamics of the material. On the one hand either the microwave frequency is set to a fixed value and the magnetic field is swept through the FMR or on the other hand the magnetic field is fixed at a certain value and the frequency of VNA is swept through the FMR. The first one is referred to as the “field-swept FMR”, where the VNA is set into the continuous wave (cw) mode, and the second one is called the “field-swept FMR”, where the VNA operates in the linear frequency sweep mode. In the following sections, these two measurement procedures will be discussed in more detail.

3.2 Continuous Wave Mode

In field-swept FMR the frequency of the VNA is fixed and the magnetic field is varied and swept through the ferromagnetic resonance condition. The vector network analyzer is therefore set into the continuous wave mode (cw-mode) and the IF bandwidth is set small (typically a few Hz). For various fixed frequencies f this protocol is repeated. In order to derive a fitting formula for fixed frequency, we restrict ourselves to the out-of-plane case of a thin film. We will see later, that this assumption does only affect the amplitude but nonetheless gives the correct resonance position and linewidth.

The susceptibility (Eq. (2.14)) takes for the out-of-plane case ($N_x = N_y = 0$, $N_z = 1$) the following form

$$\overleftrightarrow{\chi}_{\text{oop}} = \frac{\mu_0 M_{\text{sat}}}{\sqrt{(H_0 - M_{\text{eff}})^2 - \left(\frac{\omega}{\gamma\mu_0}\right)^2 - i\Delta H(H_0 - M_{\text{eff}})}} \begin{pmatrix} H_0 - M_{\text{eff}} + \frac{i\Delta H}{2} & +\frac{i\omega}{\gamma\mu_0} \\ -\frac{i\omega}{\gamma\mu_0} & H_0 - M_{\text{eff}} + \frac{i\Delta H}{2} \end{pmatrix}$$

$$\text{with } M_{\text{eff}} = M_{\text{sat}} - H_{\text{aniso}} \quad \text{and} \quad \frac{\Delta H}{2} = \frac{\omega\alpha}{\gamma\mu_0}. \tag{3.10}$$

For the out-of-plane case, we only need to take the χ_{yy}-component of the Polder-susceptibility (Eq. (3.10)). To correct the background Nembach *et al.* [42] proposed to introduce a phenomenological, linear complex function. Therefore S_{21}^0 can be written as $S_{21}^0(H_0) = C_0 + C_1 \cdot H_0$, where C_0 and C_1 are complex parameters. Plugging this into the already derived form of the transmission parameter S_{21}, Eq. (3.9) leads to

$$S_{21}(H_0)|_\omega = C_0 + C_1 \cdot H_0 - iAe^{i\phi} \frac{\mu_0 M_{\text{sat}} \cdot \left(H_0 - M_{\text{eff}} + \frac{i\Delta H}{2}\right)}{\sqrt{(H_0 - M_{\text{eff}})^2 - \left(\frac{\omega}{\gamma\mu_0}\right)^2 - i\Delta H(H_0 - M_{\text{eff}})}}. \tag{3.11}$$

It is intuitive from Eq. (3.11) that the resonance field H_{res} has a mutual dependence on both the gyromagnetic ratio γ and the effective magnetization M_{eff}. Therefore it is convenient to replace the effective magnetization by the resonance condition (Eq. (2.18), oop-Kittel equation) and setting the g-factor fixed to $g = 2.0$ and consequently fixing γ (see Eq. (2.3)). It was shown by Nembach *et al.* [42] that this is without consequences for the resonance field H_{res} as well as the linewidth ΔH.

In the final step we divide the susceptibility by the saturation magnetization $\mu_0 M_{\text{sat}}$ and collect the terms belonging to the susceptibility for more clearness again, which leads to the final result

$$S_{21}(H_0)|_\omega = C_0 + C_1 H_0 - iAe^{i\phi} \frac{\chi_{\text{yy}}(H_0)}{\mu_0 M_{\text{sat}}}. \tag{3.12}$$

In the fitting process, we extract the background parameters C_0 and C_1, the amplitude A, the phase ϕ, the resonance magnetic field $\mu_0 H_{\text{res}}$ and the linewidth $\mu_0 \Delta H$. It is important to note that this fitting formula can also be used for bulk samples and in-plane applied magnetic field. This results in the correct resonance field as well as correct linewidth, although the resulting amplitude has no direct physical meaning.

For the derivation of the fitting formula for an in-plane applied magnetic field, it would

be necessary to go back to Eq. (3.6) and take both components of the rf magnetic field $\mathbf{h}_{\mathrm{rf}}$ into account, which would lead in Eq. (3.7) and (3.9) to the occurrence of $h_{\mathrm{x}}\chi_{\mathrm{xx}} + h_{\mathrm{y}}\chi_{\mathrm{yy}}$ as the ellipticity of the precessional motion of the magnetization has to be considered.

3.3 Linear Frequency Sweep and Derivative Divide vs. Divide Slice

In this measurement protocol, the external magnetic field $\mu_0 H_0$ is fixed and the frequency f of the vector network analyzer is swept through the ferromagnetic resonance and the complex transmission parameter S_{21} is measured. This procedure is repeated for a series of fixed magnetic fields, where the step size between two values is generally fixed. As discussed before, when measuring the complex transmission parameter S_{21}, the frequency-dependent background coming from the setup is always superimposing the signal of the ferromagnetic resonance. The magnitude of the raw measured S_{21} parameter is shown in Fig. 3.2**(a)**. It is quite obvious that the signal coming from the FMR is small and can be even much smaller. Also in the field cut at 0.5 T shown in Fig. 3.2**(d)**, the expected FMR is weakly visible at 15 GHz. A possibility to remove the frequency-dependent background, would be to calibrate the whole microwave network [43]. Typically such a calibration is tedious and insufficient as the background can be magnetic field- and temperature-dependent.

In order to overcome this problem, a more sophisticated approach is necessary. One solution is to take a field cut at a fixed magnetic field far away from the ferromagnetic resonance, where we assume to only measure the transmission of the system and no contribution from the investigated sample, and divide the measured complex transmission parameter S_{21} by it. Therefore e.g. $S_{21}/S_{21}^{\mu_0 H_0 = 3.0\,\mathrm{T}}$ is calculated and the result is shown in Fig. 3.2**(b)**. The FMR can be seen as a deviation from the background, so it is now more pronounced. The field cut at 0.5 T shown in Fig. 3.2**(e)** shows the typical signature of the FMR susceptibility as already emphasized in Fig. 2.1**(b)**. In order to derive a fitting formula, we assume that by dividing by a magnetic field far away from the resonance, the whole background is taken care of, so consequently S_{21}^0 drops out of Eq. (3.9) with the final result

$$S_{21}^{ds}(\omega)|_{H_0} = 1 - iA' e^{i\phi}\chi(\omega, H_0), \tag{3.13}$$

where a new amplitude factor $A' = A/S_{21}^0$ is introduced.

Another solution is to use a processing method called “derivative divide”, which was developed at the Walther-Meißner-Institut [43] and is shown in Fig. 3.2**(c)**. The idea is to calculate the symmetric difference quotient of the transmission parameter S_{21} with respect to the magnetic field H_0, which results in

$$\begin{aligned} \mathrm{d_D}S_{21} &= \frac{S_{21}(\omega, H_0 + \Delta H_{\mathrm{mod}}) - S_{21}(\omega, H_0 - \Delta H_{\mathrm{mod}})}{S_{21}(\omega, H_0)\Delta H_{\mathrm{mod}}} \\ &= -iA\,\frac{\chi(\omega, H_0 + \Delta H_{\mathrm{mod}}) - \chi(\omega, H_0 - \Delta H_{\mathrm{mod}})}{\Delta H_{\mathrm{mod}}} + \mathcal{O}(A^2). \end{aligned} \tag{3.14}$$

In order to denote the usage of derivative divide, it is labelled throughout this work as $\mathrm{d_D}$.

From the general definition of the symmetric difference quotient, we get the freedom to set the finite step size ΔH_{mod}. Division by S_{21} in Eq. (3.14) cancels the transmission and phase of the background $S_{21}^{0}(\omega)$. If the chosen field step H_{mod} is small, the symmetric difference quotient can be approximated by the derivative with respect to the external magnetic field H_0:

$$\mathrm{d_D}S_{21} \approx -iA\,\frac{\mathrm{d}\chi}{\mathrm{d}H_0} = -iA''\,\frac{\mathrm{d}\chi}{\mathrm{d}\omega}. \tag{3.15}$$

For small field steps the field derivative is equal to the frequency derivative, as χ varies smoothly with field and frequency if the modulation amplitude H_{mod} is chosen small enough [43]. For the equal sign, a new amplitude A'' is introduced, which includes the conversion factor $(\mathrm{d}\omega/\mathrm{d}H_0)$. Generally we are not interested in the precise evaluation of the amplitude.

A big advantage of derivative divide is, that it suppresses the variations of the background and features in the data, which vary way faster or slower than the expected FMR linewidth as it quasi-imitates a field modulation. In order to now derive a fitting formula, the distortion of the linewidth due to the modulation amplitude has to be taken into account and therefore the central difference quotient is fitted in the frequency space

$$\mathrm{d_D}S_{21}|_{H_0} = -iA''\,\frac{\chi(\omega+\Delta\omega_{\mathrm{mod}}) - \chi(\omega-\Delta\omega_{\mathrm{mod}})}{2\Delta\omega_{\mathrm{mod}}} \tag{3.16}$$

with $\Delta\omega_{\mathrm{mod}} \approx \gamma\mu_0\Delta H_{\mathrm{mod}}$. A field cut at 0.5 T using derivative divide is shown in Fig. 3.2**(f)** with the corresponding fits according to Eq. (3.16).

Derivative divide has another large advantage over the divide slice method: By simply looking at the shape of the resonance at a field slice, it is possible to extract the resonance frequency vs. magnetic field dispersion of the resonance. The real part $\mathrm{Re}(\mathrm{d_D}S_{21})$ will have a dip-peak shape for positive dispersion and a peak-dip shape for negative dispersion. This is discussed in more detail in chapter 6.

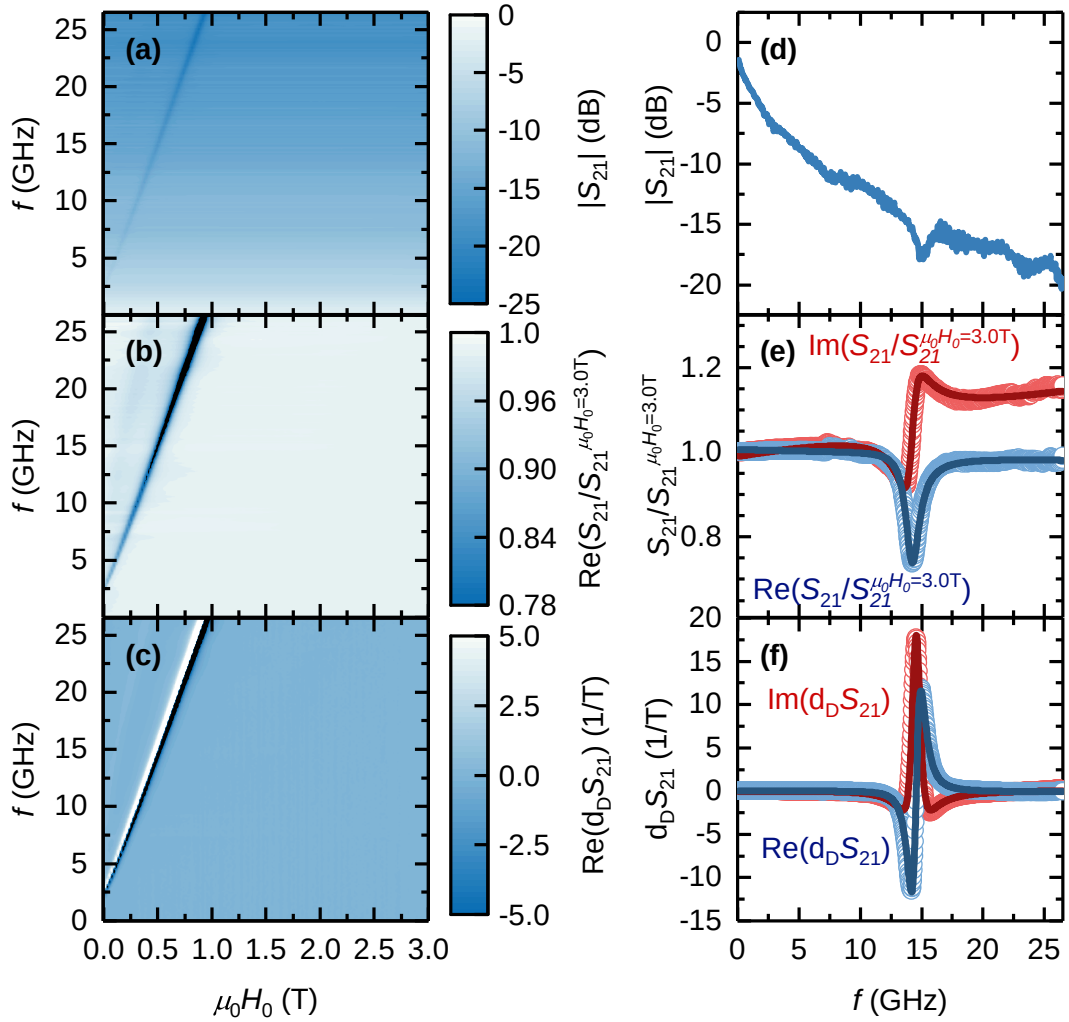

Figure 3.2: Acquired data of a typical frequency-swept FMR measurement for a gadolinium iron garnet (GdIG) single crystal (see chapter 5). **(a)** Magnitude of the complex transmission parameter S_{21} with a logarithmic scale, where the ferromagnetic resonance is barely visible and mainly the frequency-dependent background is observed. **(b)** Real part of the transmission parameter S_{21}, which is divided at a field far away from the FMR ($\mu_0 H_0 = 3.0\,\mathrm{T}$) in order to eliminate the background coming from the microwave setup. **(c)** Real part of the transmission parameter $\mathrm{d_D}S_{21}$ using derivative divide. **(d)** Transmission of the system at 0.5 T, where the FMR is barely visible at $f \approx 15\,\mathrm{GHz}$. **(e),(f)** Field cuts at $\mu_0 H_0 = 0.5\,\mathrm{T}$ of the divide slice and the derivative divide method respectively including fits (solid lines), using Eqs. (3.13) and (3.16) respectively, of the real and imaginary part of the transmission parameter.

Chapter 4

Spin-Orbit Torques in Ferromagnet/Normal Metal Bilayers

In the development of novel spintronic devices, such as memories or logic devices, so-called spin-orbit torques (SOT) are of high interest. Direct spin-orbit torques allow to drive magnetization precession in ferromagnetic materials by electric fields. In the reciprocal process, the magnetization precession leads to an electrical current, due to inverse spin-orbit torques (iSOT) [41]. In 2011, Miron *et al.* [11] first demonstrated, that these spin-orbit torques can be used to switch a perpendicular magnetized bilayer by applying an in-plane current.

The origins of these torques are manifold and can be phenomenologically divided into two groups: damping-like and field-like. The terminology originates from the direction in which these torques are acting. The damping-like torque leads, as the name suggests, to a relaxation of the magnetization to its equilibrium position. The symmetry of this torque is odd under time-reversal. In contrast, the field-like torque leads to a magnetization precession with the symmetry of that caused by an applied magnetic field. The field-like torque is even under time-reversal [14, 41]. Both torques are perpendicular to the magnetization (see Fig. 2.1).

The coupling between the spin of the electron in the ferromagnetic material and its orbital angular momentum plays a crucial role, when discussing effects in coupled ferromagnet/normal metal systems. This coupling is known as the spin-orbit coupling (SOC), as discussed in the context of atomic physics [44]. Spin-orbit interaction is especially prominent in heavy metals (Pt, Ta). The microscopic effects giving rise to these spin-orbit torques are manifold. As an example, a current flowing in the normal metal induces a spin current flowing into the ferromagnetic layer with spin polarization orthogonal to both, charge current flow and interface normal directions. This effect is known as the spin Hall effect (SHE) [45] and is leading to a damping-like torque [14, 46].

The spin Hall effect is quite analogous to the "classical" Hall effect, where the Lorentz force due to the applied magnetic field deflects charges with opposite sign to opposite sample boundaries resulting in a charge separation and consequently to a voltage. The spin Hall effect converts an unpolarized charge current into a chargeless spin current transverse to it. This can only occur in a system with a large spin-orbit interaction. In the extrinsic spin Hall effect, the scattering at impurities leads to an anisotropic scattering cross section for the two spin directions. These extrinsic effects are represented by the Mott or Skew

scattering and the Side-Jump scattering. The band structure itself might also lead to the spin Hall effect as the spin-orbit coupling causes a spin-dependent transverse velocity. This effect is referred to as the intrinsic spin Hall effect [45, 47, 48].

Another mechanism assumes a charge transport at the normal metal/ferromagnet interface, where the two layers are modelled as two dimensional. The so-called Rashba-model results in a direct coupling of the magnetization and the flowing current at the interface. The effect is known as the Rashba-Edelstein effect (REE) [49, 50] and leads to a field-like torque with an even time-reversal symmetry [14, 41].

The Onsager reciprocity [51] provides a description to relate the forward and the inverse process to produce magnetic torques or current flow in a FM/NM system by electric field or magnetization dynamics. A simple example for Onsager reciprocity in this system is found from Faraday's and Ampère's law: A precessing magnetization in the ferromagnet induces a current in the normal metal (Faraday's law). A current in the normal metal produces an Oersted field (Ampère's law), which acts on the magnetization in the ferromagnet [41]. This is important to note here, as the experiments explained in the following measure the forward process in contrast to our method, which will test the inverse process as discussed in section 4.1.

Several methods to quantify spin-orbit torques have been established. One example is the setup used by Miron *et al.* [11], where a Hall-bar is structured onto the normal metal. A current is then applied along a certain direction of the Hall-bar and the voltage perpendicular to the current is measured. This is the so-called Hall-voltage and quantifies the (damping-like) torque coming from the spin Hall effect. This measurement method is completely DC. In a complimentary approach, it is also possible to pattern the bilayer into a strip and measure the DC voltage V_{SH} due to spin pumping and the spin Hall effect.

As shown by Weiler *et al.* [52] it is also possible to measure the AC spin Hall effect in an analogous fashion, as shown in Fig. 4.1**(a)**. The challenge here is to pattern the sample with an impedance matching that of the microwave network in order to prevent back-reflection. This makes the measurement of the AC inverse spin Hall effect more technically challenging than the DC iSHE measurement.

In this chapter, we demonstrate, that the inverse spin-orbit torques (iSOT) of a bilayer system consisting of a normal metal and ferromagnet can also be detected using an inductive method, which does not require any patterning of the sample or any impedance matching. In our experiments, the ferromagnet remains always the same (CoFeB) while the normal metal is varied between three different systems (TaAu, W, AuPt), where also the exact composition of the binary alloys is varied. In section 4.1 we discuss the experimental setup and compare it to the already established methods. Additionally we discuss the advantages of our approach. The obtained experimental results are presented in section 4.2. Finally, in section 4.3 we compare our findings with two other well established methods: Harmonic Hall and THz spectroscopy. The harmonic Hall measurements were performed in the group of Markus Meinert (University of Bielefeld) and the THz measurement in the group of Tobias Kampfrath (Fritz Haber Institut of the Max Planck Society, Berlin).

4.1 Experimental Setup

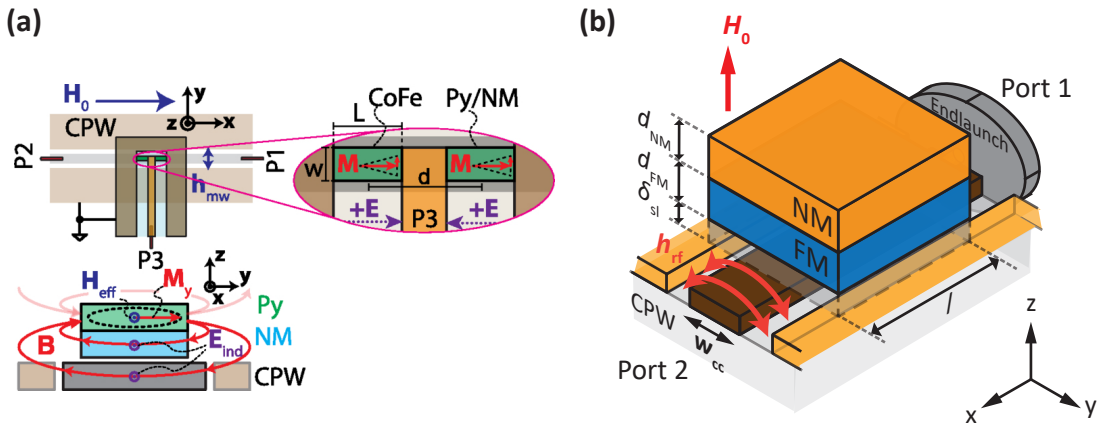

Figure 4.1: Typical experimental setups to quantitatively measure spin-orbit torques. **(a)** AC spin Hall measurement, where an additional detection coplanar waveguide with an impedance matching that of the microwave network is patterned onto the sample. Figure is taken from [52]. **(b)** Our inductive measurement technique using a phase-sensitive FMR setup, where the sample is simply placed flip-chip style onto the CPW and the complex transmission parameter S_{21} is measured.

In this chapter we are interested in the quantification of the spin-orbit torques of normal metal/ferromagnet bilayer samples. All investigated samples were fabricated in the group of Markus Meinert at the University of Bielefeld using a sputtering technique. Using glas as the substrate (size $10 \times 10\,\mathrm{mm}^2$), first the normal metal (thickness $d_{\mathrm{NM}} = 3\,\mathrm{nm}$) and then the ferromagnet ($d_{\mathrm{FM}} = 3\,\mathrm{nm}$) was sputtered onto the substrate. The normal metal and the ferromagnet are therefore in direct contact. Finally a thin layer of tantalum (1 nm) was sputtered as a capping layer, in order to prevent oxidation. The thickness of each layer remained unchanged for all samples. The rectangular thin film on the substrate has a length of $l = (8.7 \pm 0.1)\,\mathrm{mm}$ and a width of $(4.7 \pm 0.1)\,\mathrm{mm}$.

The ferromagnet used throughout all the samples was the metallic cobalt-iron-bor alloy (CoFeB), which is a widely used material in spintronics. For the saturation magnetization of CoFeB a value of $\mu_0 M_{\mathrm{sat}} = 1.05\,\mathrm{T}$ is used. For the normal metal, three different material systems were used: $\mathrm{Ta}_x\mathrm{Au}_{1-x}$ and $\mathrm{Au}_x\mathrm{Pt}_{1-x}$, with $0 \leq x \leq 1$, and W_x, where x is the inverse sputtering power $1/P_{\mathrm{dep}}$.

The variation of the sputtering power for the wolfram films with a constant background O_2-pressure, allows to control the oxidation of the wolfram. For small sputtering power ($1/P_{\mathrm{dep}}$ large), the wolfram has more time to oxidate with the oxygen in the sputtering chamber and as a consequence forms W(O)x. If the sputtering power is larger ($1/P_{\mathrm{dep}}$ small), the wolfram does not oxidise completely and forms β-W. In the sample series only one sample is claimed to be pure wolfram ($1/P_{\mathrm{dep}} \approx 0$) and is denoted as "W" in contrast to the the oxidized wolfram samples, which are identified as "W(O)x".

In our experiments, we used a VNA-FMR setup at room-temperature as described in chapter 3. The samples were placed with the film-side down onto the coplanar waveguide

(center conductor width $w_{\mathrm{cc}} = 56\,\mu\mathrm{m}$) as shown in Fig. 4.1**(b)**, which is utilized both as an excitation and a detection transducer. The sample is therefore solely inductively coupled to the CPW. The used vector network analyzer Agilent N5224A PNA is capable of frequencies up to 43.5 GHz. An electromagnet at room-temperature is used, which is able to produce magnetic fields up to 2.9 T. The magnetic field configuration is out-of-plane, where the static magnetic field $\mathbf{H}_0$ is applied perpendicular to the CPW.

For all measurements, we are using the field-swept FMR, where the microwave frequency of the VNA is fixed and the magnetic field is swept through the FMR, as already explained in section 3.2. We measure the complex transmission parameter S_{21} for frequencies $5\,\mathrm{GHz} \leq f \leq 40\,\mathrm{GHz}$ with a step width of $\Delta f = 0.5\,\mathrm{GHz}$. The microwave power is set to 1 mW and the IF bandwidth of the VNA is 2 Hz. In order to get an appropriate signal to noise ratio, the field sweeps are repeated several times and then averaged before fitting the data.

The working principle of this method explained for the spin Hall effect is as follows: The driven magnetization dynamics in the ferromagnet induce a spin current into the normal metal due to spin pumping [53]. This spin current is then converted by the inverse spin Hall effect into a charge current. The charge current produces an Oersted field which is inductively detected by the CPW, which detects all sources of AC magnetic flux in a S_{21} parameter measurement. As proposed by Berger *et al.* [41], we have to distinguish between four sources of AC magnetic flux. The first contribution is coming from the precessing magnetization in the ferromagnet (CoFeB). The second source of AC magnetic flux is coming from the currents in the normal metal, which are induced by the Faraday-effect due to the precessing magnetization in the ferromagnet. Finally the third and the fourth source are due to field-like inverse spin-orbit torques (e.g. Rashba-Edelstein effect) and the damping-like iSOT (e.g. spin pumping and inverse spin Hall effect).

The large advantage of this measurement method is that the samples do not have to be structured or patterned in any way. Therefore the samples can afterwards be used for other measurements. Furthermore, the method is phase-sensitive, allowing to distinguish damping-like torques and field-like torques.

In the following section, we discuss the necessary processing steps starting from the raw FMR spectra to finally acquire the complex spin-orbit torque conductivity σ^{SOT}, which represents the strength of the spin-orbit torques. From σ^{SOT} we estimate the spin Hall angle θ_{SH} for the AuPt and TaAu alloys and find excellent agreement with theoretical calculations.

4.2 Spin-Orbit Torques Measurement Results

We measure the complex transmission amplitude S_{21} as a function of the external static magnetic field $\mu_0 H_0$ with fixed frequency f. The complex S_{21} spectra are fitted by Eq. (3.12). The spectra are then divided by S_{21}^0, in order to de-embed the spectra from the background. Therefore we use Eq. (3.2) and acquire

$$\Delta S_{21} = \frac{S_{21} - S_{21}^0}{S_{21}^0} = -i \frac{A e^{i\phi}}{C_0 + C_1 H_0} \frac{\chi_{\mathrm{yy}}(\omega, H_0)}{\mu_0 M_{\mathrm{sat}}}, \tag{4.1}$$

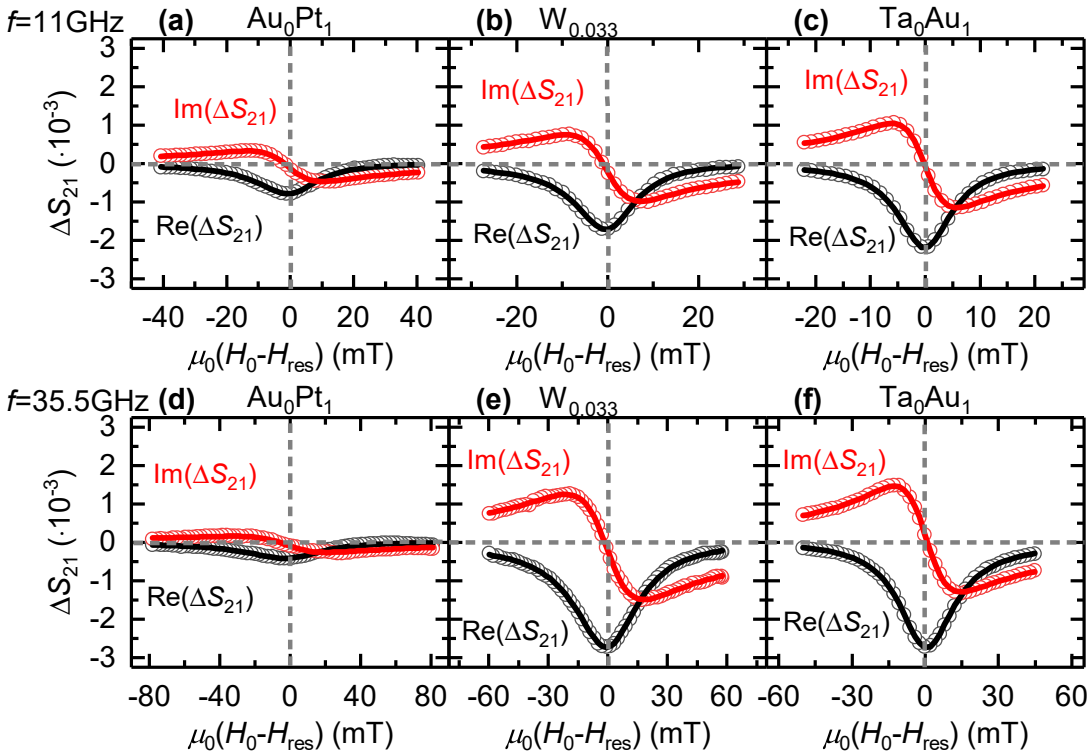

Figure 4.2: Raw data spectrum of the measured complex transmission parameter S_{21} at **(a)**-**(c)** $f = 11\,\mathrm{GHz}$ and **(d)**-**(f)** $f = 35.5\,\mathrm{GHz}$ for three exemplary NM/CoFeB-samples, where the background has already been subtracted according to Eq. (4.1). In solid lines are the fits according to Eq. (3.12). Note that the amplitude of the real and imaginary part of ΔS_{21} at the resonance field $\mu_0 H_{\mathrm{res}}$ are different.

which comprises only the contributions from the sample itself. The variable χ_{yy} is the diagonal entry of the Polder-susceptibility for the given out-of-plane geometry and is described by Eq. (3.10). Exemplary background-corrected data at $f = 11\,\mathrm{GHz}$ and $f = 35.5\,\mathrm{GHz}$ for one composition of each normal metal systems are shown in Fig. 4.2. By comparing the data at the different frequencies, it is obvious that the amplitude at the resonance field $\mu_0 H_{\mathrm{res}}$, indicated by the vertical dashed line, changes. For $\mathrm{Au_0Pt_1}$/CoFeB, the amplitude decreases with increasing frequency (c.f. Fig. 4.2**(a)** and **(d)**) while for $\mathrm{W_{0.033}}$/CoFeB the amplitude increases with frequency (c.f. Fig. 4.2**(b)** and **(e)**).

For all the measured frequencies f we perform two different types of data evaluation. First, we extract the resonance magnetic field $\mu_0 H_{\mathrm{res}}$ and the linewidth $\mu_0 \Delta H$ from the raw spectra (Fig. 4.2) and plot them as a function of the microwave frequency f. The resulting plots are shown in Fig. 4.3, again for the same exemplary normal metals. By fitting the resonance field $\mu_0 H_0$ with the out-of-plane Kittel-equation (Eq. (2.18)), it is possible to extract the effective magnetization, which is given by the y-offset, and the Landè-factor g, which is proportional to the slope. From the linewidth $\mu_0 \Delta H$ it is possible to extract the inhomogeneous linewidth broadening and the Gilbert-damping parameter α_{G} by fitting it with the Landau-Lifshitz-Gilbert equation (Eq. (2.20)). These fits are shown in Fig. 4.3**(a)**

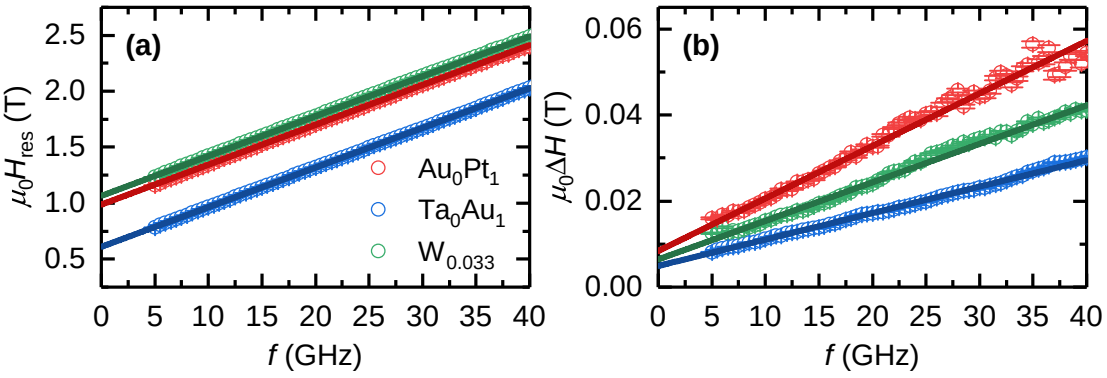

Figure 4.3: Comparison of the acquired FMR data between the different normal metals (TaAu, W and AuPt). FMR results **(a)** from the resonance position $\mu_0 H_{\mathrm{res}}$, where the Landè-factor g and the effective magnetization $\mu_0 M_{\mathrm{eff}}$ is extracted by fitting Eq. (2.18), and **(b)** from the linewidth $\mu_0 \Delta H$, where the Gilbert damping parameter α_{G} and the inhomogeneous linewidth broadening $\mu_0 \Delta H_{\mathrm{inh}}$ is determined by Eq. (2.20).

and **(b)** as solid lines. The extracted Landè-factor g and Gilbert-damping parameter α_{G} are shown later in Figs. 4.6**(a)**,**(b)**, 4.7**(a)**,**(b)** and 4.8**(a)**,**(b)** for TaAu/CoFeB, W/CoFeB and AuPt/CoFeB respectively.

The second type of calculation is taking the amplitude of ΔS_{21} into account. As known from section 3.1, the transmission parameter ΔS_{21} can be described in a voltage divider model with a resistance Z_0 and an inductance L. Under the assumption $Z_0 \gg \omega L$ and after normalizing by $\chi_{\mathrm{yy}}(\omega, H_{\mathrm{res}})$, Eq. (3.5) leads to

$$\frac{\Delta S_{21}}{\chi_{\mathrm{yy}}(\omega, H_{\mathrm{res}})} = \frac{-i\omega \widetilde{L}}{2Z_0}, \tag{4.2}$$

where we introduced the normalized inductance $\widetilde{L} = L/\chi_{\mathrm{yy}}(\omega, H_{\mathrm{res}})$. By plugging Eq. (4.1) into Eq. (4.2) and solving for the normalized inductance $\widetilde{L}$, we get

$$\widetilde{L} = \frac{1}{\mu_0 M_{\mathrm{sat}}} \frac{A e^{i\phi}}{C_0 + C_1 H_0} \frac{Z_0}{\pi f}, \tag{4.3}$$

where we used $\omega = 2\pi f$.

The result is shown in Fig. 4.4**(a)** and **(b)** for the real and imaginary part of $\widetilde{L}$ respectively. By comparing the raw data ΔS_{21} for, e.g., Au_0Pt_1 shown in Fig. 4.2**(a)** and **(d)**, one can reproduce the trend shown in Fig. 4.4**(a)**, that the amplitude decreases with increasing frequency f. For W (Fig. 4.2**(b)**, **(e)**) exactly the opposite is observed, that with increasing frequency f, the amplitude also increases. In Ta_0Au_1 (Fig. 4.2**(c)**, **(f)**) the amplitude remains more or less the same.

As shown in Fig. 4.4**(b)**, the linear trend of the imaginary part of the normalized inductance $\mathrm{Im}(\widetilde{L})$ has a finite offset. This is unphysical as in the DC limit ($f = 0$), we would expect $\mathrm{Im}(\widetilde{L})(f = 0) = 0$. In order to enforce $\mathrm{Im}(\widetilde{L})(f = 0) = 0$, we introduce an

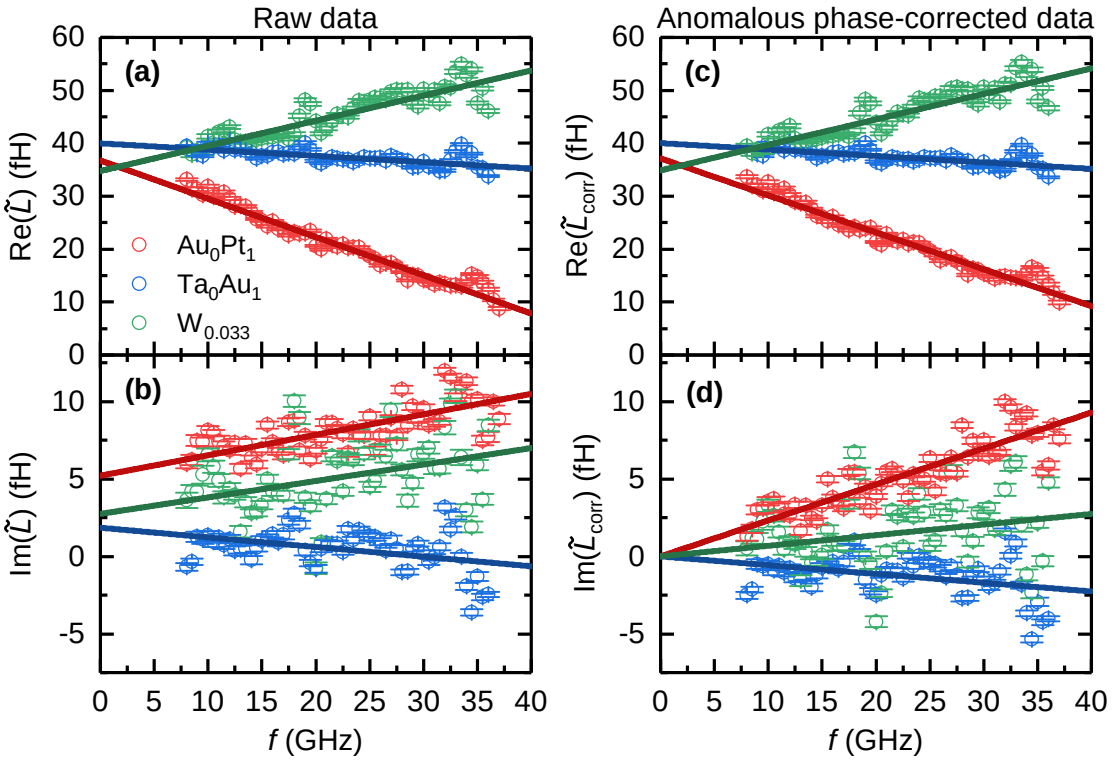

Figure 4.4: Comparison of the acquired inductances between the different normal metals (TaAu, W and AuPt) before (**(a)**,**(b)**) and after the anomalous phase correction (**(c)**,**(d)**). The anomalous phase correction forces the imaginary part of the normalized inductance $\widetilde{L}$ in panel **(d)** to $\mathrm{Im}(\widetilde{L})(f = 0) = 0$. The solid lines represent the fits according to Eqs. (4.5) and (4.6).

anomalous phase ϕ_{corr}, which is defined as $\phi_{\mathrm{corr}} = \arctan\left(\mathrm{Im}(L)(f = 0)/\,\mathrm{Re}(L)(f = 0)\right)$. We therefore effectively perform a rotation of the coordinate system by calculating

$$\begin{aligned} \widetilde{L} &= \mathrm{Re}(\widetilde{L}) + i\,\mathrm{Im}(\widetilde{L}) \\ \begin{pmatrix} \mathrm{Re}(\widetilde{L}_{\mathrm{corr}}) \\ \mathrm{Im}(\widetilde{L}_{\mathrm{corr}}) \end{pmatrix} &= \begin{pmatrix} \cos(\phi_{\mathrm{corr}}) & -\sin(\phi_{\mathrm{corr}}) \\ \sin(\phi_{\mathrm{corr}}) & \cos(\phi_{\mathrm{corr}}) \end{pmatrix} \begin{pmatrix} \mathrm{Re}(\widetilde{L}) \\ \mathrm{Im}(\widetilde{L}) \end{pmatrix}. \end{aligned} \tag{4.4}$$

This anomalous phase is most likely due to the small (but finite) capacitive coupling between the CPW and the sample. The result of the anomalous phase correction is shown in Fig. 4.4**(c)** and **(d)**. The behaviour of these curves can then be described by

$$\mathrm{Re}(\widetilde{L}_{\mathrm{corr}}) = \widetilde{L}_0 + \mathrm{Re}(\widetilde{L}_{\mathrm{NM}}) \cdot f \tag{4.5}$$

$$\mathrm{Im}(\widetilde{L}_{\mathrm{corr}}) = \mathrm{Im}(\widetilde{L}_{\mathrm{NM}}) \cdot f, \tag{4.6}$$

where the real part $\mathrm{Re}(\widetilde{L}_{\mathrm{corr}})$ is split into a frequency-independent $\mathrm{Re}(\widetilde{L}_0)$ and into a

frequency-dependent part $\mathrm{Re}(\widetilde{L}_{\mathrm{NM}})$ and the imaginary part $\mathrm{Im}(\widetilde{L}_{\mathrm{corr}})$ is solely described by a frequency-dependent contribution $\mathrm{Im}(\widetilde{L}_{\mathrm{NM}})$.

The offset of $\mathrm{Re}(\widetilde{L}_{\mathrm{corr}})$ is known and has already been discussed in section 3.1. This term is the normalized dipolar inductance $\widetilde{L}_0$ of the precessing magnetization of the ferromagnet and can be quantified by Eq. (3.7), where also the finite spacing δ_{sl} between the sample and the CPW is taken into account (also shown in Fig. 4.1). The slope of the real and imaginary part of the inductance $\widetilde{L}_{\mathrm{corr}}$ is coming from the currents in the normal metal and is therefore denoted as $\widetilde{L}_{\mathrm{NM}}$. It is obvious that $\widetilde{L}_{\mathrm{NM}}$ scales linearly with frequency f, as the currents in the normal metal are driven by the oscillating part of the magnetization $\partial\mathbf{m}(t)/\partial t$ [41]. The dipolar inductance L_0 in contrast is frequency-independent.

By extracting the values for the real and imaginary part of the normalized inductance $\widetilde{L}_{\mathrm{corr}}$ by fitting the acquired data with Eqs. (4.5) and (4.6) for all the measured samples, we obtain the data shown in Fig. 4.5. From Fig. 4.5 we observe two features: The first is the difference in the magnitudes of the inductances especially for $\widetilde{L}_{\mathrm{NM}}$, where the TaAu/CoFeB shows the lowest magnitude compared to the other two normal metals. The second feature is the sign change of the inductance $\widetilde{L}_{\mathrm{NM}}$, not only across the normal metals but also within a certain normal metal (e.g. $\mathrm{Im}(\widetilde{L}_{\mathrm{NM}})$ for AuPt/CoFeB). For our further discussions $\mathrm{Re}(\widetilde{L}_0)$ will not be taken into account any more, as it only is a measure of how well the sample was coupled to the CPW. The spacing δ_{sl} between the sample and the CPW is calculated from the measured $\mathrm{Re}(\widetilde{L}_0)$ by using the Eqs. (3.7) and (3.8).

In the next section we want to quantify the inverse spin-orbit torques by giving an analytical expression for L_{NM} and consequently calculate the complex conductivity σ^{SOT}, which is a direct measure for the strength of the effects.

4.2.1 Conductivities of the Inverse Spin-Orbit Torques

As already discussed in the previous section, L_{NM} describes the inductance due to the AC currents in the normal metal. This quantity can be calculated by [41]

$$L_{\mathrm{NM}} = -L_{21}\,\eta(\delta_{\mathrm{sl}},w_{\mathrm{cc}})\,\frac{\hbar\omega}{4M_{\mathrm{sat}}e}\,\chi_{\mathrm{yy}}(\omega,H_0)\,\sigma^{\mathrm{SOT}}, \tag{4.7}$$

where e is the electron charge, $\eta(\delta_{\mathrm{sl}},w_{\mathrm{cc}})$ is an attenuation factor described by Eq. (3.8), which accounts for the finite spacing δ_{sl} between the sample and the CPW, and L_{21} is the mutual inductance between the CPW and the sample. The minus in Eq. (4.7) is due to the used stacking order of substrate/normal metal/ferromagnet. In the case of substrate/ferromagnet/normal metal the minus becomes a plus because when reversing the stacking order the sign of the spin-orbit torques and the Faraday currents also changes [41]. The mutual inductance L_{21} can be modelled as two current-carrying sheets with a finite spacing δ_{sl}, which results in [54]

$$L_{21} = \frac{\mu_0}{4\pi}\,2l\left(\ln\left(\frac{2l}{R}\right)-1\right) \tag{4.8}$$

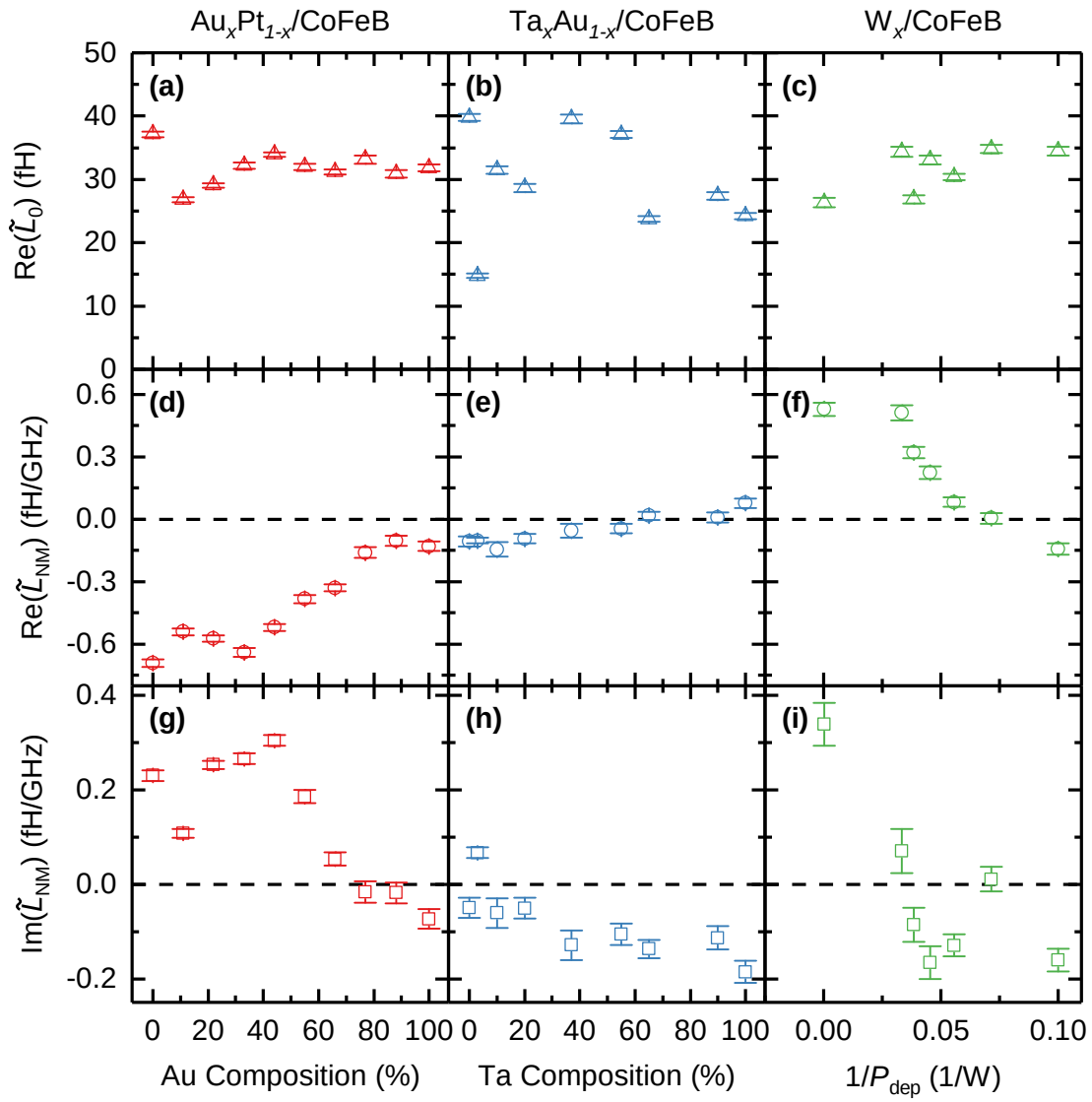

Figure 4.5: Overview of the measured inductances L of the three different normal metal systems as a function of the specific composition. Each column corresponds to a normal metal (**(a)**,**(d)**,**(g)** AuPt, **(b)**,**(e)**,**(h)** TaAu and **(c)**,**(f)**,**(i)** W) and each row shows the inductance (**(a)**,**(b)**,**(c)** Re($\widetilde{L}_0$), **(d)**,**(e)**,**(f)** Re($\widetilde{L}_{\mathrm{NM}}$) and **(g)**,**(h)**,**(i)** Im($\widetilde{L}_{\mathrm{NM}}$)).

with

$$R \equiv \sqrt{w_{\mathrm{cc}}^2 + \delta_{\mathrm{sl}}^2} \left(\frac{\delta_{\mathrm{sl}}}{\sqrt{w_{\mathrm{cc}}^2 + \delta_{\mathrm{sl}}^2}} \right)^{\left(\frac{\delta_{\mathrm{sl}}}{w_{\mathrm{cc}}}\right)^2} \exp\left(\frac{2\delta_{\mathrm{sl}}}{w_{\mathrm{cc}}} \arctan\left(\frac{w_{\mathrm{cc}}}{\delta_{\mathrm{sl}}} \right) - \frac{3}{2} \right). \tag{4.9}$$

The variable σ^{SOT} in Eq. (4.7) is an effective conductivity, which relates the charge current density $\mathbf{J}$ flowing in the NM-layer with the driving force $\partial \mathbf{m}(t)/\partial t$. This can be seen as an analogy to the Ohm's law $\mathbf{J} = \sigma \mathbf{E}$, which relates the charge current density with an electrical field [41]. This conductivity is a complex quantity, which comprises

the inverse spin-orbit torques and can be written as the sum of the conductivities of the iSOT $\sigma^{\mathrm{SOT}} = \sigma_{\mathrm{o}}^{\mathrm{SOT}} + i(\sigma_{\mathrm{e}}^{\mathrm{SOT}} - \sigma_{\mathrm{e}}^{\mathrm{F}})$, where "o" and "e" denote the already mentioned odd and even symmetry of the SOT with respect to time-reversal. The odd iSOT $\sigma_{\mathrm{o}}^{\mathrm{SOT}}$ corresponds to the inverse spin Hall effect and to spin currents due to spin pumping and is 90° phase-shifted to the even iSOT $(\sigma_{\mathrm{e}}^{\mathrm{SOT}} - \sigma_{\mathrm{e}}^{\mathrm{F}})$, which is related to the Rashba-Edelstein and the Faraday effect.

The spin-orbit torques due to spin pumping can be described with the concept of the spin-mixing conductance $G_{\uparrow\downarrow}$, which allows the description of spin transport between FM/NM interfaces [55]. As already discussed, the precessing magnetization in the ferromagnet induces a current in the normal metal. As proposed by Tserkovnyak *et al.* [13], this spin current density $\mathbf{J}_{\mathrm{s}}$ due to spin pumping can be described by [13, 52]

$$\mathbf{J}_{\mathrm{s}} = \frac{\hbar}{4\pi}\left(\mathrm{Re}(G_{\uparrow\downarrow})\,\mathbf{m}\times\frac{\mathrm{d}\mathbf{m}}{\mathrm{d}t} - \mathrm{Im}(G_{\uparrow\downarrow})\,\frac{\mathrm{d}\mathbf{m}}{\mathrm{d}t}\right), \tag{4.10}$$

where $\mathbf{m}$ is defined as $\mathbf{m} = \mathbf{M}/M_{\mathrm{sat}}$. In Eq. (4.10), the first term describes a damping-like and the second term a field-like torque. The real part of the spin-mixing conductance $\mathrm{Re}(G_{\uparrow\downarrow})$ is related to the Gilbert-damping constant α_{G} and the imaginary part to the Landè-factor g [13]. In the experiment, if $\sigma_{\mathrm{o}}^{\mathrm{SOT}}$ increases with increasing Gilbert damping parameter α_{G}, this indicates that the spin pumping mechanism is responsible for the spin-orbit torque. The Gilbert damping α_{G} increases because the spin current responsible for the spin-orbit torque first has to get into the normal metal.

The extracted inductances $\widetilde{L}_{\mathrm{NM}}$ are plugged into Eq. (4.7) and the conductivities σ^{SOT} are calculated for the real and imaginary part respectively. The results are shown in Figs. 4.6**(c)**,**(d)**, 4.7**(c)**,**(d)** and 4.8**(c)**,**(d)** for each normal metal respectively.

Now the different normal metals should be discussed in a little more detail, starting with the TaAu/CoFeB samples, which are shown in Fig. 4.6. The FMR parameters g and α_{G} (panel **(a)** and **(b)**) do not show any correlation. Also the even iSOT conductivities $(\sigma_{\mathrm{e}}^{\mathrm{SOT}} - \sigma_{\mathrm{e}}^{\mathrm{F}})$ (panel **(c)**) only increase a little with more tantalum content in the normal metal. The sample $\mathrm{Ta_5Au_{95}}$ is most likely an outlier as a sign change for only one sample in the series would be unreasonable. The odd iSOT conductivity $\sigma_{\mathrm{o}}^{\mathrm{SOT}}$ (panel **(d)**) reaches its maximum for $\mathrm{Ta_{20}Au_{80}}$ and also features a sign change at a tantalum content of about 57%. This sign change is reasonable by looking at the sign of the spin Hall angle for the normal metals (e.g. [56] Fig. 7). For gold we would expect a positive spin Hall angle in contrast to tantalum, which should have a negative one. This is in accordance with our measurement, because the spin Hall angle is directly proportional to the conductivity $\sigma_{\mathrm{o}}^{\mathrm{SOT}}$. As also already seen from Fig. 4.5 the size of the iSOT effects is, in contrast to the other normal metals, small and almost at the detection limit of the measurement technique.

Continuing with the W/CoFeB samples shown in Fig. 4.7, we observe a correlation between the g-factor (panel **(a)**) and the even inverse spin-orbit torques $(\sigma_{\mathrm{e}}^{\mathrm{SOT}} - \sigma_{\mathrm{e}}^{\mathrm{F}})$ (panel **(c)**). This behaviour might be related to the imaginary part of the spin-mixing conductance $\mathrm{Im}(G_{\uparrow\downarrow})$, which is theoretically predicted to cause a field-like torque [13]. Also the odd inverse spin-orbit torque $\sigma_{\mathrm{o}}^{\mathrm{SOT}}$ (panel **(d)**) shows a correlation with the Gilbert-damping

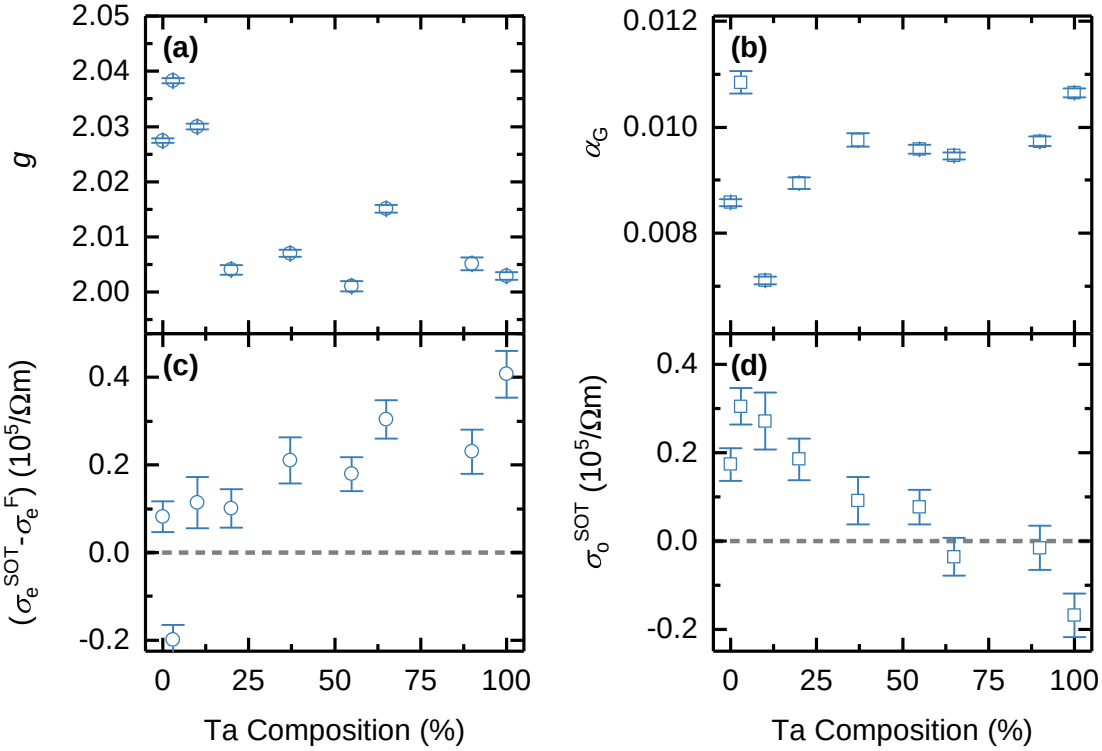

Figure 4.6: FMR extracted parameters (g-factor **(a)** and α_G **(b)**) and the calculated iSOT conductivities ($(\sigma_e^{SOT}-\sigma_e^F)$ **(c)** and σ_o^{SOT} **(d)**) for TaAu/CoFeB as a function of the tantalum composition. The plots are aligned the way, that they eventually show the correlation between the iSOT conductivity and the corresponding FMR parameter.

α_G. The sign of the iSOT conductivity σ_o^{SOT} matches the expected negative sign of the spin Hall angle of wolfram. However, we observe a sign change for W(O)x with the most oxygen ($P_{dep}^{-1} = 0.10$), which so far has not been predicted by theory.

The last sample series is AuPt/CoFeB shown in Fig. 4.8. In this normal metal system we observe a correlation between σ_o^{SOT} and the Gilbert damping α_G. The Gilbert damping decreases with an increasing gold concentration. In the range between $0\% - 35\%$ Au composition we find a plateau in the spin-orbit torque conductivity σ_o^{SOT} but the damping constant α_G decreases. This indicates, that for pure platinum the spin current is more contributing to σ_o^{SOT} than for e.g. $Au_{33}Pt_{67}$. With increasing gold contribution the spin current decreases (as α_G decreases). However, the plateau in σ^{SOT} can be explained if we assume that the spin Hall angle increases. In section 4.3, we calculate the spin Hall angle θ_{SH} and indeed find that it initially increases with increasing Au content in $Au_xPt_{(}1-x)$/CoFeB. Furthermore we do not observe a sign change in the odd iSOT conductivity σ_o^{SOT} as both gold and platinum have a positive spin Hall angle.

In the next section we derive the spin Hall angle θ_{SH} from the conductivity of the inverse odd spin-orbit torque σ_o^{SOT}. The calculated spin Hall angles θ_{SH} are shown in section 4.3, where they are compared to the outcome of the two collaborating groups with their measurement techniques, which should be treated briefly.

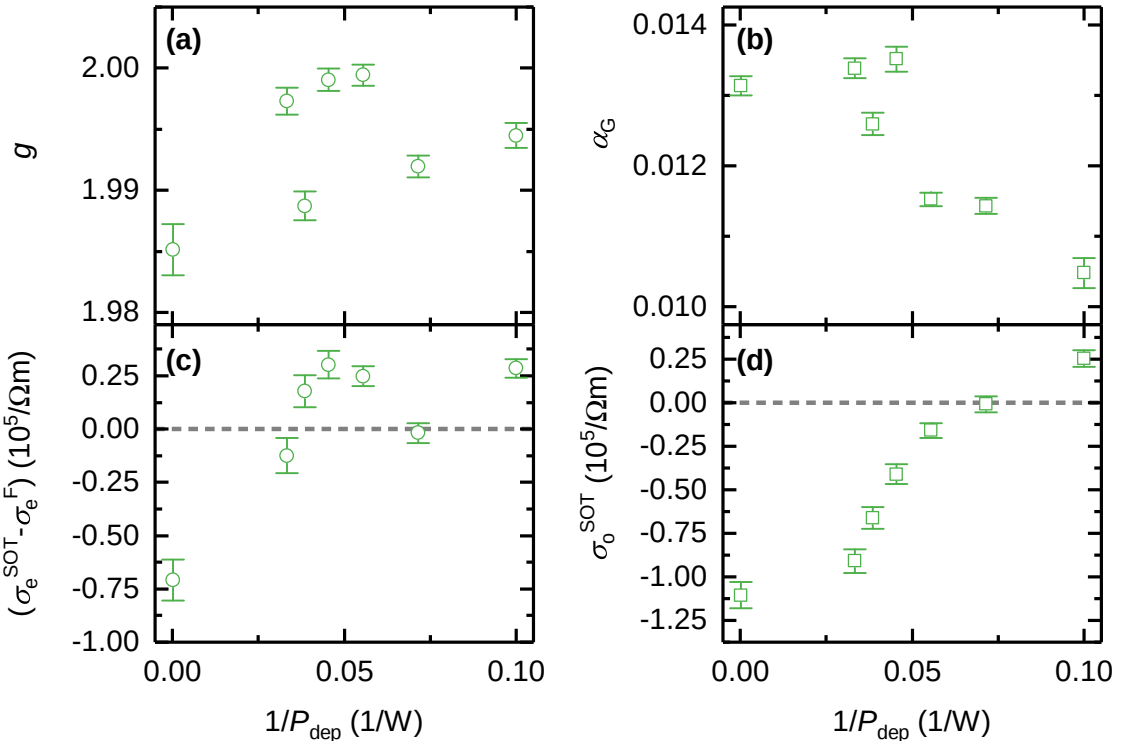

Figure 4.7: FMR extracted parameters (g-factor **(a)** and α_G **(b)**) and the calculated iSOT conductivities (($\sigma_e^{SOT} - \sigma_e^F$) **(c)** and σ_o^{SOT} **(d)**) for W/CoFeB as a function of the inverse sputtering power. The plots are aligned the way, that they eventually show the correlation between the iSOT conductivity and the corresponding FMR parameter.

4.2.2 Spin Hall Angle

The odd iSOT conductivity σ_o^{SOT} is related to the inverse spin Hall effect. It is known from theory that the Gilbert damping α_G is related to σ_o^{SOT}. In order to calculate the spin Hall angle θ_{SH}, a voltage divider model for the spin accumulation at the FM/NM interface due to spin pumping is assumed, because the interfacial spin-mixing conductance $1/G_{\uparrow\downarrow}$ and the spin conductance of the normal metal $1/G_{ext}$ are assumed to be in series [41]. The spin-mixing conductance describes the spin transport between interfaces [55]. It is important to note, that the spin-mixing conductance $G_{\uparrow\downarrow}$ is a complex quantity in contrast to the spin conductances $G_\uparrow$ and $G_\downarrow$, which are real quantities.

Without a derivation, we get for the conductivity [41]

$$\sigma_o^{SOT} = \theta_{SH}\,\sigma_{NM}\,\mathrm{Re}\left(\frac{G_{\uparrow\downarrow}}{\frac{\sigma_{NM}}{2\lambda_s}\tanh\left(\frac{d_{NM}}{\lambda_s}\right) + G_{\uparrow\downarrow}}\right)(1-\delta), \tag{4.11}$$

where σ_{NM} is the conductivity, λ_s is the spin diffusion length of the normal metal and δ is the interfacial spin memory loss due to unavoidable spin relaxation [57]. From this equation it is evident, that the term $\theta_{SH}\sigma_{NM}$ is related to the spin Hall effect and the rest of Eq. (4.11) to the spin current due to spin pumping. In a perfectly transparent

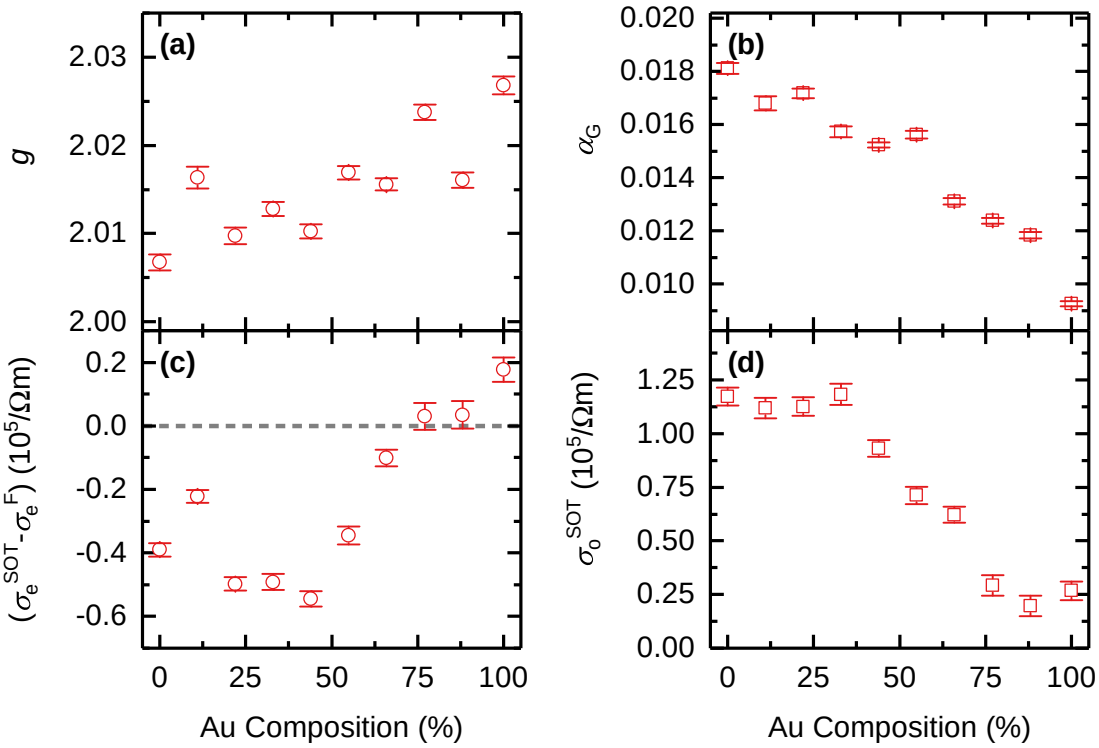

Figure 4.8: FMR extracted parameters (g-factor **(a)** and α_G **(b)**) and the calculated iSOT conductivities (($\sigma_e^{SOT} - \sigma_e^F$) **(c)** and σ_o^{SOT} **(d)**) for AuPt/CoFeB as a function of the gold composition. The plots are aligned the way, that they eventually show the correlation between the iSOT conductivity and the corresponding FMR parameter.

interface, only the spin Hall effect contributes to the spin-orbit torque. It is now necessary to calculate the spin-mixing conductance, which is given by [58]

$$G_{\text{eff}} = \frac{G_{\uparrow\downarrow}}{1 + \frac{G_{\uparrow\downarrow}}{G_{\text{ext}}}}, \tag{4.12}$$

with the external conductance

$$G_{\text{ext}} = \frac{\sigma_{\text{NM}}}{2\lambda_{\text{s}}} \tanh\left(\frac{d_{\text{NM}}}{\lambda_{\text{s}}}\right). \tag{4.13}$$

The real part of the spin-mixing conductance $G_{\uparrow\downarrow}$ can now be computed by solving

$$\alpha_{\text{G}} - \alpha_0 = \frac{\gamma\,\hbar^2}{2e^2 M_{\text{sat}}\, d_{\text{FM}}}\ \text{Re}(G_{\text{eff}}) \tag{4.14}$$

and by plugging in Eqs. (4.12) and (4.13). In this relation, α_0 is the intrinsic Gilbert damping of the ferromagnet (CoFeB) only and is taken from literature using a value $\alpha_0 = 4.2{\cdot}10^{-3}$ [59]. It is therefore evident from Eq. (4.14), that the spin-mixing conductance is proportional to the Gilbert damping α_G. As seen from Eq. (4.11), the calculation of the spin Hall angle θ_{SH} requires the conductivity of the normal metal σ_{NM}. We use σ_{NM}

measured at the University of Bielefeld (group of M. Meinert) on reference samples grown on MgO. The spin diffusion length λ_s is directly proportional to the conductivity σ_{NM}. To calculate the spin diffusion lengths λ_s, we assume $Ta_{0.1}Au_{0.9}$ to have $\lambda_s = 2.0\,nm$ and pure platinum to have $\lambda_s = 1.3\,nm$. From the measured conductivities σ_{NM}, λ_s is then calculated for all samples. The resulting spin Hall angles θ_{SH} are shown in Fig. 4.9.

In the next section, the calculated spin Hall angle θ_{SH} are discussed and compared with the data of the two other collaborating groups and with theoretical calculations.

4.3 Comparison with THz-, Harmonic Hall-Measurement and Theory

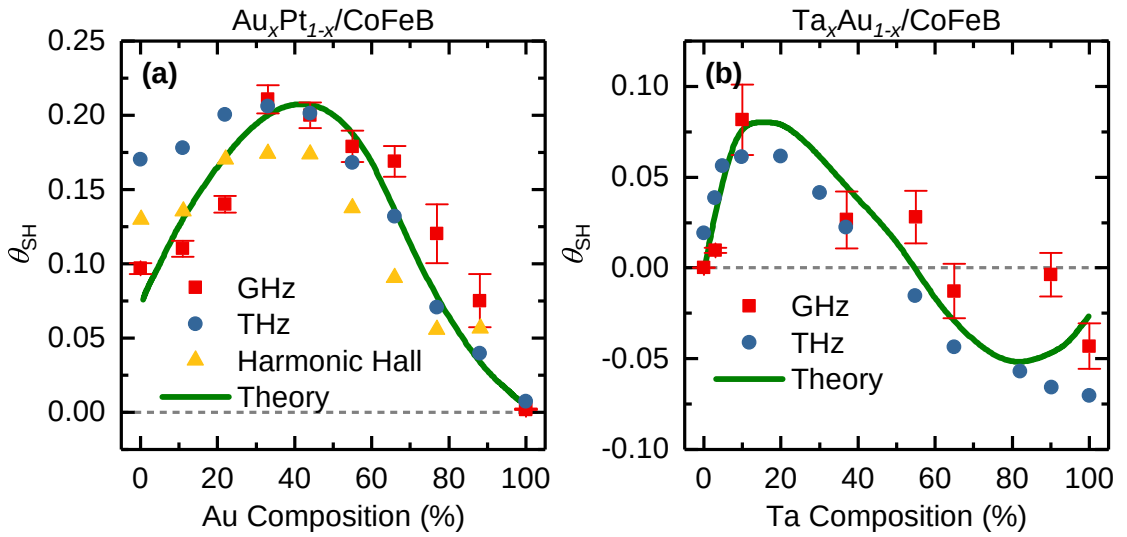

Figure 4.9: Comparison of the calculated spin Hall angle θ_{SH} with three different measurement techniques (GHz, THz and harmonic Hall) and theory for **(a)** AuPt/CoFeB and **(b)** TaAu/CoFeB.

The idea of this collaboration was to measure the spin-orbit torques with different measurement techniques, which cover a broad frequency spectrum. The lowest frequencies are found in the harmonic Hall measurement conducted by the group of Markus Meinert, which uses frequencies of a few kilohertz. Our method operates in the gigahertz regime and finally terahertz (THz) emission experiments were conducted by Oliver Gückstock and Tom Seifert from the group of Tobias Kampfrath. In the following paragraph these two other techniques will be briefly explained.

The harmonic Hall measurement technique requires to pattern a Hall-bar structure onto the normal metal. An alternating current with a frequency of 3.219 kHz is applied along the Hall bar. The magnetic field is applied in-plane and swept from $-1.6\,T$ to $1.6\,T$. A Lock-In amplifier is used to measure the Hall-voltage, where the in-phase first harmonic and the out-of-phase second harmonic signals give the full information about the odd spin-orbit torque [60, 61].

The terahertz emission experiment uses an incident femtosecond laser pulse at the ferromagnet, which excites the electrons. Consequently a spin current, due to the different transport properties of the ferromagnet and the normal metal, along the FM/NM stack is occurring. When the spin current enters the normal metal it is converted into an ultrafast transverse charge current due to the inverse spin Hall effect. This current radiates then an electromagnetic wave in the terahertz regime, which is then finally detected [62].

It is important to note that the THz emission experiment is only able to provide a relative measure of the spin Hall angle. This means that the measured THz amplitudes of the samples, which are proportional to the spin Hall angle, are normalized to a certain sample amplitude (e.g. pure gold). A scaling factor is hence used for the THz measurements, in order to best describe the theoretical calculations. Our measurement method and the harmonic Hall measurement technique are in contrast quantitative.

In Fig. 4.9 the gained results of the three measurement techniques are shown for **(a)** AuPt/CoFeB and **(b)** TaAu/CoFeB. Starting with AuPt/CoFeB we remarkably observe a maximum in the curve in the range of $30\% - 40\%$ gold content. The spin Hall angle θ_{SH} is here two times larger than that of pure platinum. For our calculations of the spin Hall angle, we assumed a interfacial spin loss of $\delta = 0.5$ [57]. By comparing Figs. 4.8**(d)** and 4.9**(a)** we can qualitatively distinguish the spin pumping and the spin Hall effect contribution. As already shown in section 4.2.1, at pure platinum the spin-orbit torque conductivity is larger than at 30% gold concentration. This means that pure Pt is more efficient in converting an applied charge current to a spin-orbit torque than $Au_{0.3}Pt_{0.7}$. The increase of the spin Hall angle seen in Fig. 4.9**(a)** hence is accompanied by a reduction of the effective spin-mixing conductance. The theoretical data (green curve) is taken from Obstbaum *et al.* [63]. The results of the three measurement techniques are in very good agreement with theory and with each other. Although at low gold compositions the THz-data (blue points) differs from the harmonic Hall and our GHz measurements.

For TaAu/CoFeB, shown in Fig. 4.9**(b)**, we assumed for our calculation of the spin Hall angle θ_{SH} an interfacial spin loss of $\delta = 0.6$. The theory data is provided by Sebastian Wimmer from the group of Hubert Ebert (LMU Munich). Again we find a good agreement of our GHz measurement data with the THz results and the theoretical calculation. The expected sign change of the spin Hall angle from gold (positive) to tantalum (negative) is observed.

For the W/CoFeB samples we have data for the conductivities σ_{NM}. Nevertheless, we do not have information about the spin diffusion length λ_{s} in this system and additionally the dependence of the spin diffusion length λ_{s} on the conductivity σ_{NM} of oxidized wolfram is not known. Therefore we cannot extract the spin Hall angle θ_{SH} for the W/CoFeB series.

4.4 Summary

In this chapter, we have investigated normal metal/ferromagnet bilayers with different normal metal compounds using a phase-sensitive vector network analyzer ferromagnetic resonance technique in the frequency range of $5\,\mathrm{GHz} \leq f \leq 40\,\mathrm{GHz}$. By placing the samples flip-chip style onto the coplanar waveguide, the inverse spin-orbit torques have been quantified. The idea of this technique is, that the sample is inductively coupled to the coplanar waveguide, which detects the additional flux produced by the current caused by the inverse spin-orbit torques.

Due to our phase-sensitive measurement, we were able to distinguish between the damping-like and the field-like spin-orbit torques as they are 90° phase-shifted to each other. The damping-like torque was attributed to the inverse spin Hall effect and the spin currents due to spin pumping. We were also able to calculate the spin Hall angle, which is a measure for the conversion efficiency of a charge current to a spin current. The field-like torques are related to the Faraday-effect in the normal metal and to the Rashba-Edelstein effect. In order to quantify the effects of the inverse spin-orbit torques, we calculated the iSOT conductivities σ^{SOT}.

We have probed three different normal metal/ferromagnet sample series, namely: TaAu/CoFeB, W/CoFeB and AuPt/CoFeB. The TaAu/CoFeB did not show any remarkable features in the conductivities. As expected this sample series showed the smallest spin Hall effect and also the sign change from a negative spin Hall angle for pure tantalum to a positive one for pure gold could be reproduced. For these samples we could not observe any correlation between the FMR parameters and the iSOT conductivities.

The W/CoFeB showed a remarkably correlation between the FMR parameters (g and α_{G}) and the iSOT conductivities ($(\sigma_{\mathrm{e}}^{\mathrm{SOT}} - \sigma_{\mathrm{e}}^{\mathrm{F}})$ and $\sigma_{\mathrm{o}}^{\mathrm{SOT}}$). Although the matching is not perfect, the corresponding parameters show an uncanny likeness (cf. Fig. 4.7). For the inverse spin Hall effect we also observe the expected negative sign of the spin Hall angle for wolfram. It is interesting that the sign of the spin Hall angle changes with decreasing sputtering power (P_{dep}^{-1} increasing) or with increasing oxygen content for W(O)x. The reason for this behaviour is unknown.

The AuPt/CoFeB samples shows a maximum in the spin Hall angle θ_{SH}. The sample $\mathrm{Au}_{0.33}\mathrm{Pt}_{0.67}$/CoFeB has a two times larger spin Hall angle than the pure platinum sample $\mathrm{Au}_0\mathrm{Pt}_1$/CoFeB. This is interesting, as platinum is known as a normal metal with one of the largest spin Hall angles [56].

Due to the collaboration with Markus Meinert and the group of Tobias Kampfrath, it was possible to compare our results with two different measurement techniques namely the harmonic Hall measurement and the terahertz emission experiment. These techniques are sensitive to the damping-like spin-orbit torques and it was possible to compare the spin Hall angle θ_{SH} with each other and with theory. The results throughout the three techniques are in very good agreement with each other and also with theory. This shows that the damping-like spin-orbit torques do not depend on frequency from dc to THz and can be accurately determined using different measurement techniques.

Chapter 5

(Strongly) Coupled Magnetization Dynamics in the Compensated Ferrimagnet Gadolinium Iron Garnet

In the previous chapter we discussed the magnetization dynamics in a magnetic bilayer thin film. We now consider a single crystalline ferrimagnet. Ferrimagnetism is a magnetic ordering phenomena like ferro- and antiferromagnetism. In a ferromanget the spins are aligned in parallel and in an antiferromanget they are antiparallel due to the Heisenberg exchange interaction [17]. In the antiferromagnet the magnetization is zero. The ferrimanget may now be defined as an antiferromagnet with unbalanced magnetic sublattices so the total magnetization is different from zero. This can occur, for example if either the population of similar spins (up or down) are unbalanced or the total magnetic moments of different sublattices are unequal, which requires some sort of crystallographic selection [64].

The so-called (rare-earth) iron garnets, which have a cubic lattice, are a prototype ferrimagnetic system. Their lattice consists of three sublattices, which are an octahedrally coordinated Fe-ions sublattice (a-sublattice), a tetrahedral Fe-sublattice (d-sublattice) and a dodecahedral rare-earth metal or yttrium lattice (c-sublattice), which leads to the occurrence of ferrimagnetism [65]. The most famous representative of the material class is yttrium iron garnet ($Y_3Fe_5O_{12}$) or short YIG, which is already used in numerous applications like in microwave technology [66].

In this chapter we focus on the fully gadolinium (Gd) substitute gadolinium iron garnet ($Gd_3Fe_5O_{12}$) or short GdIG. The main difference between YIG and GdIG is, that gadolinium has an unfilled $4f$ shell in contrast to yttrium, which has an unfilled $4d$ shell. This leads to completely different magnetic properties [64].

The three sublattices of the rare-earth iron garnets contribute to the total magnetization and add up to the total magnetization

$$M_{\mathrm{tot}} = M_{\mathrm{c}} + M_{\mathrm{Fe,a}} - M_{\mathrm{Fe,d}} = M_{\mathrm{Gd}} + M_{\mathrm{Fe,coupled}}. \tag{5.1}$$

The two iron-sublattices (a- and d-sublattice) are strongly antiferromagnetically coupled and can be treated as one effective sublattice $M_{\mathrm{Fe,coupled}} = M_{\mathrm{Fe,a}} - M_{\mathrm{Fe,d}}$. Therefore the effective number of sublattices is reduced from three to two. This simplification will be needed later in section 5.2.2 because performing calculations with three sublattices is tedious. The gadolinium-sublattice is again weakly antiferromagnetically coupled to

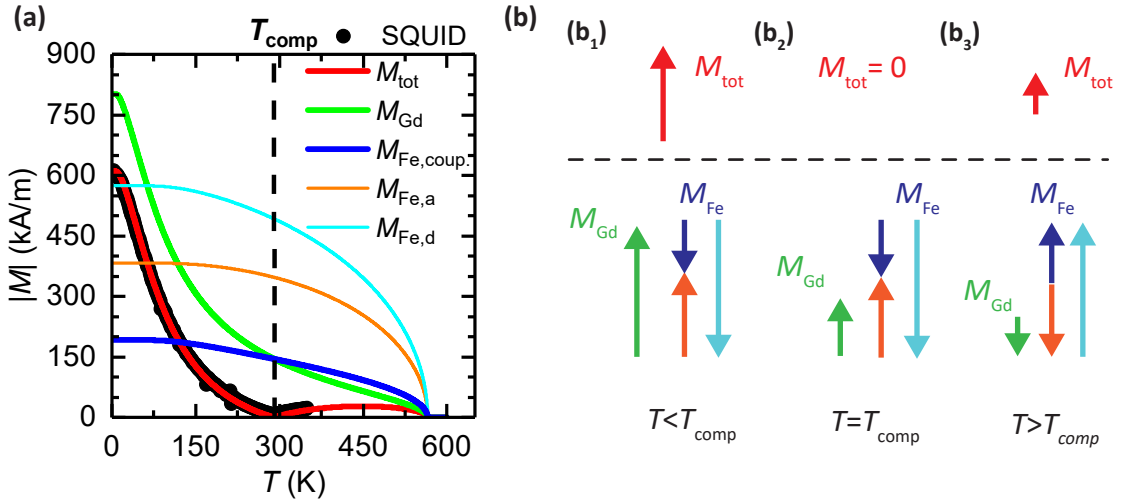

Figure 5.1: **(a)** Simulation of the magnetization of the sublattices according to [67]. In black a SQUID measurement with a magnetic field $\mu_0 H_0 = 1\,\mathrm{T}$ is shown to compare the simulated data with a measurement. **(b)** Schematic evolution of the magnetization of the gadolinium iron garnet sublattices for certain temperatures for a finite external applied magnetic field ($\mu_0 H_0 \neq 0$). **($\mathbf{b}_1$)** At temperatures lower than the compensation temperature $T_{\mathrm{comp}} > T$ the magnetization of the Gd-sublattice dominates. **($\mathbf{b}_2$)** At the compensation point $T = T_{\mathrm{comp}}$ the net remanent magnetization vanishes as the magnetization of the Gd- and the Fe-sublattice are equal. **($\mathbf{b}_3$)** For temperatures larger than the compensation temperature $T_{\mathrm{comp}} < T$ the magnetization of the Fe-sublattices dominates. Note that the magnetization of the Fe-sublattices barely changes with temperature in contrast to the Gd-sublattice.

the iron-sublattice, which leads to the emergence of a so-called compensation point at the compensation temperature T_{comp}, where the magnetic moment of the Gd-sublattice equals the moment of the coupled iron-lattice $M_{\mathrm{Gd}} = M_{\mathrm{Fe,coupled}}$. This is in complete contrast to YIG, which does not feature such a compensation point due to the fact, that the magnetization of the c-sublattice (here Y-sublattice) is zero and therefore only the magnetization of the coupled iron-sublattice is relevant.

The calculation of the sublattice magnetization can be done by using molecular field theory [67, 68]. The sublattices are only exchange coupled, which then leads for the three sublattices to

$$M_i(T) = M_i(0) \cdot B_{S_i}(a_i) \quad i \in \{a,d,c\}\,, \tag{5.2}$$

where $M_i(0)$ is the magnetization at $T = 0\,\mathrm{K}$ and $B_{S_i}(a_i)$ is the Brillouin function with the Boltzmann energy ratios $a_i = m_i \mu_0 H_{\mathrm{ex}}^{(i)} / k_{\mathrm{B}} T$, where the coupling between the sublattices is taken into account. The molecular field coefficients are taken from [67] and slightly adjusted to yield the compensation temperature $T_{\mathrm{comp}} = 288\,\mathrm{K}$ found in the SQUID-measurement performed by Stephan Geprägs. By solving these equations self-consistently, the magnetization of the sublattices and the total magnetization can be calculated, which is shown in Fig. 5.1**(a)**. To compare the calculated values, the data of a

SQUID-measurement at an external magnetic field of $\mu_0 H_0 = 1\,\mathrm{T}$ is shown. At an applied external field H_0 the total magnetization always points along the magnetic field as also shown in Fig. 5.1**(b)**. The Fe-sublattice only shows a very weak temperature dependence and directly corresponds to the total YIG magnetization (blue curve). At the compensation point T_{comp} the magnetization of the Gd- and Fe-sublattice cancel each other out and the total magnetization is zero, as schematically shown in Fig. 5.1**($\mathbf{b}_2$)**.

The tune-ability of the magnetization makes gadolinium iron garnet an ideal testbed to investigate the magnetization dynamics close to and far away of the compensation point. In this experiment we investigate the magnetization dynamics in a single crystalline bulk GdIG-disk using a cryogenic-temperature VNA-FMR setup. In section 5.1 the sample under investigation and the used experimental setup are discussed. The magnetic modes of the ferrimagnet, namely the ferrimagnetic and antiferromagnetic resonance, and their theoretical description are briefly discussed in section 5.2. Afterwards the transition between weak and strong coupling of the ferrimagnetic and antiferromagnetic mode depending on the orientation of the external magnetic field relative to the crystallographic directions, is investigated in section 5.3.

5.1 Experimental Setup

In this experiment, we investigate a single crystalline bulk GdIG-disk, which was grown by Andreas Erb using travelling solvent floating zone [69]. The magnetic alignment of the ferrimagnet was done by Stephan Geprägs. The disk has a diameter of $d = 6.35\,\mathrm{mm}$ and a thickness of $t = 500\,\mu\mathrm{m}$.

For our investigation of the magnetization dynamics in the ferrimagnet, a cryogenic-temperature broadband vector network analyzer ferromagnetic measurement setup is used. The GdIG-disk is placed on a coplanar waveguide with a center conductor width of $w_{\mathrm{cc}} = 250\,\mu\mathrm{m}$. The CPW is mounted on a dipstick, which is placed in the variable temperature inset (VTI) of the cryostat. The sample temperature is adjusted in the range of $150\,\mathrm{K} \leq T \leq 300\,\mathrm{K}$. The used cryostat features a 3D-vector magnet, which is capable of generating magnetic fields up to 6 T into the z-direction and up to 2 T in an arbitrary direction. The GdIG-disk is placed in a way, that the z-direction of the cryostat coincides with the crystallographic $[1\bar{2}1]$-direction of the sample.

We use the frequency-swept FMR (c.f. section 3.3), where the magnetic field $\mu_0 H_0$ is fixed and the frequency is swept through the FMR. The magnetic field is set in the range of $3.0\,\mathrm{T} \geq \mu_0 H_0 \geq 0\,\mathrm{T}$ with a step width of $\Delta\mu_0 H_0 = 10\,\mathrm{mT}$. This increases the measurement time drastically, as the vector magnet has to stabilize every set point of the magnetic field. The measurements are performed with a vector network analyzer, Agilent N5242A PNA-X, using the linear frequency mode and measuring the complex frequency-dependent transmission parameter S_{21} in the frequency range of $0.1\,\mathrm{GHz} \leq f \leq 26.5\,\mathrm{GHz}$ with 1080 frequency-points. In order to ensure an acceptable signal to noise ratio, the frequency traces are averaged 4 times and the IF bandwidth is set to 1 kHz. The acquired data were then processed by using the "derivative divide" algorithm [43] as discussed in section 3.3.

Exemplary data for GdIG-disk using different processing methods, was already shown in Fig. 3.2.

5.2 Magnetic Resonances (AFMR vs. FMR)

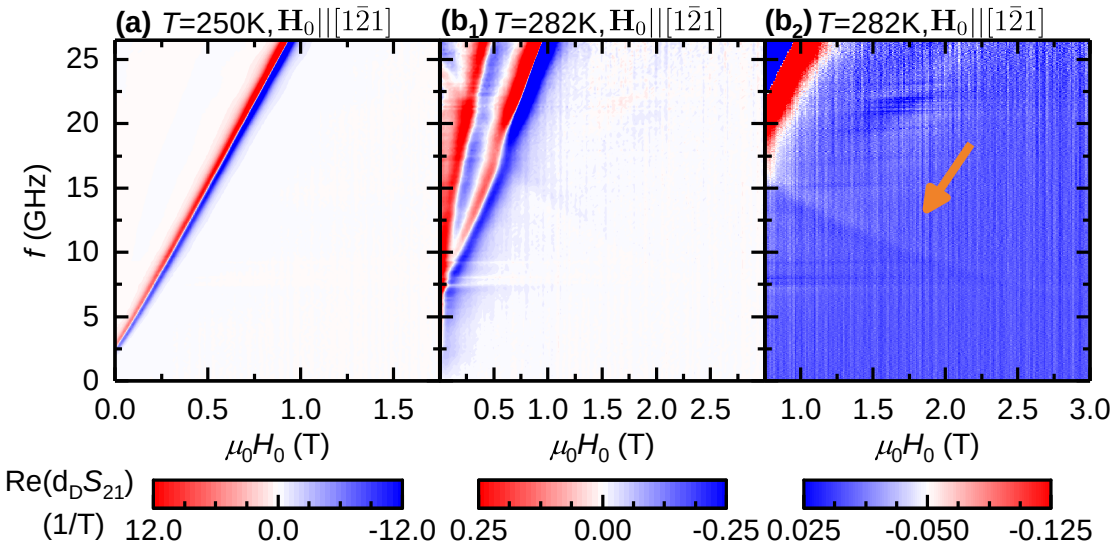

Figure 5.2: Real part of the background-subtracted transmission parameter $d_\mathrm{D}S_{21}$ using derivative divide at **(a)** $T = 250\,\mathrm{K}$ and at **(b)** $T = 282\,\mathrm{K}$ for a magnetic field along $\mathbf{H_0}||[1\bar{2}1]$. In **(a)** only the FMR is observable as the AFMR is shifted to higher frequencies, which were not observable due to the limited frequency range of the VNA. Note that the dispersion of the ferrimagnetic resonance follows $\partial f_\mathrm{res}/\partial H_0 > 0$. In $(\mathbf{b}_1)$ both the FMR and AFMR are observable, although the AFMR is very faint. The resonance on the left is probably due to a magnetic compound in the endlaunch. In $(\mathbf{b}_2)$ a limited range of $(\mathbf{b}_1)$ is shown with an adjusted colorbar range to get a better contrast for the AFMR. For the AFMR $\partial f_\mathrm{res}/\partial H_0 < 0$ holds in contrast to the FMR. Note that the colorbar range changes within these three plots as the amplitude of the resonances gets smaller the closer the temperature is to the compensation point.

Typical data for the $[1\bar{2}1]$-direction are shown in Fig. 5.2. For temperatures T far away from the compensation point T_comp only one magnetic mode is observable as depicted in Fig. 5.2**(a)**. This mode is the so-called low frequency mode or the ferrimagnetic resonance (FMR). This mode will be discussed in the following section 5.2.1.

If the temperature is close to the compensation point, another magnetic mode is noticeable as shown in Fig. 5.2$(\mathbf{b}_1)$. This magnetic mode is weak if compared to the FMR. We attribute this mode to an antiferromagnetic resonance (AFMR). The small contrast in Fig. 5.2$(\mathbf{b}_1)$ is due to the fact that the amplitude of the AFMR is proportional to $(g_1 - g_2)^2$, where g_i are the Landè-factors of the sublattices [70]. Therefore the colorbar is adjusted in order to get a better contrast (Fig. 5.2$(\mathbf{b}_2)$). The theoretical description is a little bit more challenging as it requires to take both sublattices into account. The antiferromagnetic resonance will be discussed in section 5.2.2.

The resonance on the left of the ferrimagnetic resonance (Fig. 5.2**(b$_1$)**) is probably due to a magnetic compound in the endlaunch. This resonance is not showing up at lower temperatures (Fig. 5.2**(a)**), because the amplitude of the ferrimagnetic resonance increases with decreasing temperatures. Close to the compensation point the magnitude of the FMR and AFMR is small and therefore the additional resonance is more present (compare the different colorbar scaling).

5.2.1 Ferrimagnetic Resonance (FMR)

In Fig. 5.2**(a)** a typical spectrum of the ferrimagnetic resonance is exemplary shown for $T = 250\,\mathrm{K}$ (below T_{comp}). It is important to note that the dispersion of the ferrimagnetic resonance is positive and follows $\partial f_{\mathrm{res}}/\partial H_0 > 0$. As we will see later, this is exactly opposite for the high frequency mode. In order to get a quantitative picture, frequency traces at constant magnetic field are extracted and the real and imaginary part are fitted simultaneously (c.f. Fig. 3.2). As the used processing method is derivative divide, Eq. (3.16) is used to fit the frequency data at fixed magnetic field.

From the fits, the resonance frequency f_{res} and the linewidth Δf_{res} is extracted. We first discuss the resonance frequency f_{res}. We fit the bulk Kittel equation (Eq. (2.16)) to f_{res} vs. H_0 and extract the Landè-factor g. For the Kittel fits, we use the demagnetization factors $N_x = 0.888$ and $N_y = N_z = 0.056$ obtained by modelling the disk as a general ellipsoid with semiaxes according to the dimensions of the disk and using the equations proposed in [71]. It is important to note, that the z-direction is defined as the direction of the applied magnetic field. The saturation magnetization M_{sat} is obtained from the SQUID-data measured by Stephan Geprägs and interpolated between the temperatures in order to reduce the number of fit parameters to two. The two remaining fit parameters are the anisotropy field H_{aniso} and the Landè-factor g.

The fitted g-factor as a function of temperature is shown in Fig. 5.3**(a)**. As clearly visible, the g-factor diverges to negative infinity, when coming from temperatures lower than the compensation point, and diverges to positive infinity, when coming from higher temperatures. The reason for this dispersive shape is that the compensation point for the angular momentum occurs at higher temperatures than the compensation point of the magnetization [72]. It is important to note, that there is a difference between these compensation points: At the angular momentum compensation point the net angular momentum vanishes and at the magnetization compensation the net remanent magnetization becomes zero [73].

From the already mentioned calculations of the sublattice magnetizations using molecular field theory, it is also possible to calculate the expected temperature-dependence of the effective Landè-factor of GdIG. Therefore

$$g_{\mathrm{eff}} = \frac{M_{\mathrm{Gd}} + M_{\mathrm{Fe,a}} - M_{\mathrm{Fe,d}}}{\frac{M_{\mathrm{Gd}}}{g_{\mathrm{Gd}}} + \frac{M_{\mathrm{Fe,a}}}{g_{\mathrm{Fe,a}}} - \frac{M_{\mathrm{Fe,d}}}{g_{\mathrm{Fe,d}}}} \tag{5.3}$$

is calculated, where $g_{\mathrm{Gd}} = 1.994$, $g_{\mathrm{Fe,a}} = 2.003$ and $g_{\mathrm{Fe,d}} = 2.0047$ are the g-factors of the Gd- and Fe-sublattices respectively and are taken from literature [72]. The gained trend is

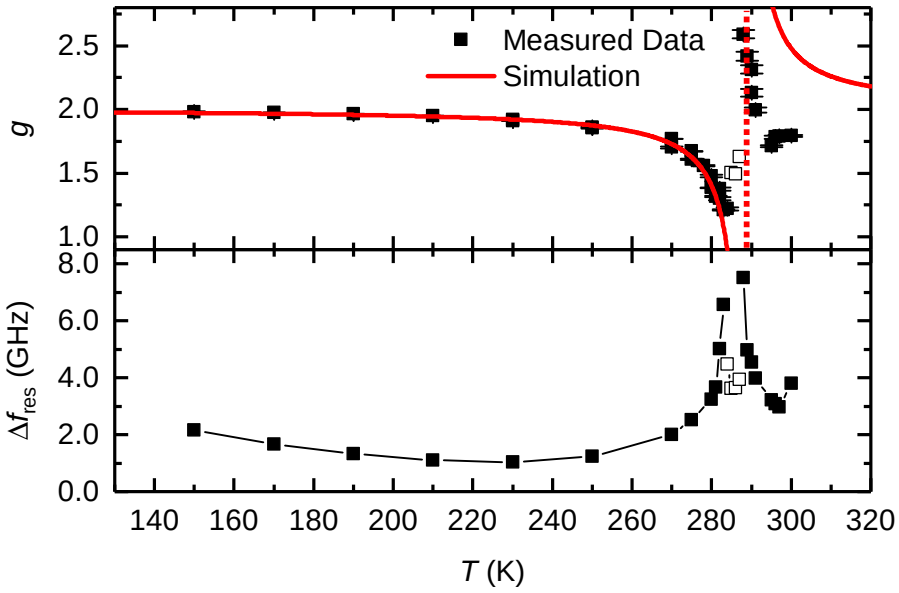

Figure 5.3: Evolution of typical FMR parameters of GdIG as a function of temperature. In **(a)** the fitted g-factor from Eq. (2.16) is shown (black symbols) with the simulated g-factor (red curve). The vertical red line indicates the compensation temperature, which was adapted to the compensation point of the SQUID-data. In **(b)** the linewidth Δf_{res} is shown for a fixed field of 0.50 T. The black solid line is a guide to the eye. The open symbols indicates the outliers close to the compensation point.

shown as a red curve in Fig. 5.3**(a)**. Below the compensation point the simulation describes the measured data well, although above T_{comp} the simulation predicts a slower decrease of the g-factor than our data shows. One possible explanation for this deviation could be, that the g-factors of the sublattices are also temperature-dependent, which is not considered in the calculation. The open symbols in Fig. 5.3 are the outliers close to the compensation point, where the amplitude of the FMR is very small and the fits become less reliable.

Now the extracted linewidth Δf_{res} of the FMR at a fixed magnetic field of $\mu_0 H_0 = 0.50\,\mathrm{T}$ is taken into consideration, which is shown in Fig. 5.3**(b)** as a function of temperature T. The linewidth varies at lower temperatures only in a small range and is more or less constant. The increasing linewidth with decreasing temperature is attributed to inhomogeneous broadening due to magnetostatic modes (MSMs), which are standing spin wave patterns due to the shape of the sample [74]. In the vicinity of the compensation point, the linewidth diverges to positive infinity. This behaviour is due to the rapid rise of the anisotropy field H_{aniso}, which also diverges at the compensation point (not shown), and due to the breakdown of the dipolar narrowing [72, 75].

Comparing the obtained data with literature, we could reproduce the theoretically expected behaviour of the g-factor and the linewidth near the compensation point. One should notice that in the discussion regarding the ferrimagnetic resonance the existence of two or more sublattices was irrelevant. Therefore it is justified to treat the ferromagnetic resonance in a ferrimagnet like in a ferromagnet.

5.2.2 Antiferromagnetic Resonance (AFMR)

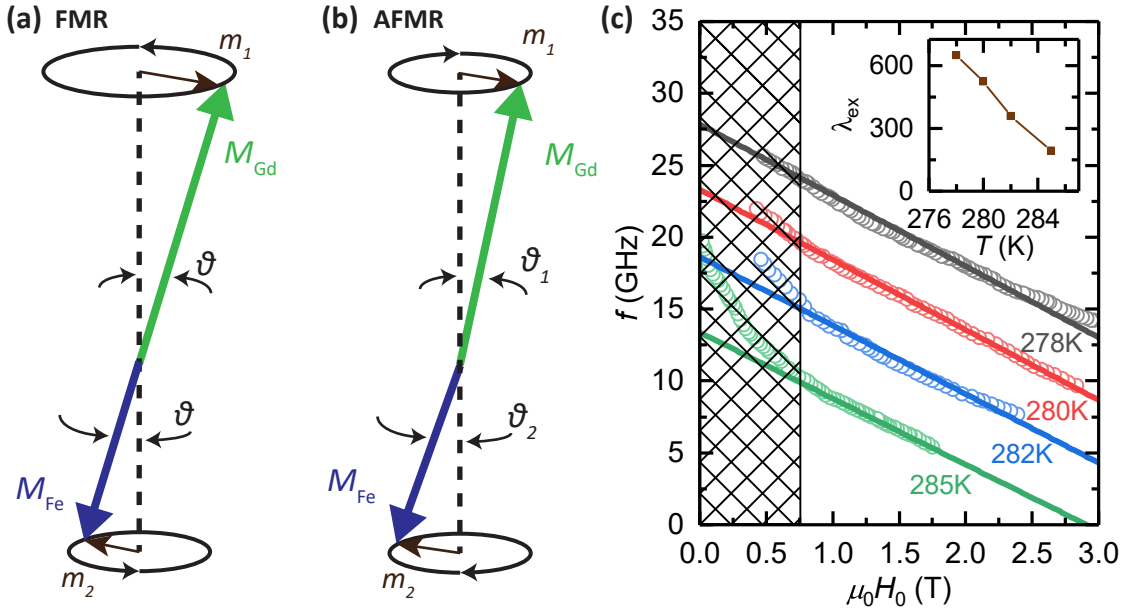

Figure 5.4: Precession of the magnetizations of the Gd-sublattice M_{Gd} and the coupled Fe-sublattice M_{Fe} of **(a)** the ferrimagnetic resonance (FMR) and **(b)** the antiferromagnetic resonance (AFMR). **(a)** For the ferrimagnetic resonance, both magnetizations are aligned and precess in-phase. Therefore the angle of the magnetizations θ relative to the equilibrium position are the same. **(b)** As the oscillating parts of the magnetizations m_i are almost the same (tiny difference not shown), the angles θ_i are now different. **(c)** The resonance frequency of the antiferromagnetic resonance for different temperatures shown as a function of the magnetic field. The points are the extracted data and the solid lines are the calculated curves according to [25]. The shaded region indicates the magnetic field region, where the AFMR cannot described by the simulation due to the coupling between the FMR and AFMR (see section 5.3). The inset shows the fitted molecular exchange constant λ_{ex} as a function of temperature T. The lines are added as a guide to the eye.

For the antiferromagnetic resonance, both sublattices have to be taken into account as depicted in Fig. 5.4**(a)** and **(b)**. In contrast to the ferrimagnetic resonance (Fig. 5.4**(a)**), where the magnetizations of the sublattices are aligned and precess in the same sense, the magnetizations of the sublattices are not aligned for the antiferromagnetic resonance (Fig. 5.4**(b)**). Additionally, the magnetizations now precess clockwise compared to the ferrimagnetic mode, where they precess counterclockwise [25].

In order to describe the antiferromagnetic resonance as shown in Fig. 5.4**(c)** for various temperatures, the properties of the two sublattices have to be taken independently into account. The AFMR resonance frequency is extracted by hand as the signal-to-noise ratio of the data is insufficient in order to fit it. The coupling between the sublattices is described by Nèel theory. The following calculation is based on [24] and [25], where a more extensive discussion on the antiferromagnetic resonance can be found. We start with the

Landau-Lifshitz equation (Eq. (2.6)), which is modified by an exchange term $\lambda_{ij}\mathbf{M}_j$. This leads to

$$\omega \times \mathbf{M}_i = \gamma_i \mathbf{M}_i \times \left(\mathbf{H}_0 + H_{\mathrm{aniso},i} - \sum_{i \neq j} \lambda_{ij} \mathbf{M}_j \right) \quad \text{with } i,j \in \{1,2\}, \tag{5.4}$$

where we used that $\mathrm{d}\mathbf{M}_i/\mathrm{d}t = \omega \times \mathbf{M}_i$ and i, j accounts for the number of sublattices (here 2). As only two sublattices are considered, the sum disappears and the molecular exchange constant λ_{ij} is rewritten to $\lambda_{ij} = \lambda_{\mathrm{ex}}$. Under the assumption, that the external magnetic field $\mathbf{H}_0$ is applied in the z-direction, this equation can be written down for each sublattice and the calculations can be performed equivalently to section 2.2.1. This finally leads (without derivation) to a quadratic equation for the resonance frequency [25]

$$\omega^2 + A\omega + B = 0 \tag{5.5}$$

with

$$\begin{aligned} A &= (\gamma_1 + \gamma_2) \cdot H_0 + \gamma_1 H_{\mathrm{aniso},1} - \gamma_2 H_{\mathrm{aniso},2} + \lambda_{\mathrm{ex}} \cdot (\gamma_1 M_2 - \gamma_2 M_1) \\ B &= \gamma_1 \gamma_2 \left[(H_0 + H_{\mathrm{aniso},1})(H_0 + H_{\mathrm{aniso},2}) + \lambda_{\mathrm{ex}} \left(H_0 \left(M_1 - M_2 \right) - M_1 H_{\mathrm{aniso},1} - M_2 H_{\mathrm{aniso},2} \right) \right]. \end{aligned} \tag{5.6}$$

For the gyromagnetic ratios $\gamma_i = g_i \mu_{\mathrm{B}}/\hbar$, the g-factors of the sublattices taken from [72] are plugged in (c.f. section 5.2.1). As we do not have information about the anisotropy fields of the respective sublattices, we assume that $H_{\mathrm{aniso}} = H_{\mathrm{aniso},1} = H_{\mathrm{aniso},2} = 2K_1/M_{\mathrm{sat}}$. Only a cubic anisotropy is taken into consideration with the anisotropy constant $K_1 = 4.1 \times 10^2\,\mathrm{J/m^3}$ [65]. The saturation magnetization is taken from the SQUID-measurements.

The only unknown parameter is the molecular exchange constant λ_{ex}. Therefore Eq. (5.5) is solved using Mathematica and the exchange constant λ_{ex} is taken as a fitting parameter. The resulting AFMR curves are shown in Fig. 5.4**(c)** as solid lines. For decreasing temperatures the AFMR is shifted to higher frequencies until they are out of our accessible frequency range ($f \leq 26.5\,\mathrm{GHz}$). In the inset of Fig. 5.4**(c)** the fitted molecular exchange constant λ_{ex} is shown as a function of temperature T. For decreasing temperatures the exchange constant increases such as the saturation magnetization (c.f. Fig. 5.1**(a)**) because from Nèel theory the saturation magnetization is proportional to the exchange constant. Consequently, the exchange constant λ_{ex} goes to zero at the compensation temperature T_{comp}.

The mismatch at high magnetic fields, where the AFMR slightly bends, is due to the small misalignment of the magnetic field to the $[1\bar{2}1]$-direction ($\approx 1°$) as shown in [76]. At low magnetic fields the curves cannot describe the data due to the coupling to the ferromagnetic resonance, which will be discussed in the next section.

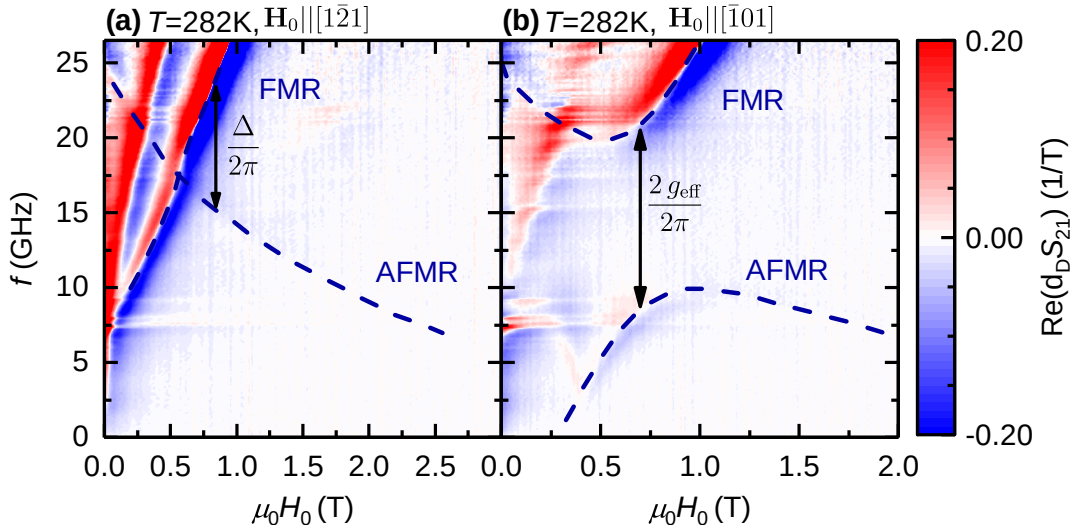

Figure 5.5: Measured colormaps of the weak **(a)** and the strong coupling **(b)** regime at $T = 282\,\mathrm{K}$. The FMR and the AFMR are indicated with dashed blue lines as especially the intensity of the AMFR is low.

5.3 Coupling of AFMR and FMR

Previously we have treated the antiferromagnetic (AFMR) and the ferromagnetic resonance (FMR) independently of each other. In a certain temperature range some "cross-talk" between these two modes can be observed as shown in Fig. 5.5**(a)**. In the previous discussions the magnetic field was applied in the [1$\bar{2}$1]-direction because qualitatively the other directions in the disk plane show the same behaviour regarding the FMR and AFMR. The only thing what changes between these crystallographic directions is the anisotropy field. Nevertheless by now rotating the magnetic field by 90°, which corresponds to the [$\bar{1}$01]-direction, a clear anti-crossing between the FMR and the AFMR is observable as shown in Fig. 5.5**(b)**.

In the following we discuss the distinct behaviours between the [1$\bar{2}$1]- and the [$\bar{1}$01]-direction, where on the one side weak and on the other strong coupling is observed. It should here be noted, that in discussions of coupling phenomena the involved coupling strength and the linewidths have in literature the units of an angular frequency (rad/s).

5.3.1 Weak Coupling

Along the [1$\bar{2}$1]-direction the ferromagnetic as well as the antiferromagnetic resonance is observed as shown in Fig. 5.5**(a)**. At the crossing point of the FMR and AMFR a small "kink" in the FMR can be seen. To illustrate this behaviour both the FMR and the AFMR resonance frequencies are shown with dashed blue lines.

To get a more quantitative picture, the frequency difference $\Delta(\mu_0 H_0)/2\pi = f_{\mathrm{res,FMR}}(\mu_0 H_0) - f_{\mathrm{res,AFMR}}(\mu_0 H_0)$ between the FMR and the AFMR is extracted, which is also indicated in Fig. 5.5**(a)**. As the intensity of the FMR is larger than of the AFMR, fixed magnetic field slices of the FMR are fitted and the linewidth $\mathrm{d}f_{\mathrm{res}}$ is extracted. It is important to

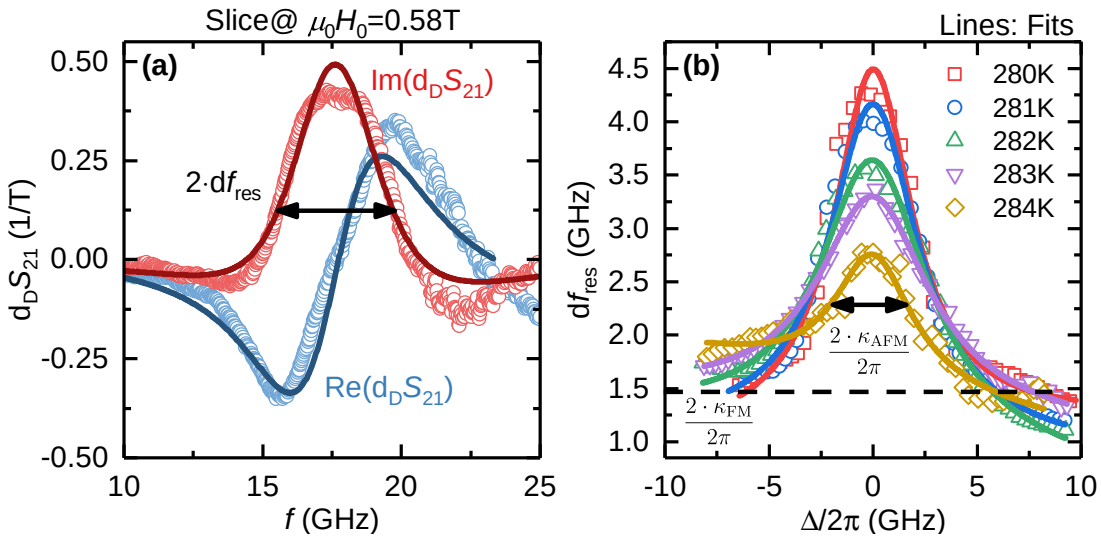

Figure 5.6: Linewidth extraction for the weak coupling regime. In **(a)** the real and imaginary part of $d_D S_{21}$ is fitted exemplary at a field cut of 0.58 T in order to extract the linewidth df_{res}. **(b)** The extracted linewidths df_{res} are plotted as a function of the frequency difference between the FMR and AMFR and are then fitted by the model of Herskind [77] with Eq. 5.7 in order to extract the coupling strength $g_{eff}/2\pi$ and the linewidths of the FMR and the AFMR $\kappa/2\pi$.

note, that in literature the linewidths in coupling phenomena are always defined as half width at half maximum (HWHM), as it will also be used here. Upon the crossing point a broadening of the linewidth is observed as depicted in Fig. 5.6**(a)**.

Following the approach of Herskind *et al.* [77] the extracted linewidths df_{res} are plotted as a function of the frequency difference $\Delta/2\pi$ in Fig. 5.6**(b)** for various temperatures. The Lorentzian lineshape can now be fitted by using [77, 78]

$$2\pi\, df_{res}(\Delta) = \kappa_{FM} + g_{eff}^2 \frac{\kappa_{AFM}}{\kappa_{AFM}^2 + \Delta^2}, \tag{5.7}$$

where κ_{FM} and κ_{AFM} are the linewidths of the FMR and the AFMR respectively and g_{eff} is the coupling strength. As depicted in figure 5.6**(b)**, κ_{FM} is given by the offset and describes the linewidth of the undisturbed system. The linewidth of the AFMR κ_{AFM} is as indicated the HWHM linewidth of the Lorentz curve.

The gained parameters are shown in Fig. 5.7**(a)**. A discussion will be given later in section 5.3.3.

5.3.2 Strong Coupling

By applying a magnetic field along the [$\bar{1}$01]-direction, the ferrimagnetic and the antiferromagnetic resonance interact strongly and the characteristic anti-crossing forms as seen in Fig. 5.5**(b)**. In order to describe this coupled system, we assume the FMR and the AFMR

are modelled as two coupled harmonic oscillators. The coupling might be mediated by dipolar interaction[1].

This system can mathematically described by [78]

$$2\pi f_{\pm}(\mu_0 H_0) = 2\pi f_{\text{res, AFMR}}(\mu_0 H_0) + \frac{\Delta(\mu_0 H_0)}{2} \pm \frac{1}{2}\sqrt{\Delta(\mu_0 H_0)^2 + 4g_{\text{eff}}^2}, \tag{5.8}$$

where the resonance frequencies $f_{\text{res, AFMR}}$ and $f_{\text{res, FMR}}$ are taken from the $[1\bar{2}1]$-direction. The effective coupling strength g_{eff} is given by the minimum of the frequency splitting between the two branches. The coupling strength is then two times this value. In order to confirm the extracted value, it is plugged into Eq. (5.8) and the gained curves are then overlayed to the colormap as shown in Fig. 5.5**(b)** as blue curves. The calculated curve is in good agreement with the measured data.

In order to be able to distinguish between the different coupling regimes, it is also necessary to take the linewidth into account. For the strong coupling regime, it is necessary to fit a magnetic field slice far away from the crossing point to extract the undistorted linewidth κ of the FMR and the AFMR respectively. The gained values of the linewidths κ and the effective coupling strength g_{eff} are shown in Fig. 5.7**(b)**. It is important to note that due to the low magnitude of the AFMR the error of the linewidth is larger because the AFMR is barely larger than the noise floor.

5.3.3 Comparison of Weak and Strong Coupling

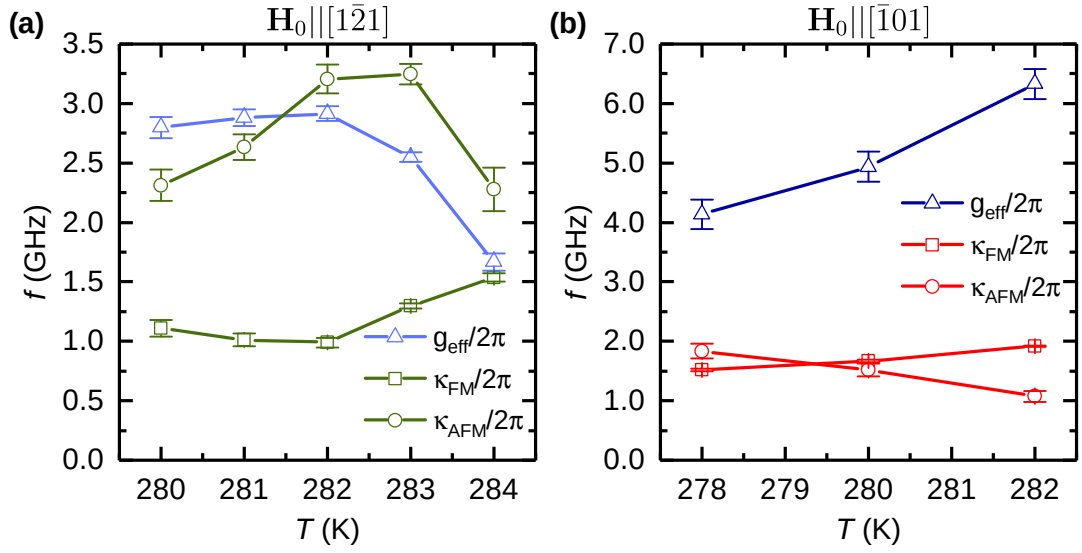

Figure 5.7: Comparison of the coupling strength $g_{\text{eff}}/2\pi$ and the linewidths of the FMR and the AFMR $\kappa/2\pi$ for the strong **(a)** and the weak coupling regime **(b)**. The approach in order to extract the shown parameters is shown for **(a)** in section 5.3.1 and for **(b)** in section5.3.2.

[1]From private communication with Akashdeep Kamra (University of Konstanz).

The gained values for the effective coupling strength g_{eff} and the linewidths κ of the undistorted system are shown in Fig. 5.7 for the $[1\bar{2}1]$- and the $[\bar{1}01]$-direction respectively. The strong coupling regime is characterized by a coupling constant g_{eff}, which is much larger than both the linewidths κ of the two undistorted systems [77, 79]. The system is claimed to be in the weak coupling regime, if the coupling strength g_{eff} is smaller or in the order of the linewidths κ.

In the $[1\bar{2}1]$-direction, as depicted in Fig. 5.7**(a)**, the effective coupling strength g_{eff} is barely larger than the AFMR linewidth κ_{AFM} in the temperature range $T = 280 - 281\,\text{K}$ and at higher temperatures it becomes smaller, while the linewidth of the FMR remains more or less constant. The system is therefore found to be in the weak coupling regime.

Along the $[\bar{1}01]$-direction as shown in Fig. 5.7**(b)** the situation is completely different. The effective coupling strength g_{eff} is always at least two times larger than the individual linewidths κ. Therefore the system is clearly in the strong coupling regime.

The shown temperatures in Fig. 5.7**(b)** are limited due to the already discussed reasons: The antiferromagnetic resonance shifts to higher frequencies for lower temperatures until they are not accessible anymore due to the limited frequency range of the VNA and the closer the temperature gets to the compensation point T_{comp} the magnitude of the FMR and AFMR gets smaller until especially the AFMR is no longer detectable.

5.4 Summary

In this chapter we investigated the magnetization dynamics of the compensating ferrimagnet gadolinium iron garnet in the form of a single crystalline disk by using a frequency-swept VNA-FMR. In contrast to the ubiquitous yttrium iron garnet (YIG), gadolinium iron garnet features a compensation point T_{comp}, where the magnetizations of the two sublattices cancel each other out. In an external magnetic field and by driving the system with a microwave, it is possible to observe two magnetic modes: the ferrimagnetic and the antiferromagnetic resonance. First, they were described independently from each other, then the coupling between these two magnetic modes was considered.

In the ferrimagnetic mode (FMR) the magnetization of the Gd- and the effective Fe-sublattice are aligned and precess in the same sense. Therefore the system behaves in the FMR mode like a ferromagnet and can be treated as one. For the FMR we extracted the Landè-factor g, which when coming from temperatures lower than the compensation temperature diverges to negative infinity at the compensation point and comes back from positive infinity at higher temperatures. This behaviour is in agreement with theory. Furthermore the linewidth at a fixed magnetic field was extracted, which diverges to positive infinity at the compensation point. This is also in accordance with theory.

For the antiferromagnetic resonance (AFMR) the magnetizations of the sublattices are not aligned. The dispersion of the AFMR is negative, in contrast to the positive FMR dispersion. In the accessible frequency range the AFMR could be described by using Nèel theory and fitting the molecular exchange constant λ_{ex}, which becomes smaller the closer the temperature is to the compensation point.

By applying the magnetic field along the $[1\bar{2}1]$-direction, weak coupling between the ferrimagnetic and the antiferromagnetic resonance was observed. In the weak coupling regime the FMR features a small "kink" at the crossing point with the AFMR. By following the approach of Herskind *et al.* [77], it was possible to extract the effective coupling strength g_{eff} and the linewidths κ of the undisturbed systems (FMR and AFMR).

In the $[\bar{1}01]$-direction the ferrimagnetic and the antiferromagnetic mode interact strongly and the characteristic anti-crossing can be observed. The system is modelled as two harmonic oscillators, which are coupled to each other. The effective coupling strength g_{eff} is here given by the minimal frequency splitting of the anti-crossing. As the coupling strength is at least to times larger than the individual linewidths the system can be classified as strongly coupled.

Due to the limited frequency range of the used vector network analyzer ($f \leq 26.5\,\text{GHz}$), it was only possible to observe the antiferromagnetic resonance in a limited temperature range because the AFMR shifts to higher frequencies for decreasing temperatures. This is also the reason, why especially the strong coupling regime could only be observed for a very limited temperature range (c.f. Eq. (5.8) and Fig. 5.7**(b)**).

In a next iteration of this experiment, it would be advantageous to use a vector network analyzer, which is capable of higher frequencies (e.g. $f \leq 50\,\text{GHz}$). In this way the AFMR could be observed up to lower temperatures and consequently the coupling phenomena between the FMR and the AFMR could be investigated more extensively.

Chapter 6

Dynamic Skyrmion Melting in Cu_2OSeO_3

After discussing the magnetization dynamics in normal metal/ferromagnet bilayers (chapter 4) and in a compensating ferrimagnet (chapter 5), we now switch to a more complicated magnetic system, which is a chiral magnet. The magnetic order in the already discussed ferromagnet and ferrimagnet is due to the Heisenberg exchange interaction, where the spins in the system are either aligned in parallel or antiparallel. In a chiral magnet, the so-called Dzyaloshinskii-Moriya interaction [80, 81] is responsible for a canting of the spins. As a consequence, the spins are helically or conically aligned.

If both Dzyaloshinskii-Moriya and Heisenberg exchange interaction are present and of comparable magnitude, a so-called skyrmion-lattice ground state can emerge. Skyrmions are topologically protected spin solitons with a particle-like behaviour, which were first discovered in the metallic MnSi in 2011 by Mühlbauer *et al.* [10] using a neutron scattering experiment. Due to their long lifetime and their nanometer-sized dimensions [82], skyrmions are promising candidates for future race track memory [83], GHz oscillators [84] and logic devices [85].

Therefore it is necessary to investigate the properties of the magnetization dynamics of the skyrmionic system. Onose *et al.* [86] and Schwarze *et al.* [87] pioneered the investigation of the magnetization dynamics of the insulating Cu_2OSeO_3, the metallic MnSi and the semiconducting $Fe_{1-x}Co_xSi$, which all share the same cubic space group $P2_13$. In order to detect the spin excitations in these materials, these authors used a broadband ferromagnetic resonance setup with a vector network analyzer and a coplanar waveguide.

In this chapter, we investigate the magnetization dynamics of the insulating Cu_2OSeO_3 using a broadband VNA-FMR setup. In contrast to the previous experiments, we however perform the skyrmion excitations with very large microwave power. As proposed by Mochizuki [15], such strong driving of the skyrmion resonance can result in a "melting" of the skyrmion lattice.

We start with an introduction into the basics and dynamic excitations of skyrmions in section 6.1. In section 6.2, the concept of melting of the skyrmion lattice by intense microwave irradiation proposed by Mochizuki is briefly discussed. Here, we also discuss the small angle neutron scattering experiments, that were performed on the same sample by Franz Haslbeck from the group of Christian Pfleiderer (TU Munich). In section 6.3, the two used microwave spectroscopy setups, referred to as 2-tone experiment and broadband magnetic resonance setup (bFMR) will be discussed. Additionally, the data analysis steps and the procedure in order to extract a phase diagram are outlined. In the last two

sections 6.4 and 6.5, the results of the 2-tone and the bFMR measurements are discussed. Here, we also discuss the employed temperature correction procedure.

6.1 Introduction to Skyrmions and their Dynamics

In a chiral magnet, the most prominent interactions are the the Heisenberg exchange and the Dzyaloshinskii-Moriya interaction or short DMI. For the occurrence of the DMI two requirements have to be fulfilled: First strong spin-orbit interaction needs to be present [88] and second a broken inversion symmetry is needed. The second precondition can be directly seen from the mathematical form of the Hamiltonian of the DMI [16]

$$\mathcal{H}_{\mathrm{DMI}} = \mathbf{D}_{ij} \cdot (\mathbf{S}_i \times \mathbf{S}_j), \tag{6.1}$$

with the spins $\mathbf{S}_i$ and the Dzyaloshinskii vector $\mathbf{D}_{ij}$. By inverting the term in the bracket and in the presence of a given inversion symmetry, the Dzyaloshinskii vector has to be zero ($\mathbf{D}_{ij} = 0$). Therefore DMI can only be present in a system with broken inversion symmetry. The broken inversion symmetry is generally fulfilled at interfaces and surfaces, leading to interfacial DMI [89]. Another possibility is a crystal structure with a broken inversion symmetry. This is, for example, given for the non-centrosymmetric cubic Cu_2OSeO_3, MnSi and $Fe_{1-x}Co_xSi$, which all posses the same space group $P2_13$ [90].

In contrast to the Heisenberg exchange interaction, which leads to a parallel or anti-parallel alignment of the spins, the Dzyaloshinskii-Moriya interaction leads to a canting of the spins. As seen from Eq. (6.1), the energy of the DMI is minimized, if the spins are canted by 90° to each other. This leads, depending on the direction of the Dzyaloshinskii vector $\mathbf{D}_{ij}$ relative to the space vector connecting the spins $\mathbf{S}_i$ and $\mathbf{S}_j$, to a helical or a cycloidal ordering. The helical ordering is depicted in Fig. 6.1**(b)**. In the helical phase, the spins are aligned on a helix. It is interesting to note, that the DMI leads to intrinsically periodic magnetic properties [90].

As already mentioned, if the Dzyaloshinskii-Moriya and the Heisenberg exchange interaction become comparable, skyrmions can emerge. Skyrmions are spin structures with a finite size in the range of 10 nm − 100 nm [91]. The size of the skyrmion is determined by the ratio $|\mathbf{D}_{ij}|/J$, where J is the Heisenberg exchange integral. A schematic of a skyrmion is shown in Fig. 6.1**(d)**. By taking a cut through the middle of the skyrmion and looking at the resulting configuration of the spins, one recovers a helical ordering. This is the reason, why this type of skyrmions is referred as helical- or Bloch-type. There also exist so-called cycloidal- or Nèel-type skyrmions [92], which we do not want to discuss here.

Another characteristic of skyrmions is the emergence of a lattice with a hexagonal symmetry for bulk materials as depicted in Fig. 6.1**(e)**. This so-called skyrmion crystal forms in a simple picture due to close-packing of equal disks. The skyrmions are two-dimensional structures and the spacing between the skyrmions is minimized by the hexagonal arrangement. In a neutron scattering experiment this hexagonal symmetry is recovered. A more sophisticated explanation of the hexagonal symmetry including experimental neutron scattering data can be found in [10].

Now, we want to briefly discuss the topological aspect of the skyrmions. Skyrmions were first proposed by T. Skyrme in 1962 [93], who described the stability of hadrons due to topological protection. Interestingly, his concepts are also applicable to problems in condensed matter physics like in quantum Hall systems or liquid crystals [91]. The skyrmion itself can be assigned with a topological charge, which is coming from the fact, that the spin in the middle is exactly opposed to the spins at the edge of the skyrmion. Additionally, skyrmions have a topological skyrmion number, which is related to the vorticity and counts how many times the skyrmion wraps around the unit sphere [91].

From a topological point of view, one can transform a doughnut into coffee cup and vice versa because they both have one hole, which is their topologically protected Chern number. On the contrary these two objects cannot be transformed into a ball because the ball has no hole. The same line of thinking can be applied to the skyrmions, which are not classified by the number of holes but by the before mentioned topological charge. This topological protection gives the skyrmions their stability.

After this discussion of the basic concepts of skyrmions, we now discuss the magnetic properties and dynamic excitations of these systems.

6.1.1 Magnetic Modes in Skyrmion Materials

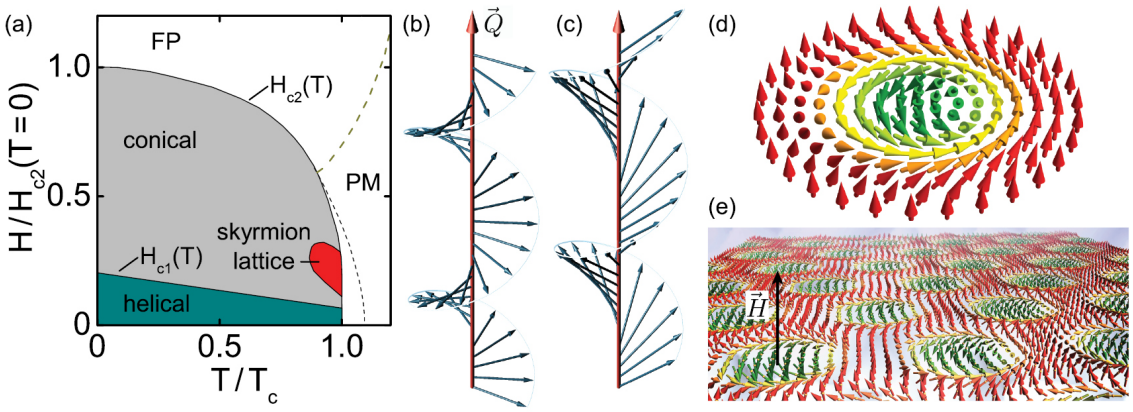

Figure 6.1: **(a)** Typical phase diagram of a chiral magnet hosting skyrmions. Above the critical temperature T_c the material behaves like a paramagnet (PM). The magnetic field at the phase transition from ferrimagnetic/field polarized (FP) to conical is labelled H_{c2} and from conical to helical H_{c1}. **(b)** Schematic of helical mode and **(c)** conical mode with the propagation vector $\vec{Q}$. **(d)** Spin arrangement of a helical- or Bloch-type skyrmion. **(e)** Hexagonal symmetry of the skyrmion lattice with perpendicular applied magnetic field $\vec{H}$. Figure taken from [90].

Spin dynamics in Cu_2OSeO_3 were first investigated by Onose *et al.* [86] in 2012. They were able to identify the characteristic eigenmodes of a chiral magnet, which also hosts a skyrmionic phase. The phase diagram, depicted in Fig. 6.1**(a)**, shows four distinct magnetic modes below the critical temperature T_c. Starting at low fields, there is the helical phase, where the spins are aligned on a helix along a crystalline easy axis, which is parallel to the

propagation vector $\vec{Q}$. As shown in Fig. 6.1**(b)**, the magnetization along the propagation vector $\vec{Q}$ is zero.

By applying a magnetic field the spins of the helical mode start to tilt towards the propagation vector as shown in Fig. 6.1**(c)**. Consequently, the conical spin arrangement has a finite magnetization parallel to the applied magnetic field. By driving a collective excitation (FMR) of the conical phase, two modes can be observed. The spins can then either precess with phase velocity parallel to the pitch vector $\vec{Q}$, which is called the Q_+ mode, or antiparallel, which is then the Q_- mode [87]. The same can be observed in the helical phase.

By further increasing the magnetic field, the material loses its chiral structure and becomes a ferrimagnet. The magnetic mode is then also referred to as the field-polarized mode. We have already discussed and derived the resonance frequency for this mode in section 2.2, when discussing the magnetization dynamics of a bulk material. Using the Kittel equation for bulk materials (Eq. (2.16)) and neglecting anisotropies ($H_{\text{aniso}} = 0$), as the Heisenberg exchange interaction and the DMI are dominating, we get the resonance frequency $f_{\text{res,FP}}$ for the field-polarized mode [31]

$$f_{\text{res,FP}} = \frac{g\mu_{\text{B}}}{h}\,\mu_0 \sqrt{(H_0 + (N_x - N_z)\cdot M)\cdot(H_0 + (N_y - N_z)\cdot M)}, \tag{6.2}$$

with the magnetization M, the Bohr magneton μ_{B} and the Planck constant h.

In a limited regime close to the critical temperature T_{c}, a skyrmion lattice forms. In the skyrmion (SkX) phase three distinct magnetic modes can be observed. Two of these are the clockwise (cw) and the counterclockwise (ccw) rotational modes, where the core of the skyrmion rotates in the clockwise or the counterclockwise rotation respectively. The third magnetic mode is the breathing mode, where the core of the skyrmion alternatingly shrinks and expands [86]. As we will see later in our experimental data (Sec. 6.3.1), only two of these modes are observed, which are the breathing and the counterclockwise mode, because the intensity (spectral weight) of the clockwise mode is very small.

The identification of the discussed magnetic modes in the experimental data is done in section 6.3.1 and the procedure to extract a phase diagram, similar to that in Fig. 6.1**(a)**, will be shown in section 6.3.2. In the next section we want to briefly discuss the theory paper by M. Mochizuki [15], who proposed a melting of the skyrmion lattice by large microwave power. Further, we show the data obtained from small angle neutron scattering experiments (SANS) performed by Franz Haslbeck.

6.2 Motivation: Melting of Skyrmions with Large Microwave Power

Masahito Mochizuki theoretically studied in 2012 [15] spin excitations in the skyrmion (SkX) phase. Starting with a Hamiltonian containing the Heisenberg exchange interaction, Zeeman coupling and the DMI and by numerically solving the Landau-Lifshitz-Gilbert equation for a two-dimensional square lattice with a constant magnetic field, he reproduced characteristics of the skyrmion lattice. He observed the hexagonal symmetry of the skyrmion

lattice and further could describe the dynamic properties of the skyrmion by additionally applying a small oscillating magnetic field. The calculations show the evolution with time of the three magnetic modes (ccw, cw, breathing).

Furthermore he observed the loss of the hexagonal symmetry of the skyrmion lattice by irradiating the material with a microwave of large power. The system then transitions into a state without any long-range ordering. This means that the long range stability of the skyrmion lattice is overcome by the dynamic excitations. This process is, as suggested by M. Mochizuki, called "melting" of the skyrmion lattice. The melting occurs within a few nanoseconds and is due to the intensely excited rotational spinwave modes, in particular the counterclockwise mode with its large intensity.

In order to prove this theoretical perediction of the "melting" of the skyrmion lattice, neutron scattering experiments under intense microwave radiation were performed by Franz Haslbeck of the group of Christian Pfleiderer (TUM) in a collaboration with the Walther-Meißner-Institut. The experimental setup and the gained results shall be briefly discussed in the following section.

6.2.1 Neutron Scattering Experiments

The experimental setup for the small angle neutron scattering (SANS) experiment [94] performed by Franz Haslbeck is depicted in Fig. 6.2**(a)**. The Cu_2OSeO_3 sample is mounted on a coplanar waveguide (center conductor width $w_{cc} = 1.3\,\mathrm{mm}$) and placed in a magnet cryostat. A frequency source and a microwave amplifier capable of a maximum output power of $P = 5\,\mathrm{W}$ produce a driving field $\mathbf{h}_{rf}$ at the sample.

In order to observe the hexagonal skyrmion lattice, the static magnetic field $\mathbf{H}_0$ is applied in the same direction as the neutron beam, which corresponds to the [110]-direction of the Cu_2OSeO_3 crystal. The magnetic field is fixed at $\mu_0|\mathbf{H}_0| = 22\,\mathrm{mT}$. The number of scattered neutrons is then detected as a function of the transversal neutron wavevector. From this SANS data [10] the intensity of the signal of the conical and skyrmion phase is extracted.

The signal intensity I stemming from scattering off the magnetic lattice is shown in Fig. 6.2**(b)** as a function of the corrected temperature $T_c - T$. The critical temperature T_c is defined as the temperature, where the skyrmion and conical intensity become zero. By applying a power of $P_{drive} = 5\,\mathrm{W}$ and by varying the frequency of the frequency source f_{drive}, it is observed, that at $f_{drive} = 0.6\,\mathrm{GHz}$ the response of the system is unchanged compared to no applied microwave power. In the range of $0.7\,\mathrm{GHz} \leq f_{drive} \leq 1.0\,\mathrm{GHz}$ the magnitude of the skyrmion signal is strongly suppressed but comes back nearly to its original magnitude at $f_{drive} = 1.2\,\mathrm{GHz}$.

Figure 6.2**(c)** shows SANS data obtained at fixed frequency $f_{drive} = 0.8\,\mathrm{GHz}$, when varying the microwave power. As depicted in Fig. 6.2**(c)** the "melting" of the hexagonal skyrmion lattice is a continuous process with no real threshold. The loss of the SkX signal means, that the spin-system gets in a disordered state (like an amorphous material) and loses its regular magnetic ordering. Therefore the wavevector is not defined and in the neutron scattering experiment no signature of skyrmions is observable anymore.

In conclusion, the neutron scattering experiment shows, that a "melting" of the skyrmion

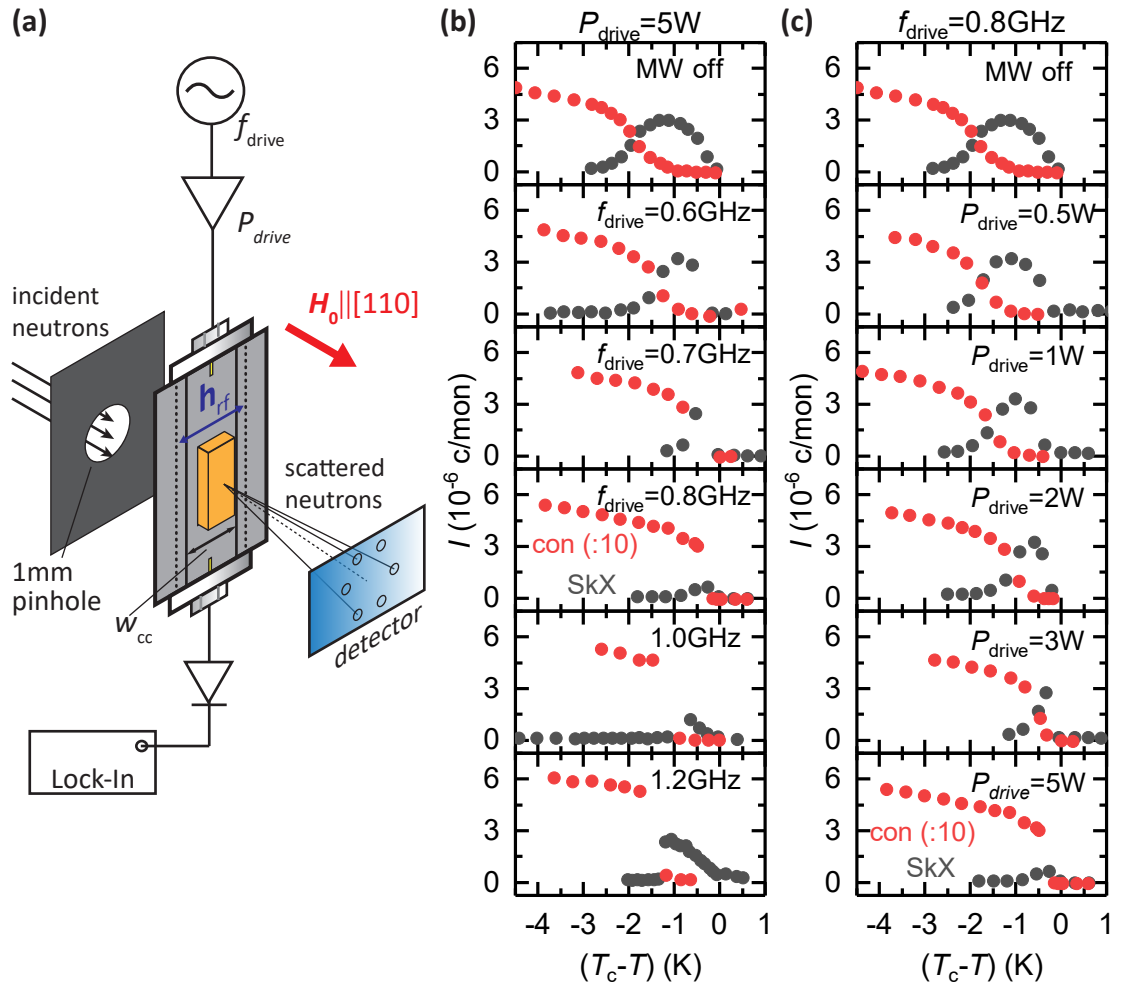

Figure 6.2: Neutron scattering experiment for the Cu_2OSeO_3 crystal performed by F. Haslbeck. **(a)** Illustration of neutron scattering setup. Intensity of the skyrmion and conical phase as a function of the corrected temperature $T_c - T$ for **(b)** various microwave frequencies f_{drive} and **(c)** microwave powers P_{drive}. The conical signal is divided by a factor of 10. Data is reproduced with permission of F. Haselbeck and C. Pfleiderer.

lattice is observable as the signal of the SkX phase is lost. This means, that the long-range ordering of the skyrmion crystal is not present anymore.

6.3 Experimental Setup and Processing

In this chapter we investigate the spin dynamics of a cuboid Cu_2OSeO_3 crystal, obtained from the group of Christian Pfleiderer (TUM). Our experiments are performed using a broadband ferromagnetic resonance setup at cryogenic temperatures with a coplanar waveguide (CPW) and a vector network analyzer (VNA). The crystal, with dimensions and crystallographic directions as shown in Fig. 6.3**(a)**, is chosen to be small and the CPW center conductor width of $w_{cc} = 1.3\,\text{mm}$ is chosen wider than the sample. The long side of the sample is aligned parallel to the center conductor to achieve a homogeneous excitation

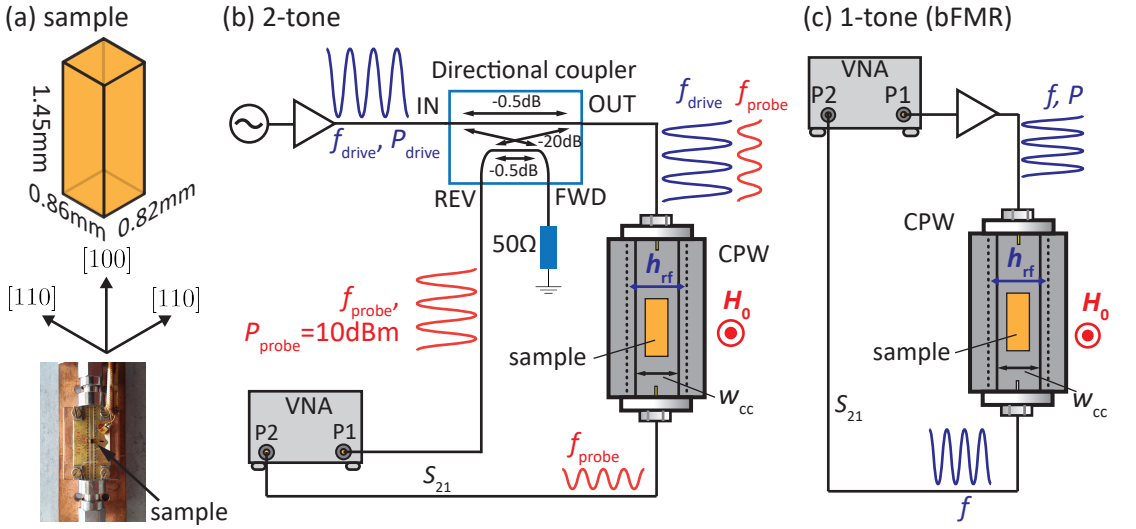

Figure 6.3: **(a)** Geometry and crystallographic axes shown for the given Cu_2OSeO_3 crystal with a picture of the mounted sample on the CPW. **(b)** 2-tone measurement with a frequency source at a fixed frequency f_{drive}, which drives the system with large microwave power P_{drive}. With the directional coupler the frequency of the VNA is superimposed with the large frequency source signal but with an attenuation of typically $-20\,\mathrm{dBm}$. **(c)** Single-tone setup (bFMR), which equals the already explained setup in chapter 3, but with an additional amplifier in order to get to high microwave power P.

field over the whole sample. The large sample volume (and thus large center conductor width) is required for the neutron scattering experiments. For the ferromagnetic resonance spectroscopy, the large center conductor width is disadvantageous because the sensitivity of the CPW-FMR scales as $1/w_{\mathrm{cc}}$.

For our investigation of the dynamic properties of Cu_2OSeO_3 we used two different experimental setups. The first one is the so-called "2-tone" setup shown in Fig. 6.3**(b)**, where the idea is to mimic the pump-probe aspect of the neutron scattering experiment by using a high power, fixed frequency pump (f_{drive}, P_{drive}) and a low power, scanning frequency probe microwave tone (f_{probe}, P_{probe}). To combine f_{probe} and f_{drive} microwave tones, we use a directional coupler (Mini-Circuits ZFBDC16-63HP+). The directional coupler has the property that an incident microwave at the IN port can travel to the OUT port with small losses (typically $-0.5\,\mathrm{dB}$) and vice versa. The same applies for a microwave from REV to FWD. The directional coupler now enables that an incident microwave at port REV is coupled to the OUT port with a typical attenuation of $-20\,\mathrm{dB}$. Therefore, if a microwave is applied at the IN and at the REV port, we get a superposition of the two microwaves at the OUT port but the microwave coming from the REV port is strongly attenuated. At the FWD port, we would get the same but with an attenuated microwave coming from the IN port.

In our setup a frequency source (Rhode&Schwarz SMF100A) capable of generating frequencies of $0.1\,\mathrm{GHz} \leq f_{\mathrm{drive}} \leq 22\,\mathrm{GHz}$ is connected to an amplifier (Mini-Circuits ZHL-5W-422+) which has a maximum output power of 5 W and a bandwidth of $0.5{-}4.2\,\mathrm{GHz}$. The

output of the amplifier is consequently the sinusoidal driving microwave with frequency f_{drive} and power P_{drive} and is connected to the IN port of the directional coupler. The input power at the amplifier is chosen in a way, that the amplifier is operated in saturation at an output power of $P_{\text{drive}} = 5\,\text{W}$.

Additionally, a vector network analyzer (Agilent N5242A PNA-X) is used to measure the complex transmission parameter S_{21} over a broad frequency range. The VNA samples 201 points in a frequency range of $0.1\,\text{GHz} \leq f_{\text{probe}} \leq 3.25\,\text{GHz}$ with an IF bandwidth of 200 Hz and 10 averages of the frequency trace and port power $P_{\text{probe}} = 10\,\text{dBm}$. Port 1 (P1) of the VNA is connected to the REV port of the directional coupler. The microwave of the VNA is consequently coupled to the OUT port with an attenuation of typically $-20\,\text{dB}$, which means that the effective power of the VNA at the OUT port is about $-10\,\text{dBm} \simeq 0.1\,\text{mW}$. Compared to the large power coming form the frequency source ($5\,\text{W} \simeq 37\,\text{dBm}$), the VNA microwave power is about 4 to 5 magnitudes smaller. The VNA probes the dynamic response of the system strongly driven at f_{drive} by measuring the complex transmission parameter S_{21} at scanning frequency f_{probe}. It is important to note, that the frequency source and the vector network analyzer are not phase-locked to each other, which means they both use their own local oscillator as their reference. Therefore the VNA does not "see" the signal coming from the frequency source. Otherwise, in a phase-locked scheme, we would expect a large signal coming from the frequency source in our data. A 30 dB-attenuator is inserted between port 2 of the VNA (P2) and the CPW in order to protect the VNA from too large input powers (not shown in figure).

We performed a second experiment, which is quasi identical to the already discussed VNA-FMR in section 3.1. The only difference is, that we now have an amplifier between port 1 of the VNA and the coplanar waveguide as shown in Fig. 6.3**(c)**. As the power range of the used vector network analyzer is insufficient to saturate the input of the 5 W amplifier used in the 2-tone experiment, we use an additional preamplifier (Kuhne LNA BB 202 A). After these two amplifiers we drive the system with a microwave power P. In contrast to the 2-tone experiment, we drive and probe the system with the same frequency $f_{\text{drive}} = f_{\text{probe}} = f$. We measure the complex transmission parameter S_{21} of the system at frequency f, where we are also driving the system. The port 2 of the VNA is again protected by a 30 dB-attenuator

The coplanar waveguide with the sample (as it was mounted from the neutron scattering experiment) is mounted on a dipstick, which is inserted in the variable temperature inset of the cryostat, where the temperature range was adjusted in the range of $T_{\text{set}} = 51 - 59\,\text{K}$ with a step size of $\Delta T_{\text{set}} = 0.25\,\text{K}$. The magnetic field $\mathbf{H}_0$ is applied in the [110]-direction of the Cu_2OSeO_3 crystal. As these materials are known to have hysteretic properties, the measurement protocol has to be the same for all temperatures. We start each measurement cycle at the lowest temperature, which is stabilized at zero magnetic field ($\mu_0 H_0 = 0\,\text{T}$). After stabilization of the temperature T_{set}, the magnetic field is set to $\mu_0 H_0 = 90\,\text{mT}$. Then the magnetic field is ramped with a constant rate of 2 mT/min to $\mu_0 H_0 = -90\,\text{mT}$, while the VNA continuously measures the S_{21} parameter for the given settings. The field resolution is therefore approximately 0.3 mT. Once the $-90\,\text{mT}$ are reached, the magnetic field is ramped to zero and temperature is raised by 0.25 K. This procedure is repeated

until the critical temperature T_c is reached (for Cu_2OSeO_3: $T_c \approx 59\,K$). Above T_c, only the field polarized mode is observable.

In the next section we want to discuss the data processing and the identification of the magnetic modes present in the skyrmion material.

6.3.1 Processing Raw Data: Derivative Divide vs. Divide Slice

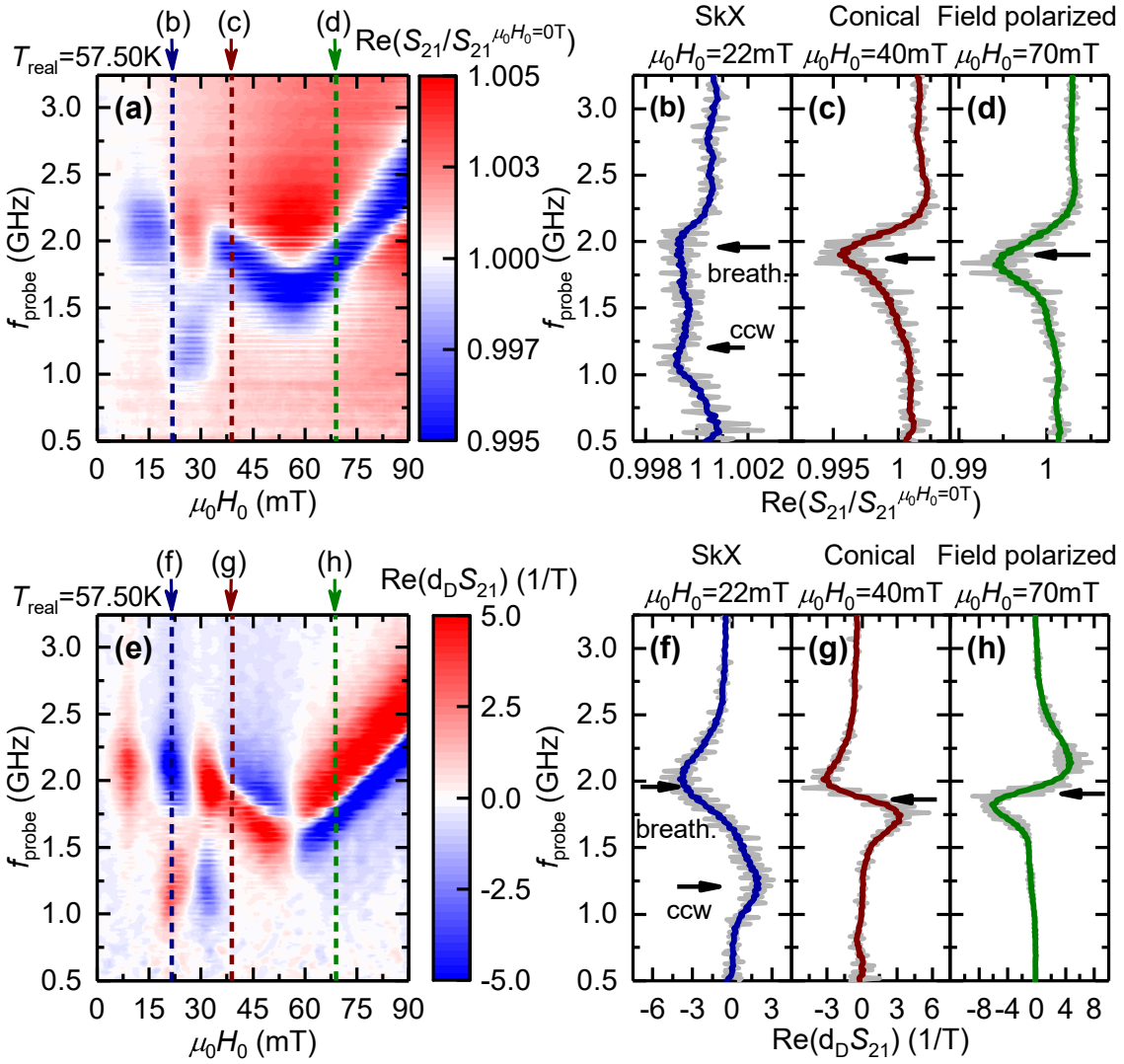

Figure 6.4: Exemplary data of 2-tone experiment for $P_{drive} = 0$ at $T_{real} = 57.50\,K$ with **(a)-(d)** divide slice at $\mu_0 H_0 = 0\,T$ and **(e)-(h)** with derivative divide. The resonance positions of the magnetic modes are indicated with arrows. The solid lines in the field cuts are smoothed data added as a guide to the eye.

As discussed in section 3.3, by measuring in the frequency-swept mode, it is necessary to de-embed the signal coming from the magnetic modes of the system from the microwave transmission background. One way to do so, is by dividing a frequency trace at a certain magnetic field ($S_{21}/S_{21}^{\mu_0 H_0 = 0\,T}$) as depicted in Fig. 6.4**(a)** exemplary at $T_{real} = 57.50\,K$,

referred to as "divide slice" in the following. Another possibility is to use the "derivative divide" method [43] by calculating the symmetric difference quotient of S_{21} (Eq. (3.14)). The resulting plot is shown in Fig. 6.4**(e)**. We now want to identify the different magnetic modes as already discussed in section 6.1.1.

Starting at low magnetic fields ($\mu_0 H_0 \lesssim 10\,\mathrm{mT}$), we would expect to observe the helical mode. Due to the low signal-to-noise ratio, which is because of the large center conductor width w_{cc}, it is barely visible. In the range of $10\,\mathrm{mT} \lesssim \mu_0 H_0 \lesssim 18\,\mathrm{mT}$ the conical mode is recognizable. Then a discontinuity is observed (especially in Fig. 6.4**(a)**), which indicates the phase transition from conical to skyrmion mode. By taking a field cut at $\mu_0 H_0 = 22\,\mathrm{mT}$ as shown in Figs. 6.4**(b)** (divide slice) and 6.4**(f)** (derivative divide), we observe two resonances, attributed to the counter-clockwise (ccw) and the breathing mode. In the divide slice depiction, the resonances are identified as Lorentz peaks in contrast to the derivative divide depiction, where the resonances are identified by dip-peak or peak-dip shapes. The ccw mode has a dip-peak shape, which means that its resonance frequency vs. magnetic field dispersion is positive ($\partial f_{\mathrm{res}}/\partial H_0 > 0$), and the breathing mode has a peak-dip shape, which corresponds to a negative dispersion ($\partial f_{\mathrm{res}}/\partial H_0 < 0$).

By further increasing the magnetic field, the system transitions to the conical phase. In the field cuts at $\mu_0 H_0 = 40\,\mathrm{mT}$ shown in Figs. 6.4**(c)** (divide slice) and 6.4**(g)** (derivative divide) only one resonance is observed. The Q+ and the Q- mode of the conical mode cannot be resolved separately because the modes become degenerate at the phase transition from conical to field polarized phase degenerate. Again, in the divide slice depiction the resonance exhibits a Lorentzian lineform, while in the derivative divide depiction the resonance has a peak-dip shape, which means, that the dispersion is negative. This negative dispersion can also be seen in the colormaps (c.f. Figs. 6.4**(a)** and **(e)**).

For large magnetic fields only the ferrimagnetic mode is present. In the field cut at $\mu_0 H_0 = 70\,\mathrm{mT}$, we see the same signature for the resonance in the divide slice methode (c.f. Fig. 6.4**(d)**) in contrast to the derivative divide depiction, where we observe a dip-peak shape of the ferrimagnetic resonance (c.f. Fig. 6.4**(h)**), which indicates a positive dispersion.

The qualitatively observed frequency vs. magnetic field dispersions are in agreement with the findings of Schwarze *et al.* [87], who used the divide slice method. It is evident from Fig. 6.4, that the signal-to-noise ratio is better in the derivative divide depiction. Additionally, the dispersion of the resonance can be extracted by a single field cut in contrast to the divide slice method. Nevertheless, its easier to extract the phase boundaries in the divide slice depiction, as a discontinuity or a change in the dispersion indicates the boundary. A brief description of the process used to extract a phase diagram from data such as that shown in Fig. 6.4 is given in the next section.

6.3.2 Phase Diagram Extraction

In order to extract the phase diagram, we choose the divide slice depiction because the phase transitions are then indicated by discontinuities or by changes in the dispersion. For a given color map as shown in Fig. 6.5**(a)** the magnetic fields $\mu_0 H_0$, at which the phase transition occurs, are extracted by hand as a function of temperature T_{real} (see section 6.4.1

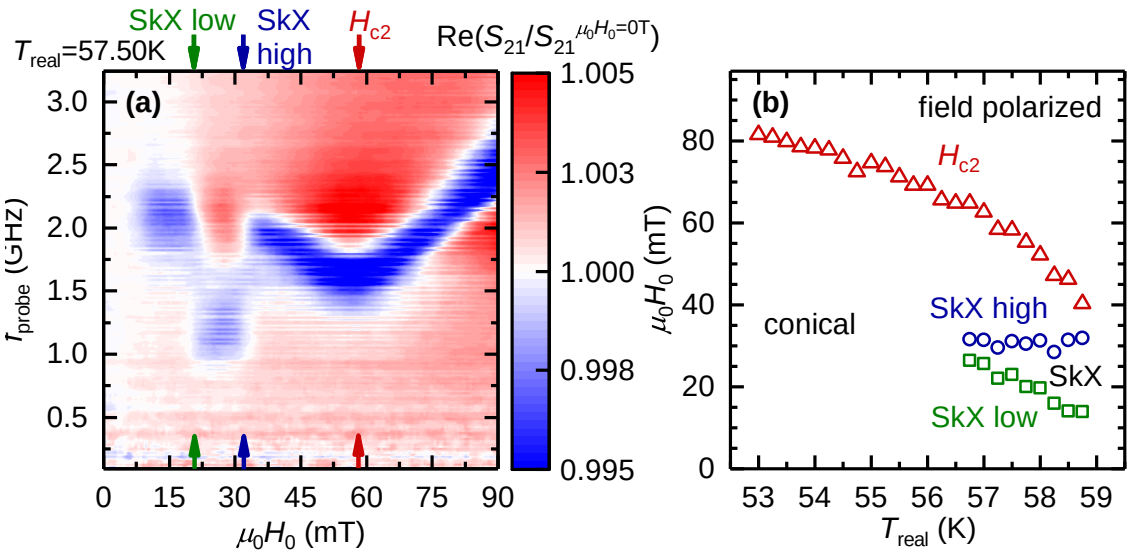

Figure 6.5: **(a)** Exemplary color plot of 2-tone experiment for $P_{\text{drive}} = 0$ at $T_{\text{real}} = 57.50\,\text{K}$ with already marked phase boundaries (vertical lines). **(b)** Complete phase diagram (phase transition at magnetic field $\mu_0 H_0$ for given temperature T_{real}) for no applied microwave. The helical phase is not shown because the signal-to-noise ratio is too low in order to observe the helical mode and extract a phase boundary.

for the determination of T_{real}). Starting at large magnetic field $\mu_0 H_0$, the field polarized mode is observed with its positive frequency vs. magnetic field dispersion. As the conical mode has a negative dispersion, the boundary is indicated by the changing point of the dispersion as indicated by the red vertical line. The critical magnetic field for this transition is called H_{c2}.

For the emergence of skyrmions the system undergoes a phase transition of the first order as the susceptibility is discontinuous at this point. In the color plot this exhibits in a discontinuity. These two transition points are indicated by the blue and green line in Fig. 6.5**(a)**. Due to the poor signal-to-noise ratio the helical mode is not clearly observable and therefore the H_{c1}-phase boundary cannot be determined.

This procedure is repeated for all the measured temperatures T_{real}. The final phase diagram is shown in Fig. 6.5**(b)**. The phase diagram is also used as an indicant to confirm the validity of our performed temperature correction.

6.4 2-Tone Measurement

We have already discussed the method of the 2-tone experiment in section 6.3. It is important to note that the large applied microwave power P_{drive} leads to heating at the sample. Therefore we first want to present our procedure to correct the heating at the sample in order to extract the real sample temperature T_{real}. After that, we discuss the dynamic response of the system by considering the excitation spectra at fixed magnetic field $\mu_0 H_0 = 22\,\text{mT}$ as a function of the microwave frequency f_{drive} at fixed $P_{\text{drive}} = 5\,\text{W}$ and the

applied power P_{drive} at fixed $f_{\mathrm{drive}} = 0.8\,\mathrm{GHz}$. The magnetic field $\mu_0 H_0$ and the considered f_{drive} and P_{drive} are chosen in accordance with the neutron scattering experiment. Finally, we want to briefly discuss the non-linear magnetization dynamics in the conical phase, if the driving frequency f_{drive} matches the resonance frequency of the conical mode.

6.4.1 Temperature Correction and Recovery of Phase Diagram

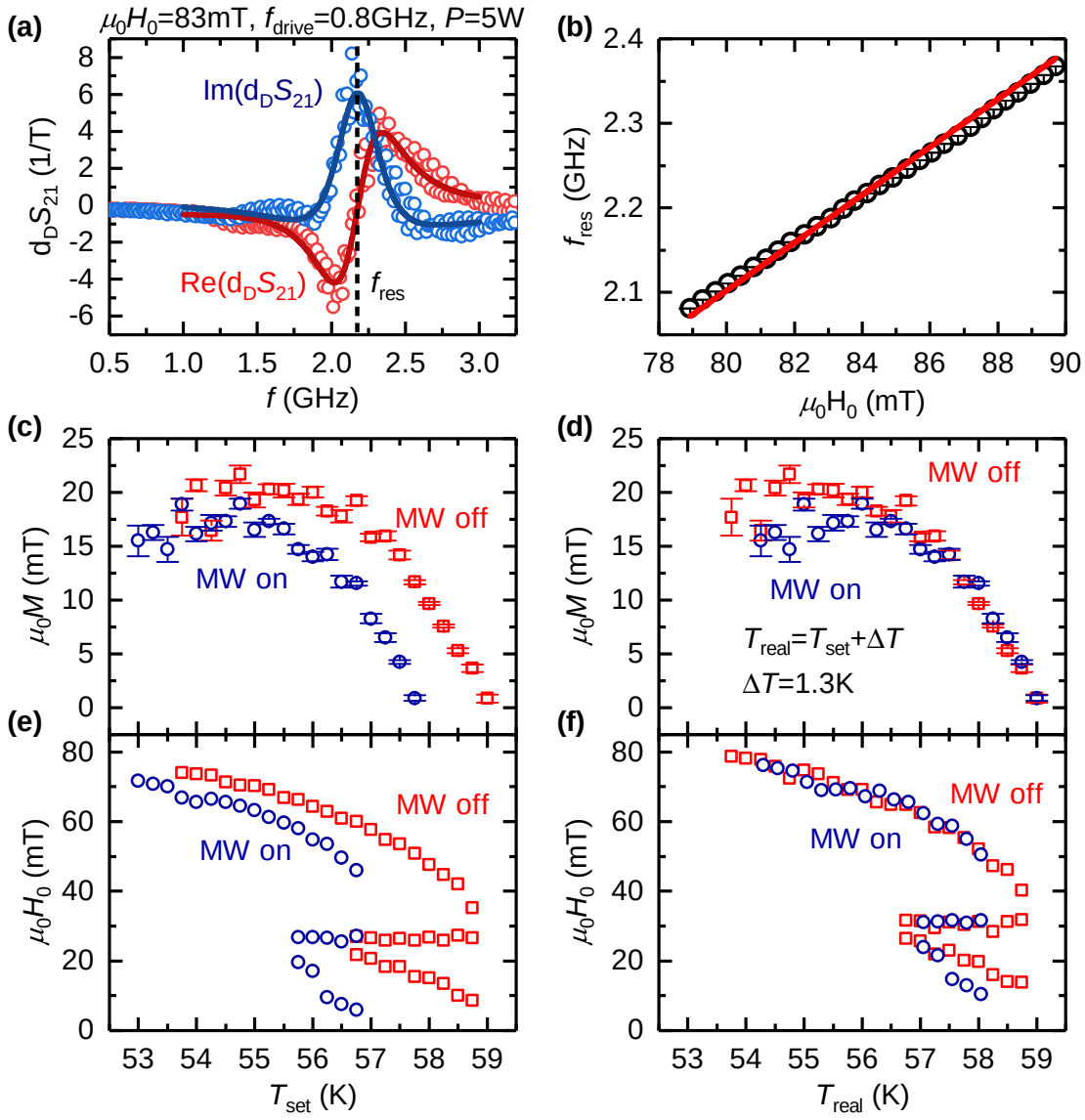

Figure 6.6: Procedure in order to correct the temperature in a 2-tone experiment due to the heating effect at the sample due to the large applied microwave power exemplary done for $f_{\mathrm{drive}} = 0.8\,\mathrm{GHz}$ and $P_{\mathrm{drive}} = 5\,\mathrm{W}$. For more details refer to text.

In contrast to the neutron scattering experiment, where the temperature correction is carried out by analyzing the conical scattering intensity, we perform our temperature correction by analyzing the temperature-dependent resonance frequency of the field-polarized

mode. This temperature correction method shall be exemplarily shown for $f_{\mathrm{drive}} = 0.8\,\mathrm{GHz}$ and $P_{\mathrm{drive}} = 5\,\mathrm{W}$.

First, for each uncorrected spectrum, such as that shown in Fig. 6.4**(e)**, we focus on the data recorded with $H_0 \gg H_{\mathrm{c2}}$, i.e., deep in the field-polarized phase. To this end, we analyze the spectra recorded for the 20 largest values of H_0. For each of these H_0, the real and imaginary part of the complex transmission parameter S_{21} is recorded in the field-polarized phase and fitted simultaneously by using Eq. (3.16) as exemplarily shown in Fig. 6.6**(a)**. From the fits the resonance frequency f_{res} is extracted and plotted as a function of the magnetic field $\mu_0 H_0$ as depicted in Fig. 6.6**(b)**. The resonance condition for the field polarized mode, which is given by Eq. (6.2), is used to fit the data. The demagnetization factors are given by $N_{\mathrm{x}} = 0.2$ and $N_{\mathrm{y}} = N_{\mathrm{z}} = 0.4$, which were calculated by modelling the sample as a general ellipsoid with semiaxes according to the dimensions of the cuboid (c.f. Fig. 6.3**(a)**) with the equations given in [71]. By fixing the Landè-factor to $g = 2.0$, we extract the magnetization $\mu_0 M$.

The extracted magnetization $\mu_0 M$ is plotted as a function of the set temperature T_{set} of the cryostat. As shown in Fig. 6.6**(c)** the data set with "MW on" ($f_{\mathrm{drive}} = 0.8\,\mathrm{GHz}$, $P_{\mathrm{drive}} = 5\,\mathrm{W}$) is shifted to lower temperatures compared to $P_{\mathrm{drive}} = 0$, which in the following is referred to as "MW off". This is a clear evidence for heating at the sample. We assume, the heating effect is negligible for $P_{\mathrm{drive}} = 0\,\mathrm{W}$ ($P_{\mathrm{probe}} \leq 0.1\,\mathrm{mW}$). Hence, for $P_{\mathrm{drive}} = 0$, we use $T_{\mathrm{set}} = T_{\mathrm{real}}$. A rough estimate of the resonant heating effects is given in appendix A.

In order to compensate for the heating, the blue curve in Fig. 6.6**(c)** is rigidly shifted in temperature so the two data sets coincide as shown in Fig. 6.6**(d)**. The real temperature T_{real} is then calculated by $T_{\mathrm{real}} = T_{\mathrm{set}} + \Delta T$. In the given example, the heating effect at the sample can be quantified to $\Delta T = 1.3\,\mathrm{K}$. Note that at the critical temperature $T_{\mathrm{c}} = 59\,\mathrm{K}$ the magnetization vanishes ($M = 0$) as here the thermal energy exceeds the exchange energy and the system becomes paramagnetic.

In order to confirm the validity of our temperature correction the extracted phase diagram is taken into consideration. In Fig. 6.6**(e)**, the phase diagrams with and without applied microwave power are shown as a function of the set temperature T_{set}. Again, a shift in temperature is observed between the two phase diagrams. Shifting the blue phase diagram with the extracted temperature shift ΔT, results in Fig. 6.6**(f)**.

Here, the size of the skyrmion pocket does not change substantially by applying a large microwave power for the given exemplary microwave frequency $f_{\mathrm{drive}} = 0.8\,\mathrm{GHz}$. We also do not observe clear changes of the SkX phase in the phase diagram for all other tested microwave frequencies f_{drive} and powers P_{drive}. This means, that the phase transition into and out of the skyrmion phase itself is not affected by strong microwave driving fields.

Having established that the phase diagram can be recovered independent of applied f_{drive} and P_{drive}, we are now interested in the dynamic response of the system while simultaneously applying strong microwave driving fields, which is discussed in the next section.

6.4.2 Excitation Spectra

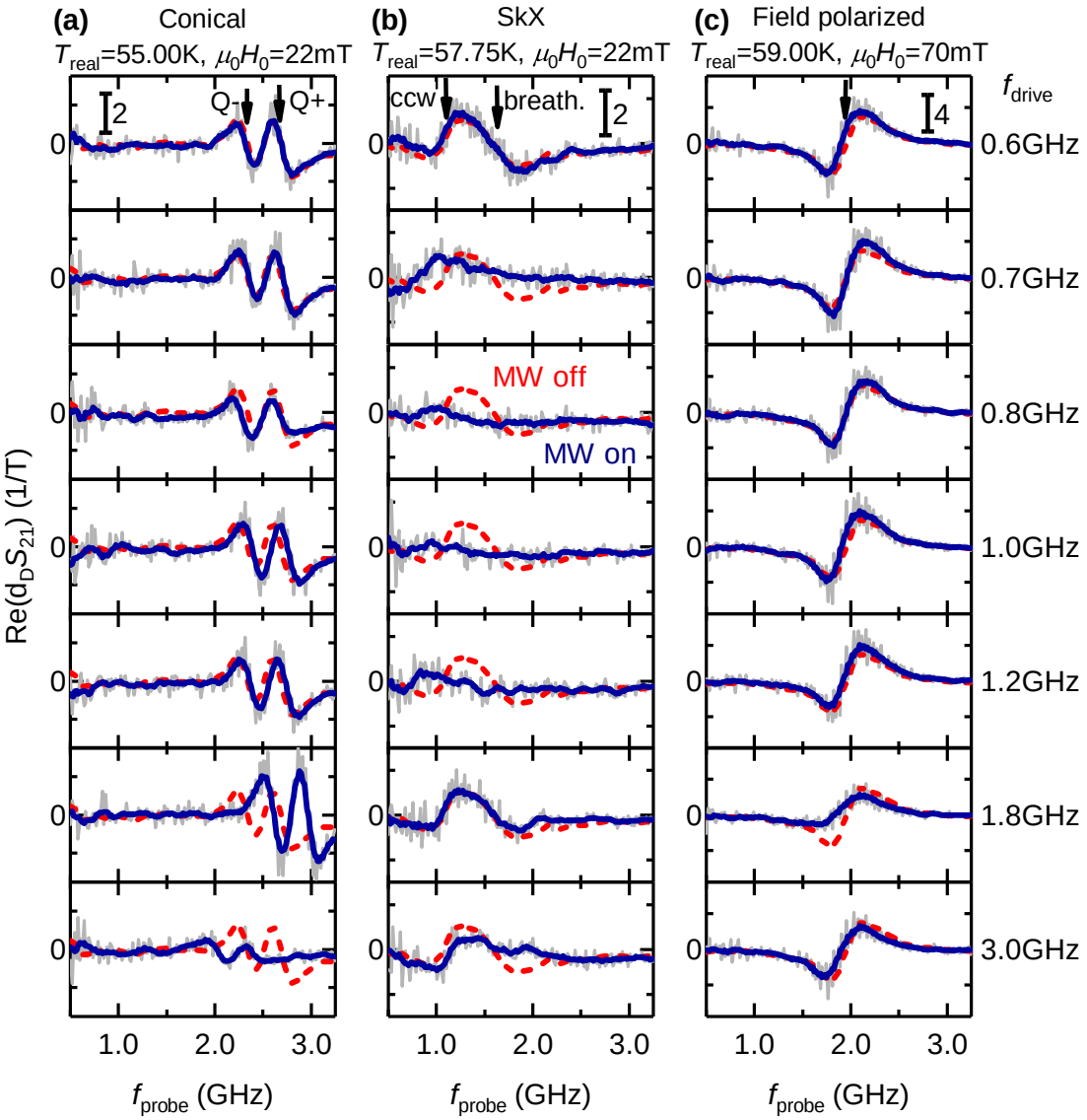

Figure 6.7: Excitation spectra shown for the **(a)** conical, **(b)** skyrmion and **(c)** field-polarized phase for $P_{\mathrm{drive}} = 5\,\mathrm{W}$ as a function of the drive frequency f_{drive}. The blue lines are smoothed curves of the raw data (gray) and are added as a guide to the eye. The excitation spectrum for no microwave power ($P_{\mathrm{drive}} = 0$) is shown as a reference in dashed red. The resonance positions of the magnetic modes for $P_{\mathrm{drive}} = 0$ are indicated with arrows. The y-axis scale is indicated by the black bar and applies to each column.

We have seen, that the phase diagrams extracted in the previous section are unchanged in the presence of a strong microwave excitation. On first sight, this seems to be in contrast to the neutron scattering data discussed in section 6.2.1, where the loss of the skyrmion signal is observable for the very same combination of P_{drive} and f_{drive} that does not lead to a modification of the phase diagram (compare Fig. 6.6**(f)**). In this section we now focus on the dynamic response of the system.

To this end, we consider frequency traces recorded at fixed magnetic field $\mu_0 H_0$. First, we discuss the excitation spectra at fixed $P_{\text{drive}} = 5\,\text{W}$. For all spectra, we employ the temperature correction scheme discussed in the previous section. Starting in the conical phase at $T_{\text{real}} = 55.00\,\text{K}$ and $\mu_0 H_0 = 22\,\text{mT}$ as shown in Fig. 6.7**(a)** we observe two resonances attributed to the Q+ and the Q- mode of the conical spiral, which are non-degenerate for the given parameters. By comparing the spectra with the reference measurement, where no microwave power is applied ($P_{\text{drive}} = 0$, MW off) and which is shown as a dashed red curve in each panel, the curves coincide for the microwave frequencies in the range $0.6\,\text{GHz} \leq f_{\text{drive}} \leq 1.2\,\text{GHz}$. At $f_{\text{drive}} = 1.8\,\text{GHz}$ the conical resonances are shifted to higher frequencies and the amplitude is enhanced, while at $f_{\text{drive}} = 3.0\,\text{GHz}$, the resonances are shifted to lower frequencies and their amplitude is reduced. This behaviour is compatible with an avoided crossing of the conical resonance frequencies with f_{drive}. Note that the observed behaviour is in particular, not compatible with a resonant heating effect, as this would always lead to a decrease of the resonance frequency. This behaviour is subject to further investigation and will be briefly discussed in section 6.4.3.

Next we consider the excitation spectra deep in the skyrmion phase ($T_{\text{real}} = 57.75\,\text{K}$, $\mu_0 H_0 = 22\,\text{mT}$), which are depicted in Fig. 6.7**(b)**. With $f_{\text{drive}} = 0.6\,\text{GHz}$ and $P_{\text{drive}} = 5\,\text{W}$ the excitation spectrum coincides closely with the reference measurement obtained for $P_{\text{drive}} = 0$. At $f_{\text{drive}} = 0.7\,\text{GHz}$ the amplitude of the SkX modes become smaller and in the range $0.8\,\text{GHz} \leq f_{\text{drive}} \leq 1.0\,\text{GHz}$ no signature of the skyrmion modes is observed. The amplitudes of the SkX resonances get larger at $f_{\text{drive}} = 1.2\,\text{GHz}$ until they completely recover to their initial value for $1.8\,\text{GHz} \leq f_{\text{drive}} \leq 3.0\,\text{GHz}$. For $0.8\,\text{GHz} \leq f_{\text{drive}} \leq 1.0\,\text{GHz}$ approximately equals the resonance frequency of the counterclockwise mode (ccw), which leads to the conclusion that by strongly driving the ccw mode, the dynamic response of the skyrmions can be suppressed. This is in accordance with the theoretical description of Mochizuki, including the required red-shift of the driving frequency with respect to the ccw mode to drive the system efficiently.

Note that the data in Fig. 6.7**(b)** are not compatible with a resonant heating effect. The spectral weight of the breathing mode is larger than of the ccw mode. However, driving the system at the breathing mode resonance ($f \cong 1.8\,\text{GHz}$) does not suppress the resonances, while driving the system at the ccw resonance ($f \cong 1.2\,\text{GHz}$) does. The loss of the dynamic response of the system implies, that we are driving the system outside of the linear response regime. In the nonlinear regime, the superposition principle does not apply anymore and therefore the excitations by the driving and probing microwave do not superimpose. If the superposition principle was still valid, we would expect to see the signature of the skyrmion modes independent of P_{drive} and f_{drive}.

In the field polarized phase ($T_{\text{real}} = 59.00\,\text{K}$, $\mu_0 H_0 = 70\,\text{mT}$) shown in Fig. 6.7**(c)** the excitation spectra remain mostly unchanged when changing the microwave frequency f_{drive}. Only at $f_{\text{drive}} = 1.8\,\text{GHz}$, which coincides with the ferrimagnetic resonance, the line becomes broader in accordance with power-broadening of the curve.

We have seen that by setting the driving frequency f_{drive} close to the resonance frequency of the counterclockwise mode, we can suppress the dynamic response of the system. We now investigate data obtained by changing the applied power P_{drive} for a fixed microwave

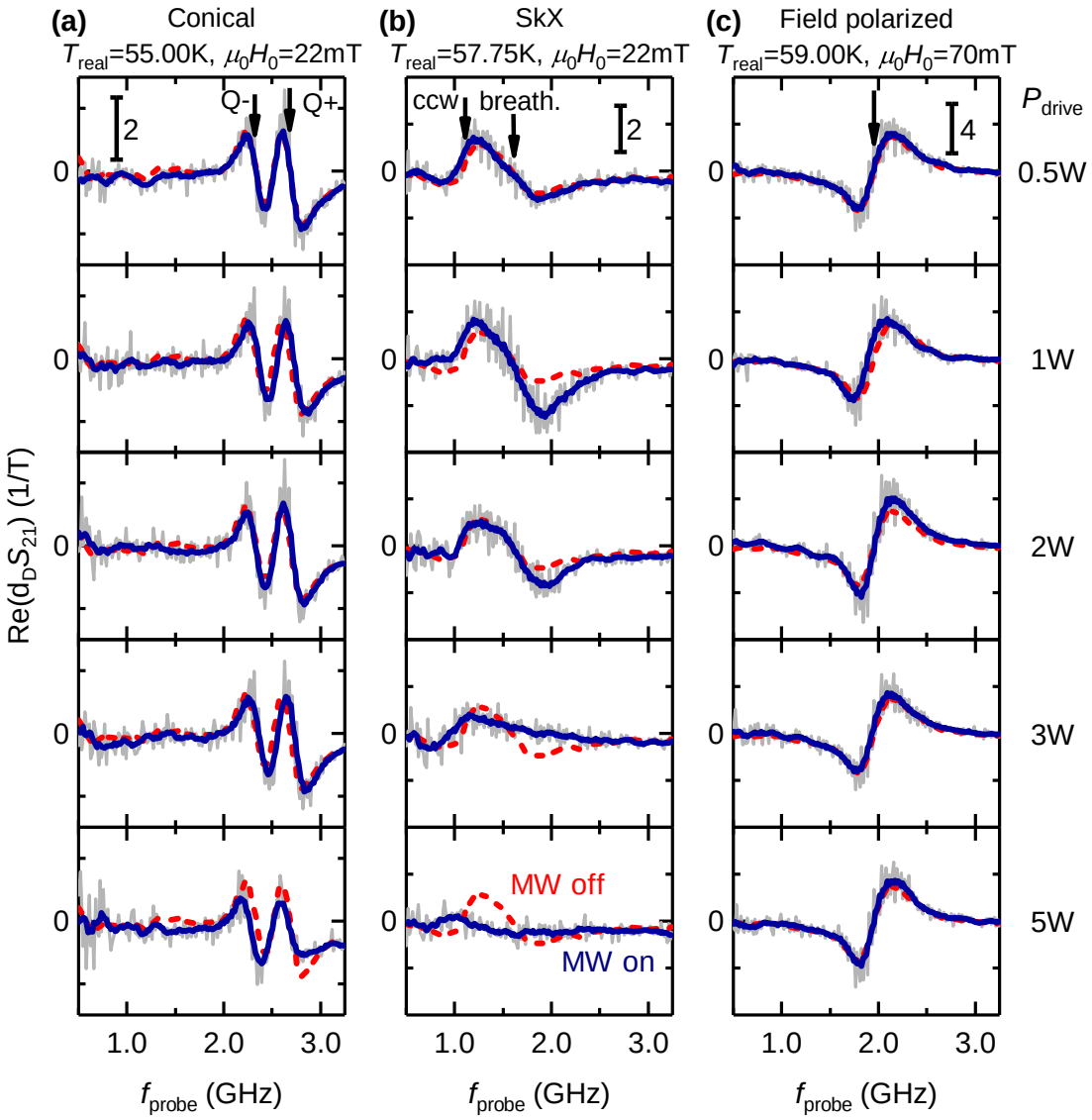

Figure 6.8: Excitation spectra shown for the **(a)** conical, **(b)** skyrmion and **(c)** field-polarized phase for $f_{\mathrm{drive}} = 0.8\,\mathrm{GHz}$ as a function of the microwave power P_{drive}. The blue lines are smoothed curves of the raw data (gray) and are added as a guide to the eye. he excitation spectrum for no microwave power ($P_{\mathrm{drive}} = 0$) is shown as a reference in dashed red. The resonance positions of the magnetic modes for $P_{\mathrm{drive}} = 0$ are indicated with arrows. The y-axis scale is indicated by the black bar and applies to each column.

frequency of $f_{\mathrm{drive}} = 0.8\,\mathrm{GHz}$. The results obtained by the 2-tone experiment are shown in Fig. 6.8.

Starting again with the conical mode shown in Fig. 6.8**(a)** no change of the Q+ and Q- mode is observed by changing the power P_{drive}. In the skyrmion mode depicted in Fig. 6.8**(b)** the curve remains unchanged for low power $P_{\mathrm{drive}} = 0.5\,\mathrm{W}$. At $P_{\mathrm{drive}} = 1\,\mathrm{W}$ the amplitude of the SkX resonances is enhanced but at $P_{\mathrm{drive}} = 2\,\mathrm{W}$ the magnitude decreases until it effectively vanishes at $P_{\mathrm{drive}} = 5\,\mathrm{W}$. The decrease of the amplitude is

quite continuous and no real threshold can be determined. In the field polarized mode (Fig. 6.8**(c)**), the resonance does not show any response to changing the power in the range of $0.5\,\mathrm{W} \leq P_{\mathrm{drive}} \leq 5\,\mathrm{W}$.

In conclusion, we observe the suppression of the dynamic response of the skyrmion resonance by applying a large microwave power P_{drive} at a microwave frequency f_{drive} close to the resonance frequency of the counterclockwise mode. A threshold power could however not be extracted with the data at hand. The other magnetic modes (conical, field polarized) remain mostly unaffected by the large microwave power.

6.4.3 Nonlinear Magnetization Dynamics in the Conical Phase

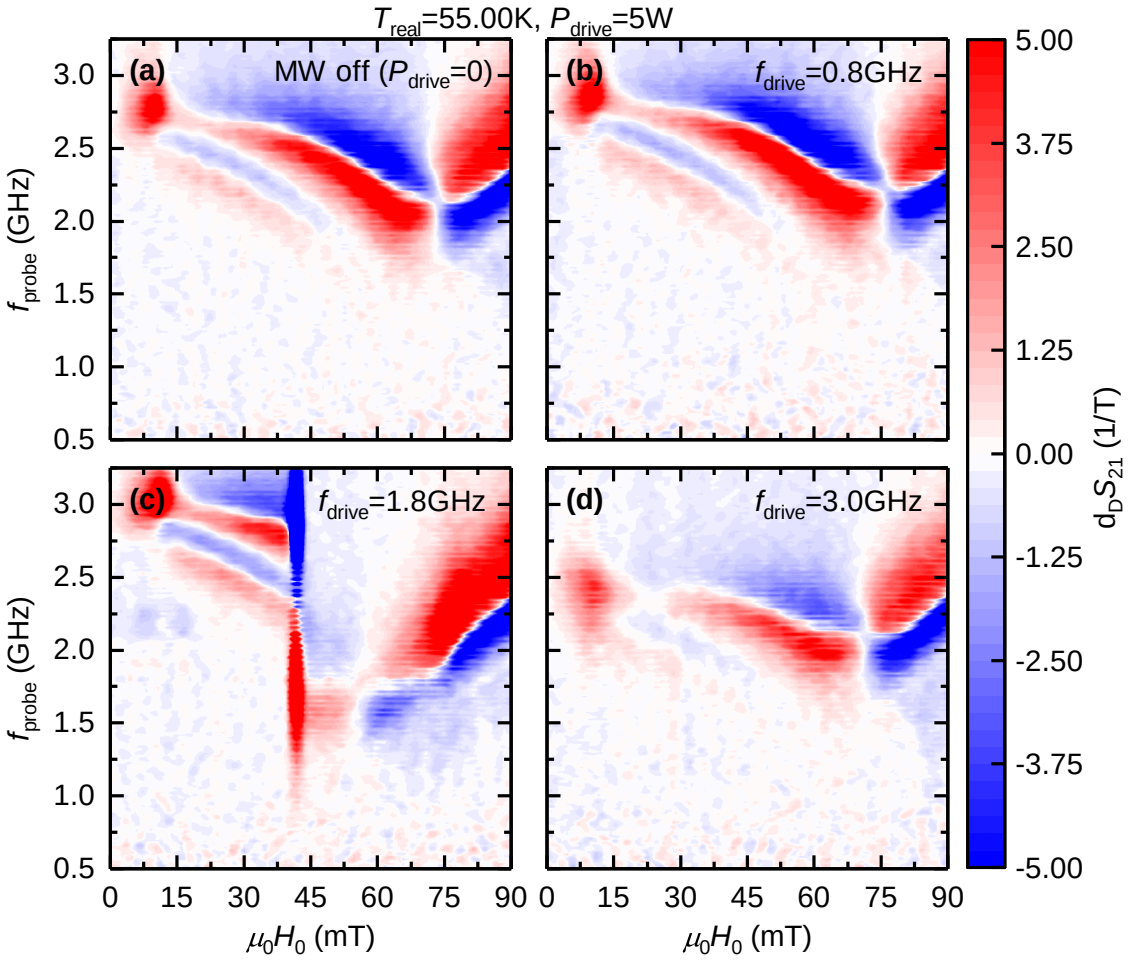

Figure 6.9: Exemplary color plots in derivative divide depiction for $T_{\mathrm{real}} = 55.00\,\mathrm{K}$ and $P_{\mathrm{drive}} = 5\,\mathrm{W}$ for different driving frequencies f_{drive} to illustrate the nonlinear magnetization dynamics in the conical phase. The situation for $P_{\mathrm{drive}} = 0$ is shown in **(a)** as a reference.

As already briefly mentioned, if the driving frequency f_{drive} matches the resonance frequency of the conical mode a new phenomenon is observed. In order to illustrate it, we consider the four color plots shown in Fig. 6.9. If the driving frequency f_{drive} is below the resonance frequency of the conical mode (e.g. $f_{\mathrm{drive}} = 0.8\,\mathrm{GHz}$ in Fig. 6.9**(b)**),

qualitatively no difference is observed compared to the no microwave power case $P_{\mathrm{drive}} = 0$ (c.f. Fig. 6.9**(a)**).

For $f_{\mathrm{drive}} = 1.8\,\mathrm{GHz}$ the situation changes as here the conical mode is degenerate with the driving frequency (Fig. 6.9**(c)**). Two features are observed: First a large "resonance" in the conical mode is observed, which leads to a "jump" of the conical resonance frequency vs. field dispersion. As the chosen depiction is derivative divide, the discontinuity is shown as peak (derivative of step function). This might indicate a phase transition of the first order due to the discontinuity of the susceptibility[1]. The second peculiarity is, that the H_{c2}-transition seems to be shifted to lower magnetic fields. Nevertheless, it is interesting to note that the field polarized mode itself is not influenced by the external driving frequency. At $f_{\mathrm{drive}} = 3.0\,\mathrm{GHz}$ (Fig. 6.9**(d)**), far away from the conical resonance frequency, the situation is again unchanged compared to no microwave power. Currently, this phenomenon is not yet understood and is subject to further investigation.

6.5 Broadband Ferromagnetic Resonance (1-Tone Measurement)

In the previous section, the suppression of the skyrmion resonance was observed by applying a large power P at a certain microwave frequency f_{drive} using a 2-tone setup. Now we switch to a broadband ferromagnetic resonance setup (bFMR) as shown in Fig. 6.3**(c)**. The idea is now to perform a control experiment, where the driving and the probing microwave are the same and where we would expect to see no change in the excitation spectra as the applied power always has to be absorbed by the sample when driving spin dynamics.

In the next section, first the performed temperature correction for the bFMR experiment is presented. Afterwards the gained experimental results regarding the dynamical response (excitation spectra) and the phase diagram are discussed.

6.5.1 Temperature Correction

In section 6.4.1 we have already presented the temperature correction for the 2-tone setup. For the bFMR measurement this procedure remains basically the same besides one aspect: The system is now driven with a broad range of frequencies $f_{\mathrm{drive}} = f$ instead of one frequency f_{drive}. Therefore the effect of heating is now dependent on the spectral weight of the present magnetic modes, which decreases the closer the temperature is to the critical temperature. A rough estimate of the resonant heating effects is given in appendix A.

Repeating the procedure described in section 6.4.1, we first consider the uncorrected spectrum deep in the field polarized mode ($H_0 \gg H_{\mathrm{c2}}$) and analyze the spectra recorded for the 20 largest values of H_0. For each H_0 the real and imaginary part of S_{21} is recorded in the field-polarized mode and fitted simultaneously. The extracted resonance frequency f_{res} is plotted as a function of the magnetic field H_0. From the resonance condition of the field-polarized mode (c.f. Eq. (6.2)) the magnetization M is extracted. The fitted magnetizations M is shown in Fig. 6.10**(a)** as a function of T_{set}. As a reference the 2-tone

[1] From private communications with Achim Rosch (University of Cologne).

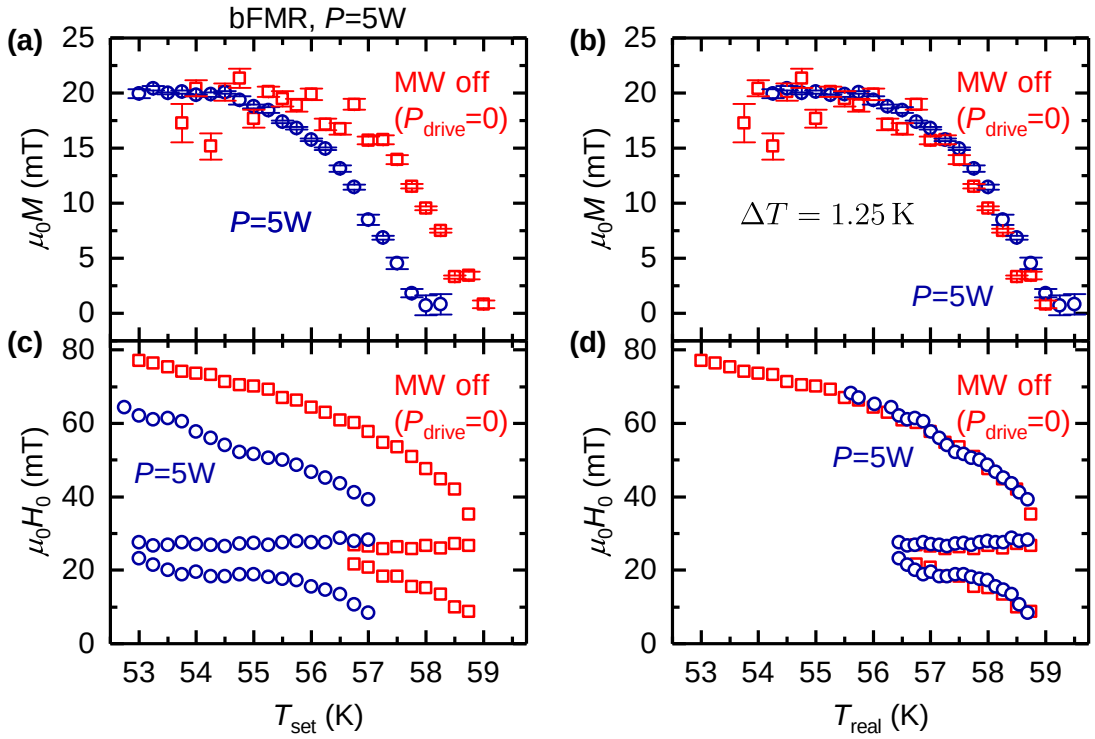

Figure 6.10: Procedure in order to correct the temperature in a bFMR experiment due to the heating effect at the sample in the presence of a large applied microwave power exemplary done for $P = 5\,\mathrm{W}$. For more details refer to text.

measurement with $P_{\mathrm{drive}} = 0$ is used (c.f. Fig. 6.6). In order to compensate for the heating, the blue curve is shifted rigidly to the reference curve (red) as shown in Fig. 6.10**(b)** and the temperature shift ΔT is extracted.

By extracting the phase diagram as described in section 6.3.2 and by comparing it with the reference measurement (both plotted vs. T_{set} in Fig. 6.10**(c)**), a large deviation is observed. Note that a rigid shift of the $P = 5\,\mathrm{W}$ dataset (as done in Fig. 6.6) cannot be used here to match the phase diagrams. This is particularly obvious from the seemingly much broader SkX phase with $P = 5\,\mathrm{W}$. We attribute this to the already mentioned dynamic heating depending on the spectral weight of the present magnetic modes at each temperature. In particular, because the magnetization M increases when decreasing the temperature T (see Fig. 6.10**(b)**), the spectral weight becomes larger for lowering T. Therefore, we separate the heating effect in a static and a temperature-dependent contribution. The static contribution is already determined by ΔT. The temperature-dependent contribution is defined from the phase diagram. We use the equation $T_{\mathrm{real}} = T_{\mathrm{set}} + \Delta T + k \cdot (58\,\mathrm{K} - T_{\mathrm{set}})$, where k is a scaling factor and is determined from the phase diagram. This equation has been derived phenomenologically. By using $k = 0.44$ the agreement with the reference is adequate (c.f. Fig. 6.10**(d)**).

After acquiring the correct temperature T_{real}, we are now interested in the excitation

spectra in the skyrmion phase and the phase diagram for various microwave powers P. These are discussed in the following section.

6.5.2 Excitation Spectra

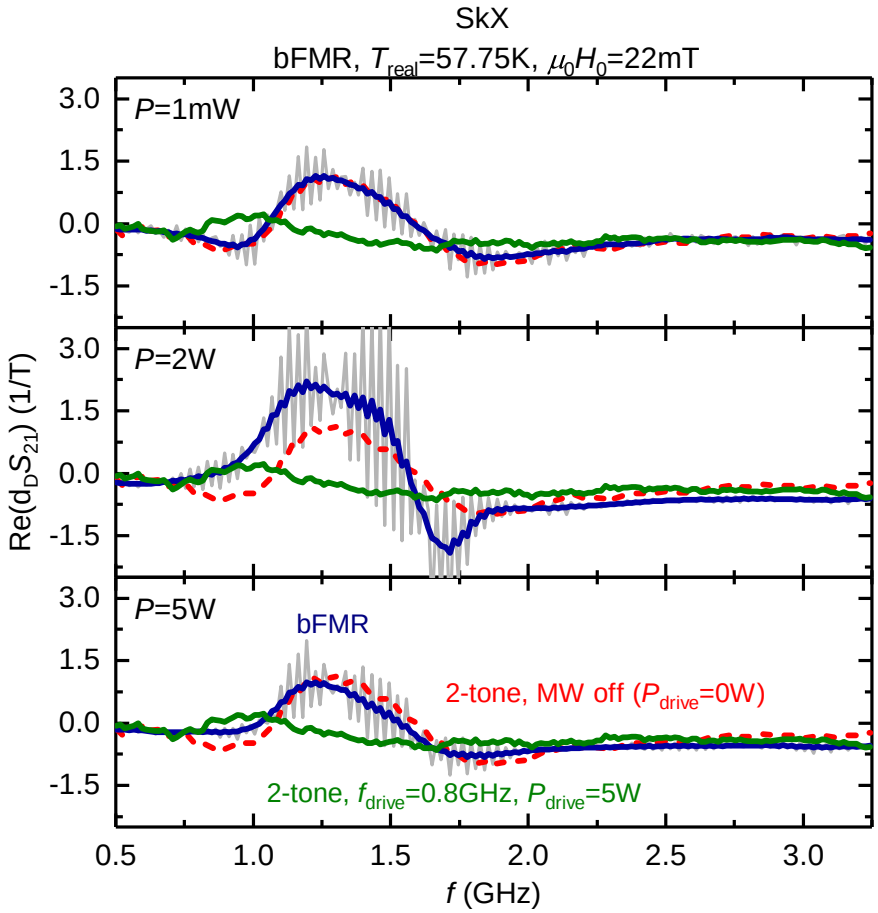

Figure 6.11: Excitation spectra in the skyrmion phase for varying microwave powers P. The low power bFMR ($P = 0.1\,\mathrm{mW}$) (dashed red) and the 2-tone excitation spectrum (green), where "melting" is observed ($f_{\mathrm{drive}} = 0.8\,\mathrm{GHz}$, $P = 5\,\mathrm{W}$), are shown as a reference.

After the temperature has been corrected in the previous section, we first want to compare the excitation spectra in the skyrmion phase for various microwave powers P. In the excitation spectra in Fig. 6.11 the same reference as in the 2-tone measurement ($P_{\mathrm{drive}} = 0$) and the measurement, where the skyrmion signal is strongly suppressed ($f_{\mathrm{drive}} = 0.8\,\mathrm{GHz}$, $P_{\mathrm{drive}} = 5\,\mathrm{W}$), are added in order to compare the magnitudes.

At $P = 1\,\mathrm{mW}$ the curves coincide and the skyrmion modes are not affected. This indicates, that the directional coupler in the 2-tone experiment does not affect the measurement result. With a power level of $P = 2\,\mathrm{W}$ the amplitude of the skyrmion resonances become larger, which is also observed in the 2-tone experiment (c.f. Fig. 6.8**(b)**). Qualitatively the form of the skyrmion resonance is unchanged and both modes can be observed. By further increasing the power to $P = 5\,\mathrm{W}$ the amplitude and noise figure are again comparable

to the lower power case as especially the second amplifier is operated in saturation. The excitation spectrum remains again unchanged.

This is something expected, as in a ferromagnetic resonance measurement the energy provided by the vector network analyzer has to be absorbed in the case of resonance. Therefore some resonant absorption of microwave power has to be observable independent of the input power P. This is in contrast to the 2-tone spectroscopy, where almost no microwave absorption at f_{probe} takes place in Fig. 6.11.

In conclusion, there is no significant change in the excitation spectra compared with the low power data. Therefore, this control experiment confirms the validity of the gained data in the 2-tone experiment, as we observe all skyrmion modes even with large driving powers with the bFMR setup.

6.6 Summary

In this chapter, we investigated the magnetization dynamics of a Cu_2OSeO_3 crystal, where we were especially interested in the dynamics in the skyrmion phase at large microwave power. We therefore used two different experimental setups: 2-tone and broadband FMR setup.

First, in the 2-tone experiment a microwave source was connected to an amplifier, which is capable of providing microwave powers up to 5 W. Additionally, a vector network analyzer was used to measure the complex transmission parameter S_{21} in the frequency range of 0.1 GHz to 3.25 GHz. The small microwave signal coming from the VNA was then superimposed via a directional coupler to the strong signal of the frequency source. The magnetization dynamics of the Cu_2OSeO_3 crystal, which was placed on a coplanar waveguide, was therefore driven by a high power microwave at a fixed frequency f_{drive} coming from the frequency source and probed with small, varying microwave frequency from the VNA.

Because of sample heating due to the large power, we performed a temperature correction. The resulting phase diagrams did not depend on the microwave power P_{drive} or driving frequency f_{drive}. Additionally, the advantages of the derivative divide method compared to the divide slice depiction were shown, as derivative divide allows to determine the sign of the resonance frequency vs. magnetic field dispersion in a single field cut.

In the 2-tone excitation spectra we demonstrated suppression of the skyrmion resonance signature by using $0.7\,\mathrm{GHz} \leq f_{\mathrm{drive}} \leq 1.0\,\mathrm{GHz}$ and $P_{\mathrm{drive}} = 5\,\mathrm{W}$. By choosing a frequency of $f_{\mathrm{drive}} = 0.6\,\mathrm{GHz}$ the excitation spectrum coincides with the reference measurement at low power and both skyrmion modes were observed (counterclockwise and breathing mode). At larger frequencies ($1.2\,\mathrm{GHz} \leq f_{\mathrm{drive}} \leq 3.0\,\mathrm{GHz}$) the skyrmion resonances return to their original magnitude. This indicates that strong driving of the counterclockwise mode with resonance frequency $f_{\mathrm{res}} \simeq 1.2\,\mathrm{GHz}$ is responsible for the suppression of the SkX signal. We however were not able to determine wether this effect possesses a clear threshold behaviour. This will remain subject of further studies.

In a second experiment, we performed a VNA-FMR measurement with an amplifier. The driving and probing microwave were provided by the VNA and hence at the same frequency.

Here we did not observe any changes in the excitation spectra. This was expected in a FMR measurement since the provided energy has to be absorbed when driving a magnetic resonance.

In conclusion, we have seen that we can suppress the dynamic response of the system in a 2-tone measurement. We attribute that to the observation of nonlinear skyrmion dynamics, where the superposition principle is not applicable anymore. In the neutron scattering experiment performed by F. Haslbeck, the signal of the sixfold skyrmion lattice was suppressed under identical conditions, which means that the long-range ordering of the lattice is not present anymore. Therefore the prediction of the "melting" of the skyrmion lattice by Mochizuki [15] could be observed in neutron scattering and in a 2-tone FMR experiment. Further experiments and corresponding theoretical efforts, are required to determine the microscopic processes involved in the "melting" process. We however note that our data represent the first step towards studying nonlinear spin dynamics in skyrmion systems.

Chapter 7

Summary and outlook

In this thesis, the magnetization dynamics in different magnetic material systems at room- and cryogenic temperatures have been investigated. For this purpose, a ferromagnetic resonance technique using a coplanar waveguide and a vector network analyzer (VNA) has been used. In particular, the spin-orbit torques in a normal metal/ferromagnet bilayer system, where the ferromagnet remained always the same (CoFeB) but the normal metals were varied between compositions of TaAu, W and AuPt, have been quantified. The magnetization dynamics in the compensating ferrimagnet gadolinium iron garnet have been investigated, with the focus on the ferrimagnetic and antiferromagnetic resonance and their coupling. Finally, skyrmion dynamics in the insulating chiral magnet Cu_2OSeO_3 have been probed with large microwave power, where a "melting" of the skyrmion lattice could be observed. In the following, we summarize the main results of this thesis.

Summary

Spin-Orbit Torques in Ferromagnet/Normal Metal Bilayers In chapter 4, we presented an inductive measurement technique that allows us to quantify the spin-orbit torques in normal metal/ferromagnet bilayers. We used a vector network analyzer ferromagnetic resonance setup at room-temperature and placed the bilayers flip-chip style onto a coplanar wavguide. The waveguide was used as an excitation as well as a detection transducer, which picks up every source of AC magnetic flux. As shown by Berger *et al.* [41], we have to distinguish between four different flux sources: dipolar contribution due to the precessing magnetization in the ferromagnet, magnetic flux due to currents induced in the normal metal by Faraday's law and magnetic flux due to currents driven by the inverse field- and damping-like spin-orbit torques, which are 90° phase shifted to each other. Due to the phase-sensitive measurement using a VNA in the frequency range from 5 GHz to 40 GHz, it was possible to distinguish these contributions by quantitative evaluation of the FMR signal alone. In particular, our technique does not require any patterning of the samples.

The TaAu/CoFeB samples showed the smallest magnitude of the spin-orbit torque conductivities. From the odd contribution of the total spin-orbit conductivities, we were able to calculate the spin Hall angle θ_{SH} as a function of the TaAu composition. As part of the collaboration with the group of Markus Meinert (University of Bielefeld), who performed harmonic Hall measurements, and the group of Tobias Kampfrath (Fritz-Haber-Intitut, Berlin), who conducted THz emission measurements, it was possible to compare the gained spin Hall angles from these different techniques. We found good quantitative agreement

of the spin Hall angles obtained from the different measurement methods and also with theory, provided by Sebastian Wimmer from the group of Hubert Ebert (LMU).

In the AuPt/CoFeB sample series, we observed a maximum in the spin Hall angle $\theta_{\mathrm{SH}} \approx 0.20$ at a gold content of about 33%. This spin Hall angle is about two times larger than that of pure platinum, which is known to have one of the largest spin Hall angles. Our data are in excellent agreement with THz emission experiments and theory [63]. Additionally, we were able to observe a correlation between the Gilbert damping parameter α_{G} and the odd spin-orbit torque conductivity $\sigma_{\mathrm{o}}^{\mathrm{SOT}}$. Starting at pure platinum the Gilbert damping α_{G} decreased with increasing gold content but $\sigma_{\mathrm{o}}^{\mathrm{SOT}}$ remained more or less unchanged. This indicates, that spin current due to spin pumping decreased with increasing gold content while at the same time the spin Hall effect increased.

In the last sample series, which is W/CoFeB, the level of wolfram-oxidation was varied. We found that the spin-orbit torque conductivities strongly decrease for increasing levels of oxidation. Furthermore, we again observed a correlation between the Gilbert damping parameter α_{G} and the odd spin-orbit torque conductivity $\sigma_{\mathrm{o}}^{\mathrm{SOT}}$. Additionally, at largest the oxygen content of W(O)x we observed a sign change in $\sigma_{\mathrm{o}}^{\mathrm{SOT}}$. This has not been predicted by theory and is not yet understood. Furthermore, we observed a correlation between the Landè-factor g and the even spin-orbit torque conductivity $\sigma_{\mathrm{e}}^{\mathrm{SOT}}$, which is related to the Faraday effect and the Rashba-Edelstein effect. This correlation indicates that the even SOT might be mediated by a spin current due to spin pumping and the imaginary part of the spin mixing conductance $\mathrm{Im}(G_{\uparrow\downarrow})$. This has been predicted by theory [13] but has not yet been observed in experiment.

(Strongly) Coupled Magnetization Dynamics in the Compensated Ferrimagnet Gadolinium Iron Garnet In chapter 5, we investigated the compensating ferrimagnet gadolinium iron garnet (GdIG), which has the same crystal structure as the well known and widely used yttrium iron garnet (YIG). However, only GdIG exhibits a compensation point ($T_{\mathrm{comp}} = 288\,\mathrm{K}$), where the magnetization of the (three) sublattices cancel each other out. The reason for this behaviour is, that GdIG features a third very temperature-dependent Gd-sublattice in contrast to YIG, where the Y-sublattice has no magnetization according to Nèel-theory [64]. The tuneability of the magnetization of GdIG makes it an ideal testbed to investigate the magnetization dynamics close and far away from the compensation point.

We used a VNA-FMR setup at cryogenic temperatures in the range from 150 K to 300 K and in the frequency range $0.1\,\mathrm{GHz} \leq f \leq 26.5\,\mathrm{GHz}$ to investigate a disk shaped gadolinium iron garnet single crystal. The static magnetic field was applied along the $[1\bar{2}1]$-direction of the crystal. First, we extracted the Landè-factor g and the linewidth $\mu_0\Delta H$ of the ferrimagnetic resonance (FMR) as a function of temperature T. The Landè-factor g diverges to negative infinity at the compensation point T_{comp} when coming from lower temperatures and diverges to positive infinity when coming from higher temperatures. The reason for this behaviour is, that the angular momentum compensation point occurs at a higher temperature than the magnetization compensation point. In the linewidth $\mu_0\Delta H$ an enormous broadening at the compensation point is observed, which is due to the rapid rise of the anisotropy field and probably to the breakdown of the dipolar narrowing [72].

The increase of the linewidth at lower temperatures is attributed to the magnetostatic modes, which are standing spin wave patterns due to the shape of the sample. The observed temperature-dependence of the g-factor and of the linewidth are in accordance with theory.

Close to the compensation point, we were able to observe the antiferromagnetic resonance (AFMR), which shifts to higher frequencies with lower temperature due to the increasing molecular exchange constant. In this temperature range, we additionally observed weak coupling between the AFMR and the FMR when their dispersions intersected. Following the approach of Herskind *et al.* [77], we fitted the broadened linewidth as a function of the frequency splitting with a Lorentzian function in order to extract the coupling strength and the linewidths of the isolated resonant modes.

By applying the magnetic field along the $[\bar{1}01]$-direction a characteristic anti-crossing of the FMR and AFMR was observed. The anti-crossing can be modelled by two harmonic oscillators which are coupled to each other. The coupling strength is given by the minimal frequency splitting, which is at least two times larger than the linewidths of both the FMR and AFMR. This classifies the system to be in the strong coupling regime. The origin of the coupling is still unclear but it might be mediated by dipolar interaction. Due to the limited frequency range of the used VNA ($f \leq 26.5\,\mathrm{GHz}$), the AFMR and consequently the coupling between the AFMR and the FMR could only be studied in a limited temperature range. Therefore, in a next iteration of this experiment a vector network analyzer which is capable of higher frequencies should be used.

Dynamic Skyrmion Melting in Cu_2OSeO_3 In chapter 6, the insulating, chiral magnet Cu_2OSeO_3 was taken into consideration. This material is known to host skyrmions, which are topologically protected spin solitons and form a (skyrmion) lattice with hexagonal symmetry in a narrow range of temperatures and external magnetic fields. This experiment was motivated by the theoretical calculations of M. Mochizuki [15], who predicted a "melting" of the skyrmion lattice by a large microwave power. In small angle neutron scattering experiments (SANS) performed by F. Haslbeck (TUM), the sample was placed on a coplanar waveguide and it was indeed observed that the SANS-intensity of the skyrmions vanishes for a microwave frequency of $f_{\mathrm{drive}} = 0.8\,\mathrm{GHz}$ and a microwave power of $P_{\mathrm{drive}} = 5\,\mathrm{W}$. In these experiments and in all our experiments discussed below, heating effects are corrected and not responsible for the melting of the skyrmion lattice.

In our approach, we used a so-called 2-tone experiment, where a frequency source with an amplifier was used to drive the magnetization of the same Cu_2OSeO_3 crystal. Additionally, the complex transmission parameter S_{21} is measured by a vector network analyzer over a frequency range of $0.1\,\mathrm{GHz} \leq f_{\mathrm{probe}} \leq 3.25\,\mathrm{GHz}$. To this end, the probing microwave tone was superimposed with the microwave driving tone using a directional coupler. The frequency source and the VNA were not phase-locked with each other. By comparing the excitation spectra in the skyrmion phase at a fixed magnetic field of 22 mT for various microwave frequencies f_{drive}, we find that the skyrmion resonance signal at f_{probe} is strongly suppressed whenever f_{drive} matches the counterclockwise skyrmion resonance mode. The skyrmion resonance at f_{probe} is not affected if f_{drive} is detuned from the skyrmion resonance.

We furthermore set the microwave frequency fixed to $f_{\mathrm{drive}} = 0.8\,\mathrm{GHz}$ and varied

the power P_{drive}. In accordance with the neutron scattering experiment, we observed a continuous decrease of the amplitude of the skyrmion resonance. As a control experiment, we additionally performed a standard VNA-FMR experiment with an amplifier, so that the driving and probing frequencies were identical. No change of skyrmion resonance intensity with varying microwave power was found, in accordance with our expectations.

Outlook

The "melting" of the skyrmion lattice is an interesting phenomenon, because the skyrmions can be "destroyed" by microwave power and not by thermal energy. If this phenomenon is fully understood, it can be technologically relevant for example in skyrmion racetrack memories. There already exist theoretical predictions [95, 96] and experimental implementations [97] of a skyrmion racetrack memory. The skyrmions can be transported through the racetrack with electrical currents [83] and are stable due to their particle-like behaviour and their topological protection. The "melting" could then possibly be used to erase the information stored in the skyrmion. Nevertheless, it is inevitable to get a full understanding of the "melting" process as it is currently unclear, what the resulting physical state of the system after the "melting" is and what really mediates the process.

Another not yet understood phenomenon observed during the skyrmion measurements is an additional resonance in the conical phase. As very briefly discussed in sections 6.4.2 and 6.4.3, an avoided crossing of the conical resonance and the microwave frequency is observed for large microwave powers. The conical mode becomes discontinuous at the value of the external magnetic field, where its resonance frequency matches the driving frequency f_{drive}. As suggested by theorists from the University of Cologne (Achim Rosch), this might indicate a phase transition of first order (due to the discontinuity) as the conical mode is hit with a microwave of large power. This behaviour is by no means fully understood and should be further investigated.

The inductive measurement technique that we used in chapter 4 to quantify the field- and damping-like spin-orbit torques, is not limited to only normal metal/ferromagnet bilayers. This method is versatile and can be used for any material systems with either interfacial or even bulk spin-orbit torques [98]. Therefore it would be interesting to study spin-orbit torques in more complicated systems containing the compensating ferrimagnet gadolinium iron garnet, the chiral magnet Cu_2OSeO_3 or any other magnetic material. This would require to fabricate thin films using a sputtering or pulsed laser deposition technique. For gadolinium iron garnet this is already possible but thin films of Cu_2OSeO_3 have not been synthesized so far due to its toxicity. Nevertheless, thin films of Cu_2OSeO_3 would be highly interesting, as it is reported that the skyrmion phase is not limited to a small region close to the critical temperature in thin films (c.f. Fig. 6.5**(b)**), but the skyrmions more or less displace the conical phase completely [99]. We could extract spin-orbit torques at Cu_2OSeO_3/normal metal interfaces by our inductive technique. It would furthermore be interesting to check, if the spin-orbit torques have a microwave power dependence in a 2-tone experiment and if the melting is also observable in thin films.

The quantification of the spin-orbit torques is not limited to VNA-FMR measurements.

It is also possible to quantify spin-orbit torques with an optical setup exploiting the frequency-resolved magneto-optical Kerr effect (MOKE). The phase-resolved dynamic MOKE technique probes the magnetization component perpendicular to the applied driving magnetic field. Consequently, the off-diagonal component of the Polder-susceptibility can be extracted. It should hence be possible to extend our quantitative spin-orbit torque analysis technique to allow for the processing of phase-sensitive frequency-resolved MOKE data. This would allow to study spin-orbit torques in a spatially resolved manner.

Appendix A

Estimation of the Resonant Heating Effect with Large Microwave Power in Cu_2OSeO_3

To give a rough estimate of the resonant heating effects, we assume that the sample absorbs all the microwave power but does not dissipate any energy. The thermal energy Q corresponding to a temperature difference ΔT is related to the mass m and the specific heat capacity c by [100]

$$Q = c\, m\, \Delta T. \tag{A.1}$$

The mass can be calculated by $m = \rho \cdot V$, where $\rho = 5.07 \times 10^6\,\mathrm{g/m^3}$ [101] is the density of Cu_2OSeO_3 and V is the volume calculated from the dimensions given in Fig. 6.3**(a)**. The molar heat capacity is close to the critical temperature approximately $C_\mathrm{M} \simeq 40\,\mathrm{J/(mol\,K)}$ [102] and can be converted to the specific heat capacity $c = C_\mathrm{M}/M_\mathrm{mol}$ using the molar mass of Cu_2OSeO_3 ($M_\mathrm{mol} \simeq 270\,\mathrm{g/mol}$).

Due to the frequency-dependent microwave losses, the applied power of maximally $5\,\mathrm{W} \cong 37\,\mathrm{dBm}$ from the amplifier is attenuated in the cables, in the coplanar waveguide and in the directional coupler (c.f. setups in Fig. 6.3). The losses are roughly $-2.5\,\mathrm{dB}$ which leads to an effective power of $P_\mathrm{eff} \simeq 2.8\,\mathrm{W}$ at the sample.

To obtain the energy which is absorbed on resonance, we consider the excitation spectra in the "divide slice" depiction as shown in Fig. 6.4**(b)-(d)** because it directly gives the relative absorption of the complex transmission parameter S_{21}. As the field-polarized mode has the largest spectral weight, we take exemplary the excitation spectrum in the ferrimagnetic phase shown in Fig. 6.4**(d)**. By considering the depth of the resonance we get an absorption of approximately 1% of the total transmission. As seen from the definition of the transmission parameter $S_{21} = V_2/V_1$ (c.f. Eq. (3.1)), we need to convert to power by $P = I \cdot V = V^2/Z_0$, where $Z_0 = 50\,\Omega$ is the impedance of the microwave system. This results in the absorbed power at resonance described by

$$P_\mathrm{abs} = \mathrm{Re}\left(\frac{S_{21}}{S_{21}^{\mu_0 H_0 = 0\,\mathrm{mT}}}\right)^2\Bigg|_{f_\mathrm{res}} = \frac{P_\mathrm{eff}}{10000} = 280\,\mu\mathrm{W}. \tag{A.2}$$

In the final step, the absorbed power needs to be rewritten into an energy using $P_\mathrm{abs} = Q_\mathrm{abs} \cdot t$, where t is the dwell time on the resonance. This time is approximately $t \simeq 25\,\mathrm{ms}$, which is estimated from the time of the total frequency trace ($\sim 1\,\mathrm{s}$) and the width of the resonance.

Plugging everything into Eq. (A.1), we get a temperature difference for $P_{\text{eff}} = 2.8\,\text{W}$ of

$$\Delta T = \frac{P_{\text{abs}} \cdot t}{c \cdot m} \overset{t=25\,\text{ms}}{\simeq} 9\,\text{mK}. \tag{A.3}$$

This result means, that every time we ramp the frequency through the resonance, the sample gets 9 mK hotter. Importantly, this is an upper limit as we do not consider any heat transfer from the sample to the environment.

For the 1-tone experiment (bFMR) this result is reassuring. For the 2-tone experiment the situation is however more difficult: If the driving frequency f_{drive} matches the resonance frequency of a magnetic mode, we constantly heat the sample and ΔT would become infinite in this approximation. To estimate the heating in the 2-tone experiments, we would need to determine the thermal time constant of the CPW-sample system.

Bibliography

[1] S. Lloyd, *Ultimate physical limits to computation*, Nature **406**, 1047–1054 (1999).

[2] M. N. Baibich, J. M. Broto, A. Fert, F. N. Van Dau, F. Petroff, P. Etienne, G. Creuzet, A. Friederich, and J. Chazelas, *Giant Magnetoresistance of (001)Fe/(001)Cr Magnetic Superlattices*, Physical Review Letters **61**, 2472–2475 (1988).

[3] G. Binasch, P. Grünberg, F. Saurenbach, and W. Zinn, *Enhanced magnetoresistance in layered magnetic structures with antiferromagnetic interlayer exchange*, Physical Review B **39**, 4828–4830 (1989).

[4] A. Fert, *Nobel Lecture: Origin, development, and future of spintronics*, Reviews of Modern Physics **80**, 1517–1530 (2008).

[5] M. Julliere, *Tunneling between ferromagnetic films*, Physics Letters A **54**, 225–226 (1975).

[6] Sining Mao, Yonghua Chen, Feng Liu, Xingfu Chen, Bin Xu, Puling Lu, M. Patwari, Haiwen Xi, Clif Chang, B. Miller, D. Menard, B. Pant, J. Loven, K. Duxstad, Shaoping Li, Zhengyong Zhang, A. Johnston, R. Lamberton, M. Gubbins, T. McLaughlin, J. Gadbois, Juren Ding, B. Cross, Song Xue, and P. Ryan, *Commercial TMR heads for hard disk drives: characterization and extendibility at 300 gbit/in*^{2}, IEEE Transactions on Magnetics **42**, 97–102 (2006).

[7] S. S. P. Parkin, M. Hayashi, and L. Thomas, *Magnetic Domain-Wall Racetrack Memory*, Science **320**, 190–194 (2008).

[8] E. Technologies Inc., *Toggle MRAM Technology* (2015).

[9] K. Ando, S. Fujita, J. Ito, S. Yuasa, Y. Suzuki, Y. Nakatani, T. Miyazaki, and H. Yoda, *Spin-transfer torque magnetoresistive random-access memory technologies for normally off computing (invited)*, Journal of Applied Physics **115**, 172607 (2014).

[10] S. Mühlbauer, B. Binz, F. Jonietz, C. Pfleiderer, A. Rosch, A. Neubauer, R. Georgii, and P. Böni, *Skyrmion Lattice in a Chiral Magnet*, Science **333**, 1381–1381 (2011), arXiv:1006.3973 .

[11] I. M. Miron, K. Garello, G. Gaudin, P.-J. Zermatten, M. V. Costache, S. Auffret, S. Bandiera, B. Rodmacq, A. Schuhl, and P. Gambardella,

Perpendicular switching of a single ferromagnetic layer induced by in-plane current injection, Nature **476**, 189–193 (2011).

[12] S. Sievers, J. Kurda, N. Liebing, F. Hohls, and H. W. Schumacher, *Microwave Interferometry for High Sensitivity VNA-FMR Measurements*, IEEE Transactions on Magnetics **53**, 1–4 (2017).

[13] Y. Tserkovnyak, A. Brataas, and G. E. W. Bauer, *Enhanced Gilbert Damping in Thin Ferromagnetic Films*, Physical Review Letters **88**, 117601 (2002), arXiv:0110247 [cond-mat] .

[14] P. M. Haney, H.-W. Lee, K.-J. Lee, A. Manchon, and M. D. Stiles, *Current induced torques and interfacial spin-orbit coupling: Semiclassical modeling*, Physical Review B **87**, 174411 (2013), arXiv:1301.4513 .

[15] M. Mochizuki, *Spin-Wave Modes and Their Intense Excitation Effects in Skyrmion Crystals*, Physical Review Letters **108**, 017601 (2012), arXiv:1111.5667v1 .

[16] R. Gross and A. Marx, *Festkörperphysik*, 2nd ed. (Walter de GruyterVerlag, 2014) p. 1024.

[17] W. Heisenberg, *Mehrkörperproblem und Resonanz in der Quantenmechanik*, Zeitschrift für Physik **38**, 411–426 (1926).

[18] J. Luttinger and C. Kittel, *A note on the quantum theory of ferromagnetic resonance*, Helv. Phys. Acta **21**, 480 (1948).

[19] N. Bohr, *Über die Serienspektra der Elemente*, Zeitschrift für Physik **2**, 423–469 (1920).

[20] S. Vonsovskii, *Ferromagnetic Resonance* (Pergamon Press, 1964) p. 340.

[21] S. Blundell, *Magnetism in Condensed Matter*, Oxford Master Series in Physics ed. (Oxford University Press, 2000) p. 238.

[22] L. D. Landau and E. Lifshitz, *On the theory of the dispersion of magnetic permeability in ferromagnetic bodies*, Phys. Z. Sowjet. **8**, 153 (1935).

[23] T. Gilbert, *A Phenomenological Theory of Damping in Ferromagnetic Materials*, IEEE Transactions on Magnetics **40**, 3443–3449 (2004).

[24] A. Gurevich and G. Melkov, *Magnetization Oscillations and Waves* (CRC Press, Taylor & Francis Group, 1996) p. 445.

[25] B. Lax and K. Button, *Microwave ferrites and ferrimangetics* (McGraw-Hill, 1962) p. 752.

[26] D. D. Stancil and A. Prabhakar, *Spin Waves*, 1st ed. (Springer US, Boston, MA, 2009) p. 348.

[27] P. D. Louis, *Broadband-Spectroscopy of Magnetic Materials at Low Temperatures*, Master thesis, Technische Universität München (2016).

[28] L. Dreher, M. Weiler, M. Pernpeintner, H. Huebl, R. Gross, M. S. Brandt, and S. T. B. Goennenwein, *Surface acoustic wave driven ferromagnetic resonance in nickel thin films: Theory and experiment*, Physical Review B **86**, 134415 (2012), arXiv:1208.0001 .

[29] J. A. C. Bland and B. Heinrich, *Ultrathin Magnetic Structures III*, 1st ed., edited by J. A. C. Bland and B. Heinrich (Springer-Verlag, Berlin/Heidelberg, 2005) p. 318.

[30] D. Polder, *VIII. On the theory of ferromagnetic resonance*, The London, Edinburgh, and Dublin Philosophical Magazine and Journal of Science **40**, 99–115 (1949).

[31] C. Kittel, *On the Theory of Ferromagnetic Resonance Absorption*, Physical Review **73**, 155–161 (1948).

[32] M. A. W. Schoen, D. Thonig, M. L. Schneider, T. J. Silva, H. T. Nembach, O. Eriksson, O. Karis, and J. M. Shaw, *Ultra-low magnetic damping of a metallic ferromagnet*, Nature Physics **12**, 839–842 (2016), arXiv:1512.03610 .

[33] Y. Y. Zhou, X. Liu, J. K. Furdyna, M. A. Scarpulla, and O. D. Dubon, *Ferromagnetic resonance investigation of magnetic anisotropy in $Ga_{1-x}MnxAs$ synthesized by ion implantation and pulsed laser melting*, Physical Review B **80**, 224403 (2009).

[34] A. B. Kos, T. J. Silva, and P. Kabos, *Pulsed inductive microwave magnetometer*, Review of Scientific Instruments **73**, 3563–3569 (2002).

[35] G. D. Fuchs, J. C. Sankey, V. S. Pribiag, L. Qian, P. M. Braganca, A. G. F. Garcia, E. M. Ryan, Z.-P. Li, O. Ozatay, D. C. Ralph, and R. A. Buhrman, *Spin-torque ferromagnetic resonance measurements of damping in nanomagnets*, Applied Physics Letters **91**, 062507 (2007), arXiv:0703577 [cond-mat] .

[36] S. S. Kalarickal, P. Krivosik, M. Wu, C. E. Patton, M. L. Schneider, P. Kabos, T. J. Silva, and J. P. Nibarger, *Ferromagnetic resonance linewidth in metallic thin films: Comparison of measurement methods*, Journal of Applied Physics **99**, 093909 (2006).

[37] M. Hiebel, *Fundamentals of vector network analysis* (Rohde & Schwarz, 2007) p. 419.

[38] C. Wen, *Coplanar Waveguide: A Surface Strip Transmission Line Suitable for Nonreciprocal Gyromagnetic Device Applications*, IEEE Transactions on Microwave Theory and Techniques **17**, 1087–1090 (1969).

[39] O. Karlqvist, *Calculation of the magnetic field in the ferromagnetic layer of a magnetic drum.* (Elanders boktr., Göteborg; [Stockholm], 1954) pp. 3–27.

[40] T. J. Silva, H. T. Nembach, J. M. Shaw, B. Doyle, K. Oguz, K. O'brien, and M. Doczy, *Characterization of Magnetic Nanostructures for Spin-Torque Memory Applications with Macro- and Micro-Scale Ferromagnetic Resonance*, in *Metrology and Diagnostic Techniques for Nanoelectronics* (CRC Press, Taylor & Francis Group, 2016) Chap. 16, p. 1454.

[41] A. J. Berger, E. R. J. Edwards, H. T. Nembach, J. M. Shaw, A. D. Karenowska, M. Weiler, and T. J. Silva, *Evidence for a common origin of spin-orbit torque and the Dzyaloshinskii-Moriya interaction at a $Ni_{80}Fe_{20}/Pt$ interface*, (2016), arXiv:1611.05798 .

[42] H. T. Nembach, T. J. Silva, J. M. Shaw, M. L. Schneider, M. J. Carey, S. Maat, and J. R. Childress, *Perpendicular ferromagnetic resonance measurements of damping and Landè g-factor in sputtered $(Co_2Mn)_{1-x}Ge_x$ thin films*, Physical Review B **84**, 054424 (2011).

[43] H. Maier-Flaig, S. T. B. Goennenwein, R. Ohshima, M. Shiraishi, R. Gross, H. Huebl, and M. Weiler, *Analysis of broadband ferromagnetic resonance in the frequency domain*, (2017), arXiv:1705.05694 .

[44] H. Haken and H. C. Wolf, *Atom- und Quantenphysik : Einführung in die experimentellen und theoretischen Grundlagen ; mit 32 Tabellen, 177 Aufgaben und vollständigen Lösungen* (Springer, 2004).

[45] J. Sinova, S. O. Valenzuela, J. Wunderlich, C. H. Back, and T. Jungwirth, *Spin Hall effects*, Reviews of Modern Physics **87**, 1213–1260 (2015), arXiv:1411.3249 .

[46] K. Garello, I. M. Miron, C. O. Avci, F. Freimuth, Y. Mokrousov, S. Blügel, S. Auffret, O. Boulle, G. Gaudin, and P. Gambardella, *Symmetry and magnitude of spin–orbit torques in ferromagnetic heterostructures*, Nature Nanotechnology **8**, 587–593 (2013), arXiv:1301.3573 .

[47] S. Maekawa and S. O. Valenzuela, *Spin current* (Oxford University Press, 2012) p. 461.

[48] A. Hoffmann, *Spin Hall Effects in Metals*, IEEE Transactions on Magnetics **49**, 5172–5193 (2013).

[49] Y. A. Bychkov and É. I. Rashba, *Properties of a 2D electron gas with lifted spectral degeneracy*, JETP Letters **39**, 78–81 (1984).

[50] V. Edelstein, *Spin polarization of conduction electrons induced by electric current in two-dimensional asymmetric electron systems*, Solid State Communications **73**, 233–235 (1990).

[51] L. Onsager, *Reciprocal Relations in Irreversible Processes. I.*, Physical Review **37**, 405–426 (1931).

[52] M. Weiler, J. M. Shaw, H. T. Nembach, and T. J. Silva, *Phase-Sensitive Detection of Spin Pumping via the ac Inverse Spin Hall Effect*, Physical Review Letters **113**, 157204 (2014), arXiv:1401.6469 .

[53] A. Brataas, A. D. Kent, and H. Ohno, *Current-induced torques in magnetic materials*, Nature Materials **11**, 372–381 (2012).

[54] E. B. Rosa and U. S. N. B. of Standards, *The self and mutual inductances of linear conductors* (U.S. Dept. of Commerce and Labor, Bureau of Standards, 1908) p. 44.

[55] A. Brataas, Y. V. Nazarov, and G. E. W. Bauer, *Finite-Element Theory of Transport in Ferromagnet–Normal Metal Systems*, Physical Review Letters **84**, 2481–2484 (2000), arXiv:9906065 [cond-mat] .

[56] C. Du, H. Wang, P. C. Hammel, and F. Yang, *$Y_3Fe_5O_{12}$ spin pumping for quantitative understanding of pure spin transport and spin Hall effect in a broad range of materials (invited)*, Journal of Applied Physics **117**, 172603 (2015), arXiv:1410.1597 .

[57] J.-C. Rojas-Sánchez, N. Reyren, P. Laczkowski, W. Savero, J.-P. Attané, C. Deranlot, M. Jamet, J.-M. George, L. Vila, and H. Jaffrès, *Spin Pumping and Inverse Spin Hall Effect in Platinum: The Essential Role of Spin-Memory Loss at Metallic Interfaces*, Physical Review Letters **112**, 106602 (2014), arXiv:1312.2717v1 .

[58] C. T. Boone, H. T. Nembach, J. M. Shaw, and T. J. Silva, *Spin transport parameters in metallic multilayers determined by ferromagnetic resonance measurements of spin-pumping*, Journal of Applied Physics **113**, 153906 (2013), arXiv:1301.5861 .

[59] X. Liu, W. Zhang, M. J. Carter, and G. Xiao, *Ferromagnetic resonance and damping properties of CoFeB thin films as free layers in MgO-based magnetic tunnel junctions*, Journal of Applied Physics **110**, 033910 (2011).

[60] J. Kim, J. Sinha, M. Hayashi, M. Yamanouchi, S. Fukami, T. Suzuki, S. Mitani, and H. Ohno, *Layer thickness dependence of the current-induced effective field vector in Ta/CoFeB/MgO*, Nature Materials **12**, 240–245 (2012), arXiv:1207.2521 .

[61] Y. Wen, J. Wu, P. Li, Q. Zhang, Y. Zhao, A. Manchon, J. Q. Xiao, and X. Zhang, *Temperature dependence of spin-orbit torques in Cu-Au alloys*, Physical Review B **95**, 104403 (2017).

[62] T. Seifert, S. Jaiswal, U. Martens, J. Hannegan, L. Braun, P. Maldonado, F. Freimuth, A. Kronenberg, J. Henrizi, I. Radu, E. Beaurepaire, Y. Mokrousov, P. M. Oppeneer, M. Jourdan, G. Jakob, D. Turchinovich, L. M. Hayden, M. Wolf, M. Münzenberg, M. Kläui, and T. Kampfrath,

Efficient metallic spintronic emitters of ultrabroadband terahertz radiation, Nature Photonics **10**, 483–488 (2015), arXiv:1510.03729 .

[63] M. Obstbaum, M. Decker, A. K. Greitner, M. Haertinger, T. N. G. Meier, M. Kronseder, K. Chadova, S. Wimmer, D. Ködderitzsch, H. Ebert, and C. H. Back, *Tuning Spin Hall Angles by Alloying*, Physical Review Letters **117**, 167204 (2016).

[64] G. F. Dionne, *Magnetic Oxides* (Springer US, 2010).

[65] K. Enke, J. Fleischhauer, W. Gunsser, P. Hansen, S. Nomura, W. Tolksdorf, and U. Wolfmeier, *Garnets and Perovskites / Granate und Perowskite (Landolt-Börnstein: Numerical Data and Functional Relationships in Science and Technology - New Series) (Volume 12) (English and German Edition)* (Springer, 1977).

[66] E. Mallmann, A. Sombra, J. Goes, and P. Fechine, *Yttrium Iron Garnet: Properties and Applications Review*, Solid State Phenomena **202**, 65–96 (2013).

[67] G. F. Dionne, *Molecular Field and Exchange Constants of Gd^{3+}-Substituted Ferrimagnetic Garnets*, Journal of Applied Physics **42**, 2142–2143 (1971).

[68] G. F. Dionne, *Molecular Field Coefficients of Substituted Yttrium Iron Garnets*, Journal of Applied Physics **41**, 4874–4881 (1970).

[69] S. Koohpayeh, *Single crystal growth by the traveling solvent technique: A review*, Progress in Crystal Growth and Characterization of Materials **62**, 22–34 (2016).

[70] A. H. Morrish, *The Physical Prinicples of Magnetism* (Wiley, 2001) p. 700.

[71] J. A. Osborn, *Demagnetizing Factors of the General Ellipsoid*, Physical Review **67**, 351–357 (1945).

[72] G. P. Rodrigue, H. Meyer, and R. V. Jones, *Resonance Measurements in Magnetic Garnets*, Journal of Applied Physics **31**, 376–382 (1960).

[73] C. D. Stanciu, A. V. Kimel, F. Hansteen, A. Tsukamoto, A. Itoh, A. Kirilyuk, and T. Rasing, *Ultrafast spin dynamics across compensation points in ferrimagnetic GdFeCo : The role of angular momentum compensation*, Physical Review B **73**, 220402 (2006).

[74] L. R. Walker, *Magnetostatic Modes in Ferromagnetic Resonance*, Physical Review **105**, 390–399 (1957).

[75] E. Schlömann, *Spin-wave analysis of ferromagnetic resonance in polycrystalline ferrites*, Journal of Physics and Chemistry of Solids **6**, 242–256 (1958).

[76] M. P. Ross, *Spin Dynamics in an Antiferromagnet*, Diploma thesis, Technische Universität München (2013).

[77] P. F. Herskind, A. Dantan, J. P. Marler, M. Albert, and M. Drewsen, *Realization of collective strong coupling with ion Coulomb crystals in an optical cavity*, Nature Physics **5**, 494–498 (2009).

[78] H. Maier-Flaig, M. Harder, R. Gross, H. Huebl, and S. T. B. Goennenwein, *Spin pumping in strongly coupled magnon-photon systems*, Physical Review B **94**, 054433 (2016), arXiv:1601.05681 .

[79] S. Haroche and J.-M. Raimond, *Exploring the quantum : atoms, cavities and photons* (Oxford University Press, 2006) p. 605.

[80] I. Dzyaloshinskii, *A thermodynamic theory of "weak" ferromagnetism of antiferromagnetics*, Journal of Physics and Chemistry of Solids **4**, 241–255 (1958).

[81] T. Moriya, *Anisotropic Superexchange Interaction and Weak Ferromagnetism*, Physical Review **120**, 91–98 (1960).

[82] S. Seki and M. Mochizuki, *Skyrmions in Magnetic Materials*, SpringerBriefs in Physics (Springer International Publishing, Cham, 2016).

[83] A. Fert, V. Cros, and J. Sampaio, *Skyrmions on the track*, Nature Nanotechnology **8**, 152–156 (2013), arXiv:1008.2287v1 .

[84] G. Finocchio, F. Büttner, R. Tomasello, M. Carpentieri, and M. Kläui, *Magnetic skyrmions: from fundamental to applications*, Journal of Physics D: Applied Physics **49**, 423001 (2016).

[85] X. Zhang, M. Ezawa, and Y. Zhou, *Magnetic skyrmion logic gates: conversion, duplication and merging of skyrmions*, Scientific Reports **5**, 9400 (2015), arXiv:1410.3086 .

[86] Y. Onose, Y. Okamura, S. Seki, S. Ishiwata, and Y. Tokura, *Observation of Magnetic Excitations of Skyrmion Crystal in a Helimagnetic Insulator Cu_2OSeO_3*, Physical Review Letters **109**, 037603 (2012), arXiv:1204.5009 .

[87] T. Schwarze, J. Waizner, M. Garst, A. Bauer, I. Stasinopoulos, H. Berger, C. Pfleiderer, and D. Grundler, *Universal helimagnon and skyrmion excitations in metallic, semiconducting and insulating chiral magnets*, Nature Materials **14**, 478–483 (2015).

[88] P. Bak and M. H. Jensen, *Theory of helical magnetic structures and phase transitions in MnSi and FeGe*, Journal of Physics C: Solid State Physics **13**, L881–L885 (1980).

[89] H. T. Nembach, J. M. Shaw, M. Weiler, E. Jué, and T. J. Silva, *Linear relation between Heisenberg exchange and interfacial Dzyaloshinskii–Moriya interaction in metal films*, Nature Physics **11**, 825–829 (2015), arXiv:1410.6243 .

[90] M. Garst, J. Waizner, and D. Grundler, *Collective spin excitations of helices and magnetic skyrmions: review and perspectives of magnonics in non-centrosymmetric magnets*, Journal of Physics D: Applied Physics **50**, 293002 (2017), arXiv:1702.03668 .

[91] N. Nagaosa and Y. Tokura, *Topological properties and dynamics of magnetic skyrmions.*, Nature Nanotechnology **8**, 899–911 (2013).

[92] I. Kézsmárki, S. Bordács, P. Milde, E. Neuber, L. M. Eng, J. S. White, H. M. Rønnow, C. D. Dewhurst, M. Mochizuki, K. Yanai, H. Nakamura, D. Ehlers, V. Tsurkan, and A. Loidl, *Néel-type skyrmion lattice with confined orientation in the polar magnetic semiconductor GaV_4S_8.*, Nature Materials **14**, 1116–22 (2015), arXiv:1502.08049 .

[93] T. Skyrme, *A unified field theory of mesons and baryons*, Nuclear Physics **31**, 556–569 (1962).

[94] S. Mühlbauer, A. Heinemann, A. Wilhelm, L. Karge, A. Ostermann, I. Defendi, A. Schreyer, W. Petry, and R. Gilles, *The new small-angle neutron scattering instrument SANS-1 at MLZ—characterization and first results*, Nuclear Instruments and Methods in Physics Research Section A: Accelerators, Spectrometers, Detectors and Associated Equipment **832**, 297–305 (2016).

[95] R. Tomasello, E. Martinez, R. Zivieri, L. Torres, M. Carpentieri, and G. Finocchio, *A strategy for the design of skyrmion racetrack memories*, Scientific Reports **4**, 6784 (2015), arXiv:1409.6491 .

[96] W. Kang, Y. Huang, C. Zheng, W. Lv, N. Lei, Y. Zhang, X. Zhang, Y. Zhou, and W. Zhao, *Voltage Controlled Magnetic Skyrmion Motion for Racetrack Memory*, Scientific Reports **6**, 23164 (2016), arXiv:1603.01045 .

[97] S. Woo, K. Litzius, B. Krüger, M.-Y. Im, L. Caretta, K. Richter, M. Mann, A. Krone, R. M. Reeve, M. Weigand, P. Agrawal, I. Lemesh, M.-A. Mawass, P. Fischer, M. Kläui, and G. S. D. Beach, *Observation of room-temperature magnetic skyrmions and their current-driven dynamics in ultrathin metallic ferromagnets*, Nature Materials **15**, 501–506 (2016), arXiv:1502.07376 .

[98] H. Kurebayashi, J. Sinova, D. Fang, A. C. Irvine, T. D. Skinner, J. Wunderlich, V. Novák, R. P. Campion, B. L. Gallagher, E. K. Vehstedt, L. P. Zârbo, K. Výborný, A. J. Ferguson, and T. Jungwirth, *An antidamping spin–orbit torque originating from the Berry curvature*, Nature Nanotechnology **9**, 211–217 (2014), arXiv:1306.1893 .

[99] S. Seki, X. Z. Yu, S. Ishiwata, and Y. Tokura, *Observation of Skyrmions in a Multiferroic Material*, Science **336**, 198–201 (2012).

[100] K. Lüders, G. von Oppen, L. Bergmann, and C. Schaefer, *Bergmann, Schaefer: Lehrbuch der Experimentalphysik Band1; Mechanik, Akustik, Wärme*, 12th ed. (Walter de Gruyter, Berlin, New York, 2008) p. 846.

[101] P. Villars and K. Cenzual, *Cu2OSeO3 (Cu2[SeO3]O rt, T = 10 K) Crystal Structure: Datasheet from "PAULING FILE Multinaries Edition – 2012" in SpringerMaterials (http://materials.springer.com/isp/crystallographic/docs/sd_1627345)* (2016).

[102] T. Adams, A. Chacon, M. Wagner, A. Bauer, G. Brandl, B. Pedersen, H. Berger, P. Lemmens, and C. Pfleiderer, *Long-Wavelength Helimagnetic Order and Skyrmion Lattice Phase in Cu_2OSeO_3*, Physical Review Letters **108**, 237204 (2012), arXiv:1204.3597 .

Acknowledgements

This thesis would not have been possible without the support and knowledge of several people accompanying me during the last year. In particular, I would like to thank:

Prof. Dr. Rudolf Gross for giving me the opportunity to complete my Master's thesis here at the Walther-Meißner-Institut (WMI) and for the nice mentor talk.

Dr. Mathias Weiler for offering me this Master's thesis topic and for being a fantastic supervisor. I am grateful for always having an open door for my numerous questions even multiple times a day, for his enthusiasm and his comprehensive knowledge on seemingly all physics related topics, for his talent explaining complicated subjects in a simple way which has contributed to me being able to build a coherent picture for myself. For encouraging me to try new approaches in experiments, for his extensive proof-reading of this thesis and finally for offering me an interesting project to work on a PhD thesis.

Hannes Maier-Flaig for introducing me to the cryogenic FMR, to its subtleties and sharing his experiences as an experimentalist. For helping me with the measurements of the Gadolinium Iron Garnet, for the long and valuable discussions on anisotropies, AFMR and coupling phenomena, for providing me with an analysis software to quickly visualize colourplots and for patiently helping me with all software (python) and technical related aspects.

Stefan Klingler for first introducing me to the FMR measurement procedure and evaluation, for helping me with everything related to, especially, room-temperature FMR and for always having an open ear for questions.

Dr. Hans Hübl for sharing his extensive knowledge on high-frequency measurements and dynamics in magnetic materials, for his curiosity on my measurements and his ideas for new experiments and processing steps.

Dr. Stephan Geprägs for his several helpful discussions regarding Gadolinium Iron Garnet, providing me with the SQUID-data and for spreading good mood.

Dr. Matthias Althammer for helping me with all kind of issues related with the "Chaos"-cryostat, explaining the technical particularities of several measurement equipment (especially cryostats) to me and for his understanding when I was extending the measurement time in the Chaos (cue: CSO).

The crew of the office 112, in particular, Christian Besson, Johanna Fischer, Sebastian Oberauer, Michaela Schleuder and Jan-Robin Scholz, for the kind and productive atmosphere, for the almost daily coffee walks and discussions and chatting about physics and non-physics related topics.

The other Master's students and especially Clemens Mühlenhoff and Petio Natzkin, for pleasant and helpful ambience and for easily sharing VNAs back-and-forth.

The whole "Magnetiker"-group for the kind and cooperative atmosphere, for the easy sharing of measurement equipment and labs and for always having an open ear for problems and physics related questions.

Prof. Dr. Christian Pfleiderer, Franz Haslbeck and Dr. Andreas Bauer for the insightful discussions regarding Skyrmions and small angle neutron scattering. Thank you for making it possible for me to visit the FMR2 during the neutron measurement time.

All Members of the WMI for the kind and helpful atmosphere which contributed to the successful outcome of the experiments.

My parents, Ute and Bernhard Liensberger, for their unconditional support at any time when I needed it and for giving me the freedom to make my own decisions. I would also like to thank you for enabling me to study here in Munich. Thank you for everything!